The Dissertation Committee for Karun Vijayraghavan Certifies that this is the approved version of the following dissertation:

TERAHERTZ GENERATION WITH QUANTUM CASCADE LASERS

Committee:

Mikhail Belkin, Supervisor

Edward Yu

Dean Neikirk

Gerald Wilmink

Sanjay Banerjee

TERAHERTZ GENERATION WITH QUANTUM CASCADE LASERS

by

Karun Vijayraghavan, B.S.; M.S.E

Dissertation

Presented to the Faculty of the Graduate School of

The University of Texas at Austin

in Partial Fulfillment

of the Requirements

for the Degree of

Doctor of Philosophy

The University of Texas at Austin

December 2014

Dedication

For my parents, sisters, and grandparents.

Acknowledgments

I want to thank my mom Preethi, father Vijay, and sisters Deepthi and Meghana for their never ending support and constant optimism. I'm blessed to have them in my life.

This work would not have been possible without the guidance and support from my supervisor, Dr. Mikhail Belkin. He gave me a chance when others wouldn't and taught me how to properly write papers, grant applications, and made me a better engineer. I'm glad he was able to push me to accomplish what I have and I'm grateful for his support in my commercialization efforts of THz DFG-QCLs.

I would like to thank Dr. Ed Yu, Dr. Dean Neikirk, Dr. Sanjay Banerjee, and Dr. Jerry Wilmink for serving on my committee. With the amount of users at the MRC, Dr. Banjeree and the MRC professors have done an outstanding job maintaining a top notch cleanroom. Jerry has been an inspiring individual who has boundless optimism, energy and an entrepreneurial spirit that is contagious. I'm grateful for his continuous encouragement.

Devices reported in this work were fabricated from excellent wafer material provided by Prof. Edmund Linfield at Leeds University and Prof. Markus Amann at the Technical University Munich. I appreciate the time and effort they invested in the very challenging growth of QCLs! Fabrication was done at the Microelectronics Research Center. The facility staff is the best a student could ask for. They worked tirelessly to ensure tools were up and running. Many thanks to Jesse, Terry, Bill, Ziggy, Johnny, Rico,

Robert, Brenda, Marylene, Darren and James. Also many thanks to the administrative staff Christine, Jeannie, Jackie, Joyce, and Gerlindhe.

I would like to thank my past and current lab mates Seungyong, Yifan, Jae Hyun, and Jongwon. Rob welcomed me in the group with open arms and taught me a lot about THz QCLs. I will remember our lunch time breaks at Rudy's BBQ which would subsequently incapacitate us with a case of the 'itis' for hours after; David Austin who cast me in my first starring movie roll; Min who taught me how to process QCLs; Aiting who was always available if I had questions about processing; and Feng who entertained me with our discussions on a myriad of topics.

Graduate school would not have been as fun without hanging out with some really cool friends. I couldn't have asked for a better roommate and buddy than Lionel. Catching Spurs games and enjoying BBQ-stuffed, heavy metal music concert nights were some of the best times I've had; Kelley for being one of the chillest and nicest persons that I know; Dave and Helen for inviting me over to enjoy great food and always being up for a beer; and my gym buddies Bilal, Rob, Sahil, and Hema who made sure I didn't destroy myself during bench pressing.

I'd like to acknowledge the Cockrell School of Engineering for providing me a fellowship for the first few years of grad school, and NSF and other agencies for funding my last few years.

Terahertz Generation With Quantum Cascade Lasers

Karun Vijayraghavan, PhD.

The University of Texas at Austin, 2014

Supervisor: Mikhail Belkin

The terahertz (THz) spectral range is devoid of commercially feasible radiation sources, detectors, and components. In particular, THz sources are bulky, complex to operate, and cost-prohibitive – more suited for a research laboratory than a commercial setting. Developing compact and mass-producible sources in the 1 to 6 THz spectral range will open up new avenues for this technology to make a mainstream societal impact. The focus of this thesis is the development of compact, room-temperature terahertz sources based on quantum cascade lasers (QCL) and quantum well technology.

QCLs are semiconductor lasers that operate with high power at mid-infrared (mid-IR) and THz frequencies. THz QCLs are the only mW-level average power sources with spectral coverage from 0.8 to 5 THz. However they only work at cryogenic temperatures because they cannot maintain population inversion across the lasing transition at elevated temperatures. Cryogenic cooling makes these sources cumbersome to operate and expensive to manufacture. Room-temperature operation significantly enhances their commercial appeal and a portion of this dissertation investigated the improvement in THz QCL temperature performance using GaAs-$Al_{0.15}Ga_{0.85}As$ double-phonon resonant active region designs. These devices worked up to 173 K and were a substantial improvement compared to prior implementations of double-phonon resonant designs.

Room-temperature THz sources that do not require population inversion across the lasing transition can be engineered by combining the field of nonlinear optics with intersubband transitions in quantum well structures. One method of creating inversionless THz lasing is based upon the principle of Raman gain in semiconductors and this thesis explores the design of an intersubband Raman laser (IRL) with GaAs-$Al_{0.33}Ga_{0.67}As$ heterostructures. The primary focus of this dissertation is developing room-temperature, broadly-tunable, monolithic THz sources based on difference-frequency generation (DFG) in mid-IR QCLs. The source active region is quantum-engineered to provide lasing at mid-IR frequencies, ω_1 and ω_2, and simultaneously have giant second-order optical nonlinearity for THz generation at frequency $\omega_{THz}=\omega_1-\omega_2$. This dissertation developed a Cherenkov emission scheme that produced devices with a narrow emission linewidth, 0.12 mW peak power and tuning from 1.55 to 5.7 THz – the largest tuning bandwidth compared to semiconductor technology of similar size and cost.

Table of contents

List of tables

List of figures

Chapter 1: Introduction to terahertz radiation

1.1 Background and motivation

The terahertz (THz, $f = 1 - 10$ THz) frequency range is a narrow portion of the electromagnetic spectrum that bridges the void between high-frequency electronics and visible/infrared optoelectronics. Some unique aspects of THz radiation (also known as T-rays) are its transmission through materials that block infrared/visible light (i.e. plastics, ceramics, paper) and its ability to identify chemical/biological substances with strong THz absorption signatures.

The manufacturing industry would like to use T-ray sensing systems for improved quality control [1-3], pharmaceutical companies are interested in adopting THz spectroscopy to nondestructively evaluate the chemical and physical composition of tablets [4], doctors are interested in T-ray imagers to identify cancerous skin or tissues [5], dentists would like to replace X-ray imaging with T-ray imaging because of improved safety [6], security agencies are keen on using a THz imager-sensor combo system to probe suspicious packages and entities for contraband [7], the astronomy community desires high-frequency THz local oscillators to map different constellation formations in the universe [8, 9], and the defense industry has interest in T-ray sensors to protect soldiers and civilians from chemical/biological attacks [10].

Research and development of THz sources, detectors and components has been ongoing for more than 60 years. Yet the commercial development of this field is severely lagging. The THz radiation band is teeming with mainstream concepts and ideas but awaits a breakthrough in the technology infrastructure. In particular, THz radiation

sources are bulky, complex in design and operation, and expensive to manufacture. Real-world commercial applications for spectroscopy or imaging require sources that are not only compact and cost-effective, but emit with high spectral purity, high power and are frequency agile over a wide range.

It's worth noting that polar substances, particularly H_2O in the atmosphere, have strong absorption features from 1 – 10 THz and restricts the working distance of milliwatt-level sources to a few meters [11]. While this limits the practicality of many envisioned applications, it makes it all the more important to develop compact sources that are portable and have the capability to tune around strong absorption features. The focus of this thesis is the development of compact, electrically-pumped, room-temperature quantum cascade lasers sources that operate in the 1 – 6 THz spectral range.

1.2 Commercial terahertz semiconductor source technology

A variety of THz sources have been developed and a good review can be found in Refs. [1, 12]. Some of the best performing THz sources are travelling wave vacuum oscillators, optically pumped molecular lasers, optical parametric amplifiers, helium-cooled p-doped germanium lasers, and free-electron lasers. While these sources can operate with mW-level average power over a wide spectral range, they are not intended for commercial applications because of their sheer size, power consumption and complexity. From a commercial viewpoint, semiconductor THz sources are most appealing given their compact size and ruggedness, simple battery powered operation and propensity for mass-production. Table 1-1 lists the performance metrics of

commercialized semiconductor sources that are described in more detail in the text below.

Gunn diodes are electronic semiconductor sources with a maximum operating frequency at the boundary of the mm-wave and THz radiation bands [12]. These devices turn into THz oscillators when biased to a negative differential resistance due to electrons transferring from the gamma valley to higher order valleys with increased voltage bias. These higher order valleys have a larger effective mass and hence lower carrier velocity, so the overall device current drops with increasing voltage. Typical high-performance GaAs-based devices can produce microwatts of average power up to 0.6 THz. But the transit time of carriers between the cathode and anode limits the maximum oscillation frequencies to below 1 THz.

Multiplier chains are electronic semiconductor sources that work under the principle of up converting microwave radiation to THz frequencies using nonlinear electronic mixing elements [13]. An RF signal oscillating between 30 GHz – 100 GHz is passed through a series of nonlinear mixing elements, typically Schottky diodes, that produces an output signal at a higher-order harmonic of the input signal. These sources operate continuous-wave with milliwatts of power in the 500 GHz – 1500 GHz spectral range. Beyond 1.5 THz, the output power rapidly drops due to carrier velocity constraints and conversion efficiency loss aggregated with each mixing stage. Typically, 3-6 multiplier stages are required for THz multipliers and adds to the system size and manufacturing cost. Virginia Diodes Inc. is the primary manufacture of THz multipliers and have demonstrated sources that operate up to 2.6 THz. They have carved

a niche in the THz market providing high-frequency local oscillators for communications related applications. However, the output power of their sources is prohibitively small for commercial applications beyond 2 THz.

Photoconductive switches are another popular commercial source that generates THz radiation by optically pumping low-temperature grown GaAs with a femtosecond pulsed laser and inducing a current transient between two arms of an antenna [14]. The Fourier transform of the short current pulse results in a broad spectral output that spans from 0.01 – 3 THz. Commercial systems have been developed by numerous companies including Teraview Ltd., Picometrix, and Z-omega Optics to name a few. A significant drawback with these sources is the cost and size of the femtosecond pulsed laser. The necessity of multiple optical components requires careful and precise assembly which adds to the manufacturing cost. Additionally, these sources have a small THz spectral operating range and has broadband output that cannot be tuned and limits the system resolution to a few GHz.

Photomixers are based on the principle of interfering two infrared diode laser with offsetting frequencies ν_1 and ν_2, with an antenna patterned on low-temperature grown GaAs material [14]. An oscillation current at the beat frequency $\nu_{THz} = \nu_1 - \nu_2$ is generated between the anode and cathode of the antenna and radiated to free-space. Photomixers can operate at room-temperature with narrow linewidth and tunable emission. Toptica has developed a line of THz photomixers based on LT-GaAs pumped with fiber coupled 870 nm and 1550 nm telecom diode lasers. However, these sources are spectrally limited to operate with modest power at frequencies below 2 THz. Carrier

transit time and resistance-capacitance effects significantly reduces power at higher THz frequencies.

Quantum cascade lasers are class of compact, electrically-pumped, high power semiconductor lasers first demonstrated in 1994 at Bell labs [15]. QCLs are the workhorse laser source in the mid-infrared (mid-IR, λ = 3 μm – 12 μm) spectral range. Mid-IR QCLs can operate continuous-wave [16] at high-temperature [17], and high-power exceeding tens of Watts [18]. Distributed-feedback QCLs [19] enables stable single frequency emission and have become key optical components for gas and chemical sensing [20], and pollution monitoring. Additionally, a single QCL can be designed with an extremely broad gain spectrum [21] and have been developed into broadly-tunable mid-IR QCL systems that now widely-adopted in laboratories and commercial applications (see Daylight solutions).

Terahertz QCLs took longer to develop and were first demonstrated in 2002 [14]. Currently they are the most powerful and compact THz source that can operate from 0.8 THz to 5 THz with a milliwatt-level average power [22-24]. Similar to their mid-IR counterparts, a variety of single-frequency distributed-feedback THz QCLs have been developed and deployed in sensing and spectroscopy applications. Given their high-power output, THz QCLs are also used in a variety of far-infrared imaging systems for security monitoring and contraband detection. Longwave Photonics has successfully spearheaded the commercial developments of THz QCL systems for imaging and sensing.

A significant drawback for THz QCLs is that they require cryogenic cooling to operate. This leads to an increase in system size, mechanical complexity (which inevitably affects reliability), and power consumption. Additionally, cryo-cooled systems require a more complex procedure for operation and maintenance. For example, commercial THz QCLs are housed in Stirling engine cryo-coolers. The cryo-cooler is bulky (typically 2ft x 2ft x 0.5 ft, >10 kg), consumes more than 100 W power, takes 20 – 30 minutes to cool lasers down prior to operation, and requires periodic vacuum purging. Furthermore, extra dampening measures are required to isolate the QCL chip from piston-induced mechanical vibrations. These factors are the motivation for the research time and money spent to develop room-temperature THz QCLs. A portion of this thesis explores improving the temperature performance of sources with optimized active region designs. While the current maximum operating temperature of lasers is 200 K [25], the march towards room-temperature or even thermoelectric-cooled operation has slowed considerably in the last 5 years. Another drawback with THz QCLs is their limited tuning range. Heterogeneous active region designs can broaden the gain bandwidth to over 1 THz, but tunable THz QCLs have only demonstrated 350 - 500 GHz tuning bandwidth from a single chip using a MEMs-tuning approach which requires a cryo-cooled piezo stage to actuate the MEMs system [26].

	Virginia diodes: multipliers	Z-omega Optics: Photoconductive switches	Toptica Optics: Photomixers	Longwave Photonics: THz QCLs
Spectral range	< 2.4 THz	< 5THz	< 2 THz	1.8 – 5 THz
Single frequency	Yes	No	Yes	Select frequencies
Pumping scheme	Electrical	Optical	Optical	Electrical
Tuning bandwidth	< 0.2 THz	No tuning	< 2 THz	< 0.3 THz
Average power	0.001 mW	0.001 mW	0.005 mW	0.5mW – 2 mW
Linewidth	< 1 MHz	30 GHz	2 GHz	< 10 MHz
Approximate Cost	$60K – $100K	$120K <	unavailable	$120K <

Table 1-1, Commercialized semiconductor THz source technology: Specifications taken from company websites and data sheets.

Alternative methods of generating room-temperature THz radiation is made possible by bridging the fields of nonlinear optics with QCLs and related intersubband quantum well structures. This thesis specifically reports on the design of intersubband Raman lasers with quantum wells and THz generation using nonlinear frequency in QCLs.

Quantum well devices can be designed to possess giant optical nonlinearity that is dramatically enhanced by the intersubband transitions of carriers between confined energy states [27]. The typical strength of the nonlinearity for intersubband structures is three to four orders of magnitude larger than bulk optical crystals and semiconductors. Highly compact and energy efficient lasers and sources can be engineered compared to traditional nonlinear sources. Nonlinear optics using mid-infrared QCLs can produce radiation at frequencies outside the typical range or operating parameters of these sources. The first demonstration of this concept was second-harmonic generation (SHG) in mid-IR QCLs used to extend emission below $\lambda = 3$ μm [28]. Difference-frequency generation (DFG) in dual-wavelength mid-infrared QCLs has demonstrated room-

temperature THz generation [29, 30]. However, the power of those sources was extremely low and the spectral coverage was limited to only 4-5 THz generation [30].

1.2 Contributions and organization of dissertation

This thesis describes the work done on improving the temperature performance of THz QCLs, exploring the feasibility of a THz source using intersubband stimulated Raman scattering in quantum wells and reports on the development of broadband emission and broad tunability in THz DFG-QCLs.

Chapter 2 provides a brief introduction to quantum cascade lasers and outlines our efforts to improve the temperature performance of THz QCLs using a two-phonon resonant active region design. Chapter 3 discusses work done on modeling and testing THz intersubband Raman lasers made with the GaAs/AlGaAs heterostructures system.

Chapters 4 to 6 highlights the contribution of this thesis in the development of THz DFG-QCLs. Chapter 4 discusses the adapting a broadband, high-efficiency Cherenkov emission scheme for THz DFG-QCLs. These were the first devices with emission below 4 THz. Chapter 5 presents optimized Cherenkov THz DFG-QCLs sources that produce single frequency emission and are broadly tunable over the 1 – 6 THz spectral range. Chapter 6 reports on 3.5 THz sources grown at a commercial foundry. Concluding remarks are given in Chapter 7 and details the prospects of commercializing THz DFG-QCL technology.

Chapter 2: Terahertz quantum cascade lasers with a double-phonon resonant active region design

Terahertz quantum cascade lasers (QCLs) are the only compact, electrically-pumped semiconductor source that operates in the 1 – 5 THz spectrum with mW-level average power. However they require cryogenic cooling to lase and there are ongoing efforts to achieve room-temperature operation. This chapter will describe attempts to improve the temperature performance of THz QCLs using an optimized double-phonon resonance active region design.

2.1 Quantum cascade lasers background

The concept of an intersubband laser was first proposed in 1972 by Kazirnov and Suris, and they postulated that optical gain could be engineered in a superlattice using intersubband transitions between confined conduction band states [31]. This idea was validated in 1994 when Faist et al. at Bell labs demonstrated the first quantum cascade laser [15]. The conduction band diagram along with the electron wavefunctions from that work is shown in Fig. 2-1 and nicely illustrates the basic operating principle of a QCL. The structure was grown on an InP substrate and the active region comprised of three quantum wells made with alternating layers of nm-thick $In_{0.53}Ga_{0.47}As$ wells and $In_{0.52}Al_{0.48}As$ barriers. The three primary energy levels in the lasing process are the upper laser (E_3), lower laser (E_2) and the injector (E_1) states. Electrons are electrically injected into the upper laser level. Carriers relax to the lower laser state by emitting photons and lasing takes place when there is a sufficient carrier population difference between the upper and lower leve l. The lifetime of the lower laser state is minimized by quickly

A portion of this work has been published in R.W. Adams, K. Vijayraghavan, Q.J. Wang, J. Fan, F. Capasso, S.P. Khanna, A.G. Davies, E.H. Linfield, and M.A. Belkin, "GaAs/AlGaAs terahertz quantum cascade lasers with double-phonon resonant depopulation operating up to 172 K," ***Applied Physics Letter***, 97, **131111 (2010). All authors contributed to this work.**

funneling carriers to the injector state via electron-longitudinal optical (LO) phonon scattering. Electrons then flow through a digitally graded quantum well lattice and are injected into the upper laser state in the next active region period. A typical QCL is made up of 20 – 50 repetitions of the active region/injector that is sandwiched between waveguide cladding layers. Transport through the band structure takes place when an externally applied bias field aligns the energy levels such that carriers resonantly tunnel through the injector region into the next active region. Most QCL designs have an active region where lasing takes place and an injector/extractor stage to funnel carriers to the next period.

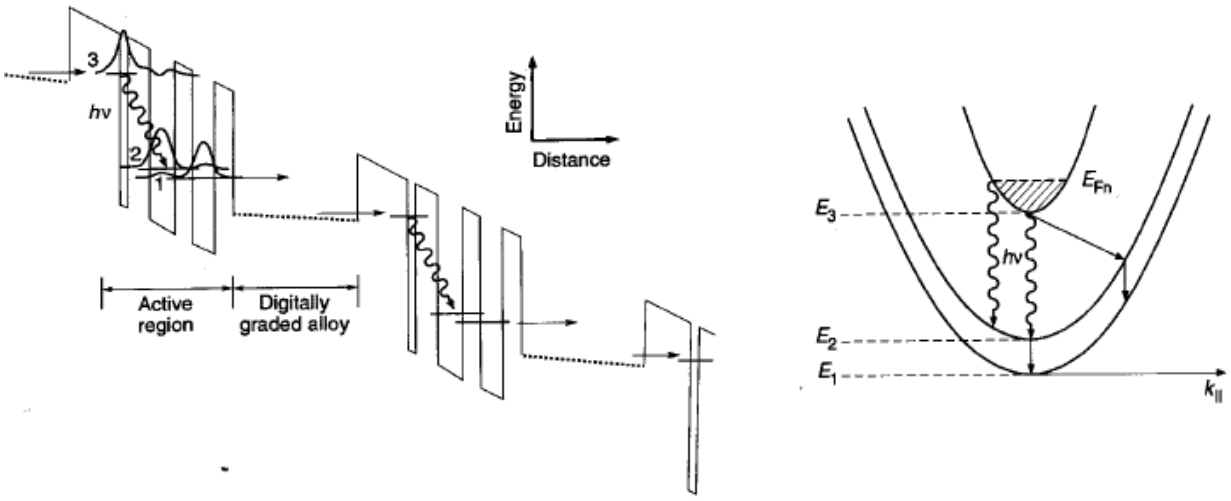

Figure 2-1, QCL bandstructure: (a) Band structure of the first QCL demonstrated in 1994 and corresponding E-k diagram representing the different scattering processed between states. The squiggly lines represent photon emission and the straight lines LO-phonon emission. Figures are taken from Ref. [15].

Traditional type-I diode lasers are based on the recombination of electrons in the conduction band with holes in the valence band and the emission wavelength is determined predominately by the constituent material bandgap. QCLs are unipolar

devices where the emission wavelength is determined by the energy level spacing of confined states in the conduction band and is controlled by tailoring the thicknesses of the quantum wells and barriers. Additionally, the scattering lifetime for QCLs and intersubband structures is on the picosecond timescale (compared to nanoseconds for interband lasers). To achieve optical gain, the upper and lower state carrier lifetimes are controlled by carefully engineering the energy state separations and wavefunctions distribution. The upper state lifetime can be maximized by strategic placement of tunnel barriers [32], creating a Bragg reflector miniband [33], or by engineering a diagonal overlap between the lower laser state [34]. The lower state lifetime is minimized using resonant electron-LO phonon scattering stages or a continuum of states to rapidly dump carriers into the injector states [35]. One nice feature of QCLs is the relatively constant scattering lifetimes over a wide temperature range that results in large characteristic temperature coefficients at high-temperatures.

The modeling of a QCL band structure and energy states is achieved by solving Schrödinger's equations in the $k \cdot p$ approximation [36]. The system Hamiltonian accounts for the potential of the crystal, heterostructures, bias across the band structure, and state lifetimes derived from rate equations. The Hamiltonian is solved self-consistently with Poisson's equation to account for doping in structures. This thesis uses a third-party program developed specifically for modeling intersubband structures.

III-V heterostructures are exclusively used in the QCL design and structures are grown either with Molecular Beam Epitaxy [37] or Metal Organic Chemical Vapor Deposition [38]. The two predominant material systems used in the active region design

are $In_xGa_{1-x}As/In_yAl_{1-y}As$ grown on InP substrates and $GaAs/Al_xGa_{1-x}As$ grown on GaAs substrates. The remarkable aspect of these lasers is the wide spectral range of operation from a single material system, as illustrated in Fig. 2-2. For example, InP QCLs can be designed to lase at infrared (λ = 3μm - 24μm) and THz (λ = 60μm - 300μm) frequencies. It should be noted that QCLs cannot lase in the Restrahlenband (λ = 30 μm – 50 μm) because the material loss from phonon absorption is prohibitively large.

High-performance mid-infrared QCLs (λ = 3.4μm - 12μm) are fabricated with the InP/ $In_xGa_{1-x}As/In_yAl_{1-y}As$ heterostructure system because of the large conduction band offset that effectively confines carriers in the quantum wells and minimizes carrier leakage into the energy continuum. Scattering into satellite conduction-band valleys is also significantly smaller for carriers high energy states in this system [36]. Additionally, InP is a good waveguide cladding material because it has a smaller refractive index compared to the active region and has excellent thermal conductivity. The combination of small intrinsic losses, large material gain, and superior cladding properties results in excellent performance for InP QCLs in the λ = 5 μm - 12 μm range. For lasing in the λ = 3 μm - 5 μm range, strain-compensation is used to increase conduction band offset and continuous-wave, room-temperature lasing at $\lambda \approx 3$ μm has been demonstrated. Lasing below $\lambda \approx 3$ μm with $In_xGa_{1-x}As/In_yAl_{1-y}As$ has not been demonstrated because of insufficient gain due to carrier leakage into the continuum (caused by poor carrier confinement). A promising solution for $\lambda \approx 2.5$ - 3 μm emission are QCLs constructed with InAs/AlSb heterostructures and work is being done to realize room-temperature operation [39].

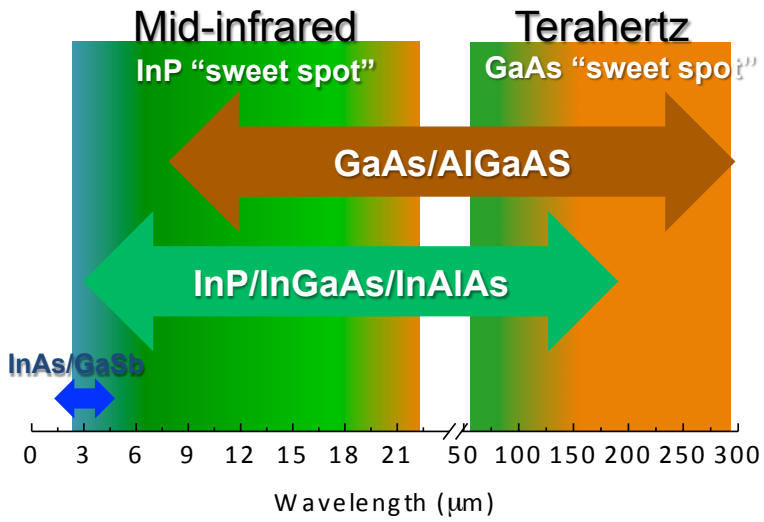

Figure 2-2, QCL materials: Heterostructure systems used to construct quantum cascade lasers. InP heterostructures are best suited for mid-infrared operation while GaAs heterostructures have the best performance in the terahertz.

High-performance THz QCLs are made with GaAs/$Al_xGa_{1-x}As$ heterostructures. Excellent material quality is routinely achieved with this material system due to the maturity of the growth process. Despite having a larger effective mass, smaller oscillator strength, and smaller gain coefficient, the THz material loss in GaAs-based heterostructures is significantly smaller compared to InP-based designs. The first demonstration of THz QCL was in 2002 [40]. These initial devices used a chirped super lattice active region design and a semi-insulting surface plasmon ridge waveguide for THz modal confinement. Devices emitted at 3 THz and operated up to 50 K in pulsed mode. In 2003, lasers operating up to 137 K was demonstrated by MIT [41]. Devices used a double-metal surface plasmon waveguides with near unity modal overlap and reflectance, and significantly reduced the gain threshold. In 2005, continuous-wave

operation up to 117 K (and 164 K pulsed-operation) was demonstrated using a double-metal waveguide and resonant-phonon active region design [42]. In 2008 lasing at 178 K was demonstrated using copper-copper double-metal waveguides [43] and a year later lasing at 186 K was shown using an optimized resonant phonon active region design [44]. A more thorough history mapping the temperature performance developments of THz QCL can be found in Ref [45].

2.2 Terahertz quantum cascade lasers with double-phonon resonant depopulation

By 2010, state-of-the-art THz QCLs were constructed with a GaAs-$Al_{0.15}Ga_{0.85}As$ heterostructures and used active regions with a single-phonon resonant depopulation scheme [41]. The band structure of a single-phonon resonant (SPR) active region along with the electron wavefunctions is shown in Fig. 2-3 and illustrates the operating principle of this type of design. Carriers are injected into the upper laser state (blue) and relax to the lower state (green) via THz emission. Lower state carriers are quickly transition to the injector state (black) using electron-phonon scattering. This is accomplished by separating the lower laser level and injector state by a LO-phonon, which is 36 meV for GaAs. In this manner, the lower state lifetime is minimized and population inversion can be maintained. As the QCL operating temperature increases, LO-phonon scattering of thermal carriers in the upper laser state significantly reduces the upper state lifetime of carriers and the thermal backfilling of the lower laser level from carriers in the injector significantly increases the lower state lifetime. These two effects are illustrated in the E-K diagram of Fig. 2-3 and combine to diminish the population inversion at high-temperatures. Although structures could be pumped with higher

currents to achieve population inversion, the doping required to achieve this would result in prohibitively high waveguide losses.

In this work, we investigated improving the performance of THz QCLs by designing and testing a double-phonon resonant active region design to reduce the thermal backfilling of the lower laser level. In this scheme, the lower laser state is separated from the injector by two equally spaced LO-phonon energy levels, as shown in Fig. 2-4. We can estimate the amount of backfilling into the lower state by using a Boltzmann approximation for the carrier distribution give as,

$$\frac{n_L}{n_{inj}} \propto \exp\left[\frac{-E_{LO}}{k_B T_e}\right] \tag{2.1}$$

where n_{inj} is carrier sheet density in the injector, n_L is population in the lower laser state and T_e is the electron temperature. It should be noted that the electron temperature is approximately 50K – 100K higher than the lattice temperature [46]. Assuming a lattice temp of 195 K and an energy separation between the states being an LO phonon energy, as in the case of a single phonon resonant design, nearly 20% of carriers in the injector backfill into the lower level. However, if the energy separation is twice the LO phonon energy, as in the double phonon case, only 3% of the carriers are estimated to backfill. The reduction in backfilling is expected to improve population inversion at higher temperatures.

MIT first tried a double-resonant active region designs in 2006 and devices were made with a GaAs/$Al_{0.3}Ga_{0.7}As$ heterostructure and had maximum operating temperature T_{max} = 138 K in pulsed mode [47]. The operating temperature was a significantly lower

compared to single-phonon resonant devices with a T_{max} = 164 K at that tim[42]. However, it was difficult to draw any general conclusions from their comparison as the design space of double-phonon THz QCLs was virtually unexplored and the devices in Ref. [47] had complicated injectors susceptible to parasitic absorption.

In this work, we compared the performance of a double-phonon resonant and single-phonon resonant active region design, with both having a similar emission frequency and design parameters. We chose to use a GaAs/$Al_{0.15}Ga_{0.85}As$ heterostructure because of its smaller conduction band offset compared to GaAs/$Al_{0.3}Ga_{0.7}As$. A smaller conduction band offset allows for better energy level control in THz QCLs, and leads to a reduced interface roughness scattering and linewidth broadening [48]. The conduction band diagram for the single-phonon resonant and double-phonon resonant active region designs is shown in Fig. 2-3 and Fig. 2-4, respectively. Band structures were simulated using a 1-D Schrodinger-Poisson solver and the layer sequence and other relevant design parameters are given in the figure caption. To reduce current leakage and parasitic absorption, the energy separation between the electron levels needed for laser operation and parasitic levels lying in higher energy states was maximized. This was accomplished using a two-well injector to push parasitic energy levels higher in energy compared to their positions in 3-quantum-well THz QCLs and their possible double-phonon derivative. Both lasers were designed with injection and extraction anti-crossing energies of $\Delta_{inj}\approx$2.0 meV and $\Delta_{extr}\approx$4.0 meV, respectively. The upper-lower laser state transition dipole moment

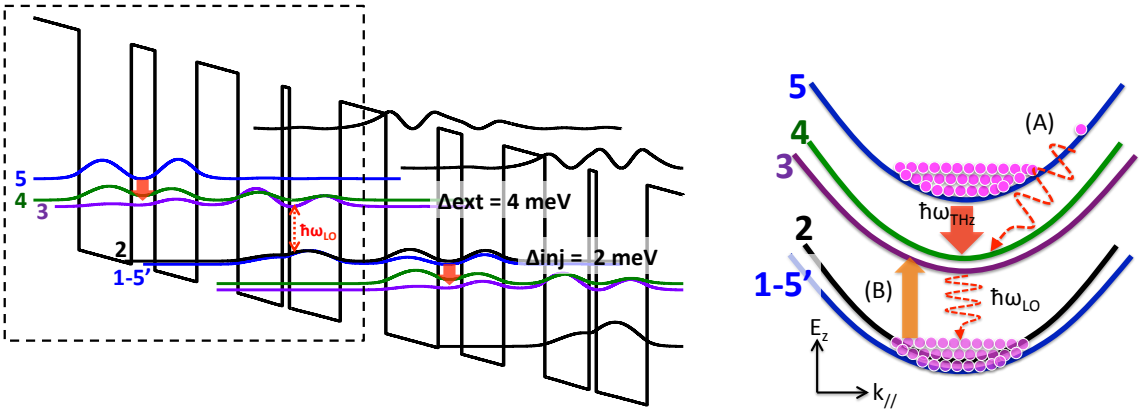

Figure 2-3, L235 single phonon resonance band structure: Conduction band diagrams, under operating bias, of a two quantum-cascade stages of the devices with single-phonon resonant depopulation active regions. A single quantum-cascade stage is marked by a dashed box. The operating bias voltage was calculated to 12.8kV/cm. The layer sequences, in nanometers, the single-phonon design are, starting from the injection barrier (the barrier on the leftmost side of the band diagrams): **6.2**/7.1/**3.2**/5.7/**5.6**/6.0/**1.0**/6.9, Here, $Al_{0.15}Ga_{0.85}As$ barriers are indicated in bold and the underlined layers are n-doped. For the single-phonon design, 2.5nm and 2.4nm sections of the 6.0nm and 6.9nm wells immediately adjacent to the 1 nm barrier were n-doped at 5×10^{16} cm^{-3}. Red block arrows indicate lasing transitions, with energies and dipole moments as indicated. Phonon transitions are indicated with red dashed arrows and labeled $h\omega_{LO}$.

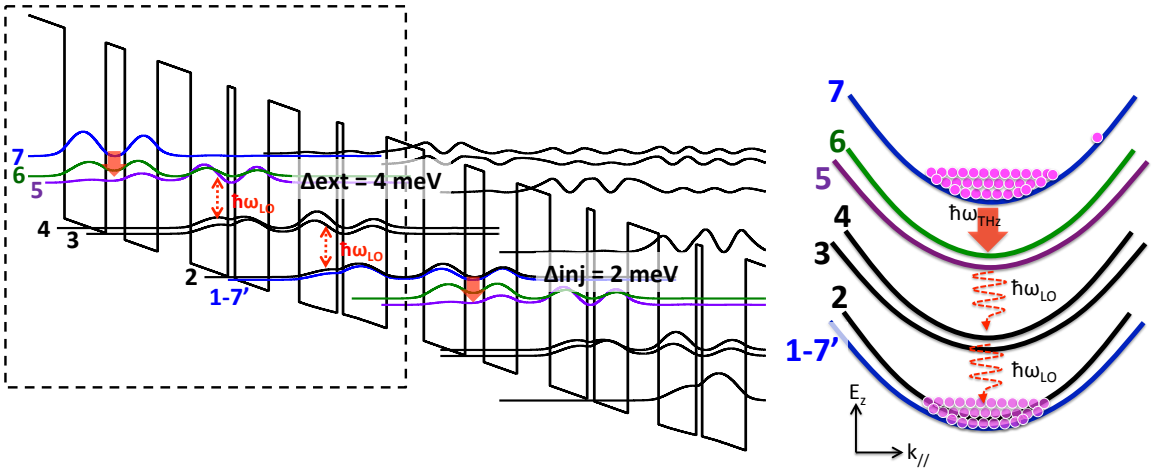

Figure 2-4, L220 double phonon resonance band structure (continued on next page): Conduction band diagrams, under operating bias, of a two quantum-cascade stages of the devices with double-phonon

resonant depopulation. A single quantum-cascade stage is marked by a dashed box and the total number of stages is indicated. The operating bias voltage was calculated to be 14.3kV/cm. The layer sequences, in nanometers, for the double-phonon and single-phonon designs are, starting from the injection barrier (the barrier on the leftmost side of the band diagrams): **6.3**/7.0/**3.2**/5.6/**5.6**/6.3/**1.2**/5.7/**5.2**/6.4/**1.0**/7.4. Here, $Al_{0.15}Ga_{0.85}As$ barriers are indicated in bold and the underlined layers are n-doped. For the double-phonon design, a 6.4nm well was uniformly doped at 5.9×10^{16} cm^{-3}. Red block arrows indicate lasing transitions, with energies and dipole moments as indicated. Phonon transitions are indicated with red dashed arrows and labeled $h\omega_{LO}$.

The QCL material was grown at Leeds University by molecular beam epitaxy. An undoped GaAs substrate was used and the growth sequence started with a 250-nm-thick undoped GaAs buffer layer. This was followed by a 300-nm-thick $Al_{0.5}Ga_{0.5}As$ etch-stop layer, a 75-nm-thick layer of GaAs *n*-doped to $5x10^{18}$ cm^{-3}, a 10-μm-thick active region consisting of multiple repetitions of the layer sequences listed in the Figs. 2-3 and 2-4 caption, and finally a 50-nm-thick GaAs layer *n*-doped to $5x10^{18}$ cm^{-3}.

Samples were fabricated into metal-metal ridge waveguides and the processing steps is shown in Fig. 2-5. Metallization of the QCL wafer and a receptor wafer commenced first and consisted of 10-nm thick Ti and 500 nm-thick Au. The wafers were then sent to Applied Microengineering Ltd. for wafer bonding. Bonding was done in a N_2 purged atmosphere and at 320° C under a constant pressure of 37.5 kg/cm^2. Next, the QCL substrate was mechanically lapped to ~150 μm thickness using a SiC lapping paste. The remainder of the substrate was chemically etched using 19 parts H_2O_2 and 1 part NH_4OH. The etch rate was ~2.5μm/min at 25°C and is selectively etches GaAs over AlGaAs. The $Al_{0.5}Ga_{0.5}As$ etch stop layer was then stripped with HF. Sample fabrication

began by defining the top metal waveguide using a metallization image-reversal lift off process and consisted of a 5 nm-thick Ti adhesion layer followed by a 500 nm-thick Au waveguide layer. The Au strips also served as a self-aligned etch mask for the deep ridge etch. Etching was carried out with an Oxford 100 ICP-RIE using a BCL_3 gas combination. Fomblin was applied to the substrate backside for improved thermal conductivity. The etch recipe parameters are the following: BCl_3 9 sccm, N_2 3 sccm, 450 W ICP power, 30 W RF power, 165 V DC bias, and 5 mTorr pressure. The etch time was approximately 9 minutes and the depth was equal to the active region thickness. The sample substrate was then mechanically polished to ~150 – 200 μm thickness and metallized with 5-nm thick Ti and 100 nm thick Au. Lasers were cleaved into approximately 2 mm-long bars, indium soldered to copper heatsinks, and mounted in a cryostat for testing. Testing was done using 100 ns pulse widths and 2.5 kHz repetition rate. The THz signal was collected with a calibrated He-cooled Silicon bolometer. Spectral measurements were recorded using a step-scan with a Bruker Vertex 70 Fourier Transform Infrared Spectrometer. Power measurements were done using an off-axis parabolic mirror setup and corrected for collection efficiency loss, which was 50% for our set up.

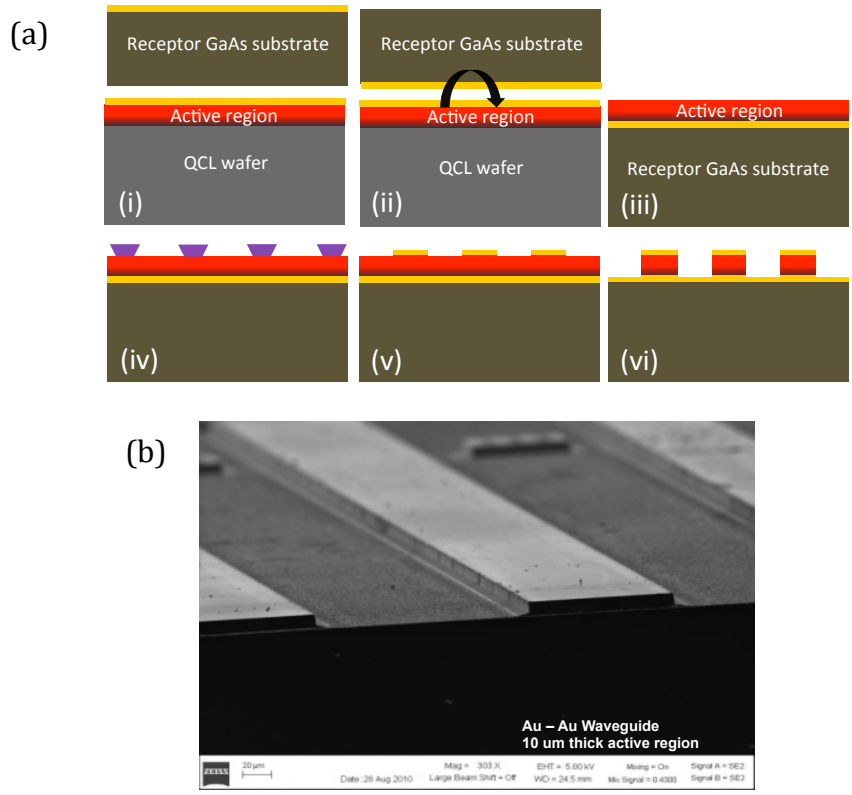

Figure 2-5, QCL fabrication steps: (a) The steps followed to process THz QCLs. (i) the QCL wafer and receptor wafer are first metallized (ii) metal-metal bonding (iii) the QCL wafer is removed with a combination of physical lapping and chemical etching (iv) image reversal photolithography (v) top waveguide metallization and liftoff (vi) deep waveguide ridge etching (b) SEM of the processed ridge waveguide metal-metal THz QCL.

The current-voltage and current-intensity plots for these two designs are shown in Fig. 2-6. As seen in the I-V characteristics, the operation voltages for both devices are considerably higher than the values of 14.3 and 12.8 V expected from the band structure calculation. A similar discrepancy has been observed previously and is likely to be due to the nonalloyed contact resistance in our structures [49, 50]. At low temperatures, the double- phonon lasers have much lower threshold current densities than single-phonon devices. Since the double-phonon devices have considerably higher sheet density per

QCL stage (3.8×10^{10} cm^{-2} vs. 2.5×10^{10} cm^{-2}), and a higher average doping density (6.2×10^{15} cm^{-3} vs. 5.9×10^{15} cm^{-3}), compared to their single-phonon counterparts, the observed lower threshold current density for these devices indicates suppression of parasitic current channels and a more efficient electron injection into the upper laser state. We note that single-phonon devices are susceptible to parasitic current that is produced by electron tunneling from the lower injector state to the upper injector state in the next QCL stage and subsequent LO-phonon relaxation [51]. Using this model we obtain a parasitic current of 810 A /cm^2 for single-phonon devices, which is close to the experimental value. This approach, however, cannot be used to calculate parasitic current in double phonon devices because only at operational bias do energy levels align to allow electron transport through the whole QCL period. This property of double-phonon devices is likely the reason for lower parasitic current. Detailed analysis of parasitic current in double-phonon devices needs to include the consideration of space-charge buildup during electron transport.

The double-phonon devices operated with a $T_{Max} \approx 172$ K compared to $T_{Max} = 156$ K for single phonon devices. Threshold current density J_{th} as a function of temperature is plotted in Fig. 2-6(c). The data suggests that the double-phonon design has a weaker dependence of J_{th} on temperature. From this we can infer that effects of thermal backfilling are not as severe compared to the single phonon design.

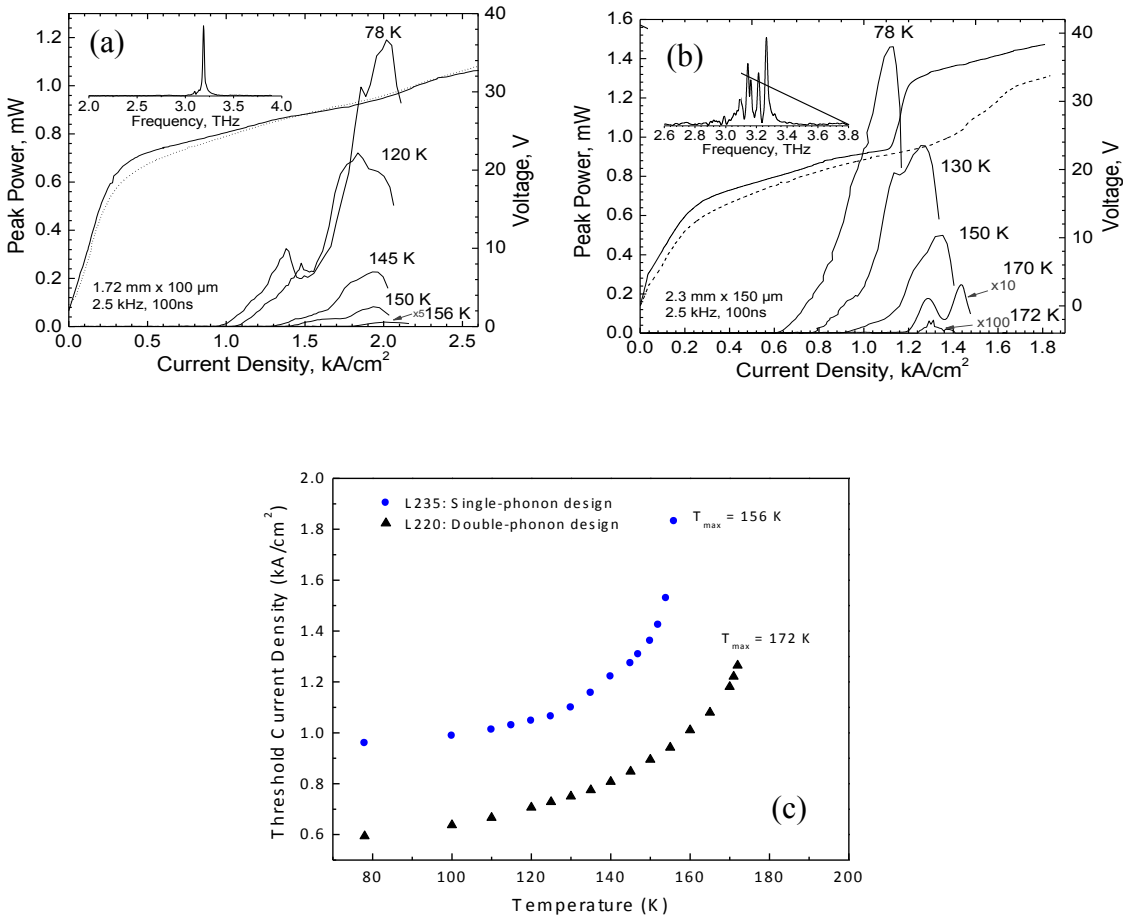

Figure 2-6, Device performance: Current-voltage (I-V) and light output-current (L-I) characteristics of (a) a single-phonon device, and (b) a double-phonon device, operated with 100ns pulses at different temperatures. Solid I-V lines represent device operation at 78K and dashed I-V lines represents device operation at 156K for the single-phonon device and 170K for the double-phonon device. Insets: device spectra near the peak output power at 78K. Results. (c) Threshold current density J_{th} as a function of temperature for single-phonon circles and double-phonon triangles devices. The data suggests that the double-phonon design has a weaker dependence of Jth on temperature of. Results were obtained with a 1.72 mm x 100 µm single-phonon device and a 2.3 mm x 120µm double phonon device operated in pulsed mode with 100 ns pulses.

An interesting characteristic of the double-phonon devices are the two lasing peaks, as seen in the L-I, at high temperatures. The secondary peak begins past the onset of the "negative differential resistance" region in the I-V curve. While this phenomenon is not very pronounced, it has been confirmed in all tested devices. The second peak in the L-I curve occurs at a bias voltage approximately 2.2 V above that of the initial peak and spectral measurements reveal a constant emission frequency as the laser goes into the "negative differential resistance" regime. To understand this effect, band structure simulations at biases corresponding to both lasing peaks were carried out and shown in Fig. 2-7. The wavefunction alignment breaks down at the secondary lasing peak bias field and indicates the onset of negative differential resistance as expected. At negative different resistance bias, we thought a parasitic energy may come into alignment with levels 4-5 and thereby creating a parasitic current channel that enabling lasing. But there wasn't clear evidence of this. To better understand the situation, we consulted with a QCL modeling group at Technical University Munich that studied the carrier dynamics in our structure. Their results indicate carriers at high temperatures thermalize into the quantum wells that localize states 3-4 (see Fig. 2-4) and creates a local space charge that disrupts the resonance of these levels. As the device is biased past the roll over and the into negative differential resistance regime, states 3-4 realign to improve the scattering of carriers from the lower state and thereby increase the lasing power.

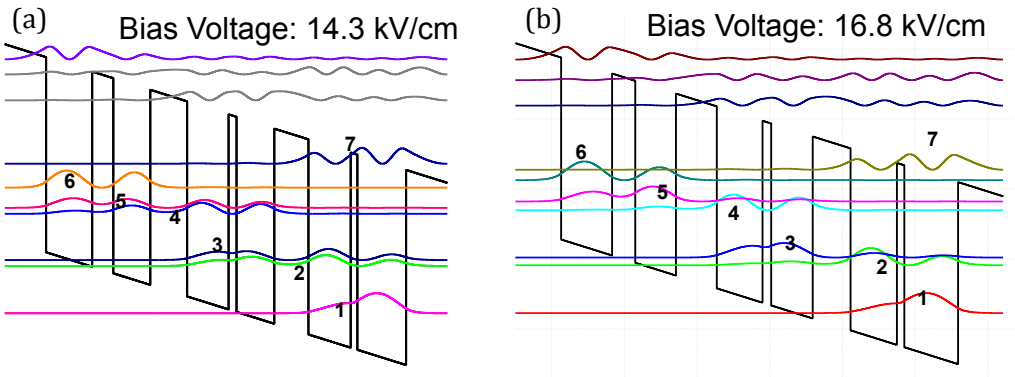

Figure 2-7, L220 band structure simulation at rollover: (a) Band structure alignment at the voltage corresponding to the initial lasing peak. This is optimal bias where the energy levels are resonantly aligned for transport. (b) Band structure alignment at the voltage corresponding to the secondary lasing peak. At this bias the neegy levels come out of resonant alignment and resonant tunneling through the structure diminishes.

A slight modification to the active region was made with the goal of increasing the maximum operating temperature by correcting for this misalignment at high temperature. The quantum well width containing the energy levels 3-4 was reduced. The layer sequence for this structure, starting from the injection barrier, is **6.3**/7.0/**3.2**/5.6/**5.6**/6.3/**1.2**/5.6/**5.2**/<u>6.1</u>/**1.0**/7.4, where bold and underlined text are barrier and doped layers, respectively. The L-I and I-V characteristics are shown in Fig. 2-8. The maximum operating temperature increased slightly to T_{max} = 173 K, but we still observed the dual lasing peak feature at device rollover. More detailed simulations would have to be carried out to understand this effect.

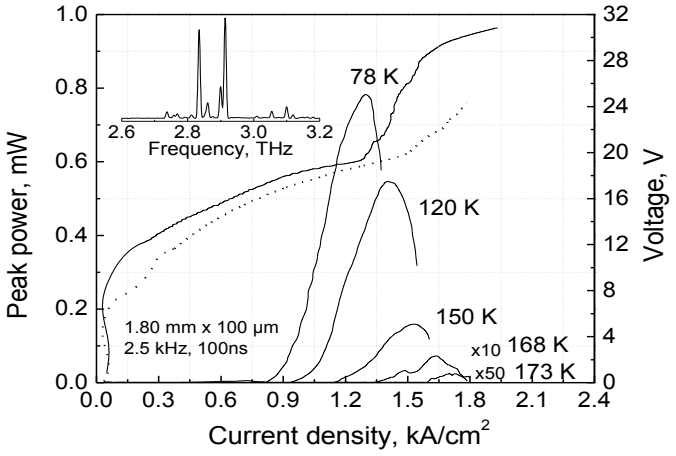

Figure 2-8, L684 modified two-phonon resonant active region design performance: Current-voltage (I-V) and light output-current (L-I) characteristics of the modified double-phonon device, operated with 100ns pulses at different temperatures. Solid I-V lines represent device operation at 78K and dashed I-V lines represents device operation at 173 K. Inset: Device spectra near the peak output power at 78K.

2.3 Conclusion and outlook

We've shown that a double-phonon resonant band structure reduces the thermal backfilling of the lower laser level and increases the maximum operating temperature operation compared to a single-phonon counterpart. However the lack of significant improvement in T_{max} indicates that there are other physical mechanisms preventing the high temperature operation of QCLs. In particular, it becomes difficult to selectively inject of carriers into the upper laser state at high temperature due to transition linewidth broadening. Nevertheless active work is still being done to improve the temperature performance. Since the completion of this work, the maximum operating temperature of QCLs has increased to ~ 200 K using copper metal-metal waveguides, novel active

region designs, and implementing minor changes such as the elimination doped contact layers at the expense of higher voltage operation. Despite all these improvements, THz QCLs are still more than 50 K away from even thermoelectric-cooled operation and the march towards higher temperature operation has slowed considerably. Different active region architectures are being explored for room-temperature performance. We have looked into structures with multiple compositions for the barrier material in the active region and simulations indicate that gain up to 240 K is possible [52]. But experimental results haven't produced devices operating at temperature higher than 188 K [53]. Other material systems are being explored for THz QCL construction. GaN-based heterostructures are promising considering that the LO-phonon energy is 90 meV and would reduce the LO phonon scattering of upper state carriers at high temperatures [54, 55]. However, the dislocation density in a nitride superlattice is prohibitively large and degrades the transport and spontaneous emission lifetime of carries. Significant improvement in the material quality is required. Strained Si_xGe_{1-x} heterostructures are also promising for high temperature lasing [56], but the material quality is not good enough at this point. Additionally, they are complicate to model since the hole transitions in the valence band would dictate lasing (given the larger barrier offset compared to the conduction band).

Chapter 3: Design of a Terahertz Intersubband Raman Laser

Terahertz quantum cascade lasers cannot maintain population inversion at temperatures greater than 200 K and therefore cease to lase. However, the problem of creating a room-temperature THz semiconductor laser may be overcome by designing a laser that does not require population inversion across the THz transition. In particular, the concept of Raman gain may be used to produce laser action in materials where population inversion is difficult to achieve. This chapter will describe the Raman gain process using intersubband transitions in GaAs-AlGaAs multiple quantum well systems and describe an experimental approach of realizing THz Intersubband Raman Lasers (IRL).

3.1 Background

The *spontaneous Raman effect* is a third-order nonlinear optical process first demonstrated by C.V Raman the 1920's and is characterized by the inelastic scattering of light by a medium. From a quantum mechanics viewpoint, an incident photon with energy $\hbar\omega_p$ is either scattered into a photon with lower energy given as $\hbar\omega_s = \hbar\omega_p - \hbar\nu$ (Stokes) or a photon with larger energy given as $\hbar\omega_{as} = \hbar\omega_p + \hbar\nu$ (anti-Stokes). The difference in energy, $\hbar\nu$, between the incident and scattered photon is referred to as the Stokes-shift and typically corresponds to the rotational, translational or vibrational phonon modes of the scattering medium. The Stokes and anti-Stokes scattering efficiency is no larger than $10^{-8} - 10^{-6}$, however it's an extremely powerful analytical method for the spectroscopic studies of a wide variety of materials [57, 58].

A portion of this work has been published in K. Vijayraghavan, R.W. Adams, Q.J. Wang, J. Fan, F. Capasso, S. Khanna, L. Li, A.G. Davies, E. Linfield, M. Belkin, "Intersubband Raman laser for operation at terahertz frequencies", *36th International Conference on Infrared, Millimeter, and Terahertz Waves* , Houston, TX (Oct. 2011). All authors contributed to this work.

In the early 1960s, *stimulated Raman scattering* was fortuitously demonstrated by a team at the Hughes Research Labs and marked the birth of the first Raman laser [59]. HRLs initial studies focused on experiments with an optically pumped Q-switched Ruby laser emitting at λ = 694 nm. Spectral measurements of the laser revealed strong secondary emission at λ = 767 nm, despite this wavelength being well outside the gain bandwidth of the Ruby medium. It was later explained that the secondary emission originated from the Stokes scattering of the primary wavelength by a nitrobenzene-filled Kerr cell used in Q-switching! A critical feature of their setup was the laser cavity end facets that provided optical feedback at the Stokes wavelength. Raman lasing is described schematically in Fig. 3-1(b). The gain medium is placed in a resonant cavity and optically pumped. The pump laser induces Stokes emission that is reflected back into the Raman gain media by the cavity reflecting facets. This in turn drives a stronger excitation oscillation within the gain medium and exponentially increases the Stokes scattering of the pump. This positive feedback effect continues until steady-state lasing takes place, provided there is sufficient Raman gain at the Stokes wavelength to overcome the cavity loss. An expression for the steady state Raman gain at the Stokes frequency is given as [1],

$$g(\omega_S) = -\frac{\omega_S}{c\, n_{eff,\omega_S}} \mathrm{Im}\left(\chi^{(3)}\right) \times \frac{2 I_P}{n_{eff,\omega_P} \varepsilon_0 c} \tag{3.1}$$

where ω_S is the stokes frequency, $\chi^{(3)}$ is the third-order optical susceptibility, I_P is the external pump intensity, $n_{eff,\omega S}$ is the Stokes mode refractive index, and $n_{eff,\omega p}$ is the pump mode refractive index.

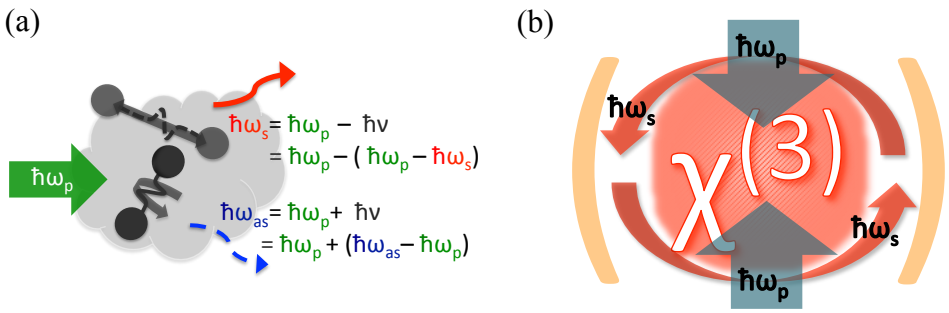

Figure 3-1, Raman scattering: (a) Photon description of spontaneous Raman Stokes and anti-Stokes scattering. (b) Stimulated Raman scattering occurs by placing the Raman gain media (red) in a cavity resonator with reflectors (yellow). When the medium is externally pumped (blue), Stokes emission (red) occurs and gets amplified in the resonator. When the Raman gain exceeds the cavity loss at the Stokes wavelength, steady-state lasing takes place.

Raman lasers have been constructed with a variety of optical crystals [60], gases [61], fibers [62], and semiconductors [63-67] Table 3-1 lists the parameters of some common Raman gain media. Many fiber and solid-state crystal Raman lasers have a transparency window in the visible to near-infrared frequencies and phonon-based Raman shifts ranging from 500 cm^{-1} to 1500 cm^{-1}. Additionally, they possess small third-order optical nonlinearity coefficients around $\chi^{(3)} \sim 10^{-16}$ - 10^{-15} cm^2/V^2 that result in Raman gain coefficients on the order of 10 – 100 cm/GW. Overall they are best suited for near-infrared and infrared Raman lasing using strong visible/infrared pump lasers. Given the high THz material loss and small gain coefficients, extending Raman lasing to THz frequencies using solid-state crystals would require prohibitively large pump powers that would go beyond the material damage threshold. Additionally, pumps would experience huge loss since they would operate outside the material transparency window.

Semiconductors with optical nonlinearity have been used as Raman gain material and the most prominent device is the silicon Raman laser demonstrated by Intel in 2005 [64]. The initial design comprised of a sequined silicon rib-waveguide 48-mm in length and pumped by near-IR laser at λ = 1064 nm. This marked the first demonstration of room temperature lasing with silicon. Currently, the size and pump thresholds have considerably dropped and is a promising development for photonic circuits. However, extension of THz Raman emission with silicon is not feasible given the small stokes shift for telecom laser based pumping.

Material	Pump wavelength	Stokes shift	Stokes wavelengh	Raman gain coefficient
$Ba(NO_3)_2$	0.35 – 1.8 μm	1,046 cm^{-1}	0.36 – 2.21 μm	11 cm/GW
$LiIO_3$	0.38 – 3.5 μm	770–848 cm^{-1}	0.39 – 5 μm	4.8 cm/GW
Silica fiber	1.3 – .155 μm	440–470 cm^{-1}	1.38 – 1.67 μm	20 cm/GW
H_2	10.60 μm	415 cm^{-1}	18.92 μm	10 cm/GW
Silicon	1.3 - 1.55 μm	625 cm^{-1}	1.41 – 1.71 μm	10 cm/GW
GaAs intersubband quantum wells	10.60 μm	385 cm^{-1}	15 μm	10,000 cm/GW

Table 3-1, Raman gain material properties: Solid state, gas and semiconductor Raman gain material.

An alternative semiconductor Raman laser is based on intersubband (ISB) transitions in multiple quantum well structures [65-67]. The Stokes-shift is based on electronic transitions of carriers between subband states in the conduction band. It can be specifically engineered by controlling the energy spacing between subband states by varying the width of the quantum wells and barriers. Additionally, the energy level spacing between states can be tailored to match the resonance of the external pump. For a three-level system, as shown in Fig. 3-2, an expression for the optical nonlinearity in perfect resonance is given as [57, 67, 68],

$$\chi^{(3)} \approx -\frac{e^4}{\hbar^3 \varepsilon_0} \frac{(z_{13})^2 (z_{23})^2}{i\Gamma_{13} \times i\Gamma_{12} \times i\Gamma_{23}} (N_1 - N_3) \tag{3.2}$$

where N_i, qz_{ij} and Γ_{ij} is the electron concentration in state i, the transition dipole moment and transition linewidth broadening between states i-j, respectively. ISB quantum well structures can be designed with $\chi^{(3)}$ more than $10^3 - 10^4$ times larger than bulk crystals and semiconductors. This significantly reduces the device size, pump threshold power, and provides enough gain to overcome THz cavity losses. Mid-infrared ISB Raman lasing was first demonstrated with a 2 quantum well design made in the GaAs/$Al_{0.35}Ga_{0.65}As$ materials system [66]. These structures were optically pumped by a tunable CO_2 laser emitting around λ = 10.6 μm and Raman emission centered at λ = 15 μm was observed. Soon after mid-IR ISB Raman lasing was demonstrated with optically pumped InGaAs/InAsAs multi-quantum wells [65] and electrically pumped InP/InGaAs/InAlAs QCLs [67].

Extending IRL operation to the THz range requires innovation on two fronts. First the active region must be designed to provide a large enough Raman gain to overcome higher THz waveguide losses. Secondly, the Raman laser waveguide must provide confinement for both the THz and the mid-infrared pump modes.

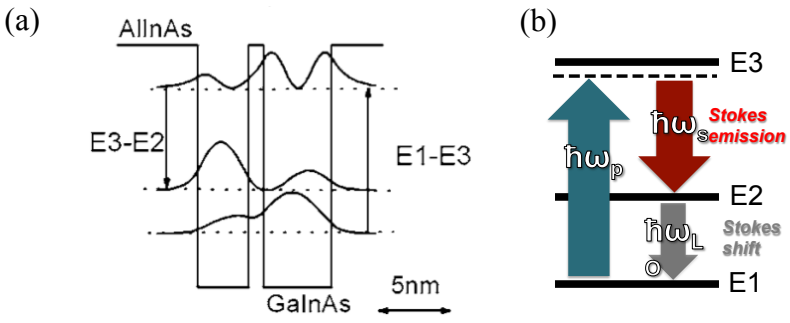

(Figure 3-2 continues on next page)

Figure 3-2, Raman gain with quantum wells (figure started on previous page): (a) Two quantum well, three energy level system for a mid-IR Raman laser. Figure reprinted from Ref. [65]. (b) Energy level schematic of the Raman process using intersubband transitions in quantum wells. The Raman shift is determined by the energy level 1-2 separation. The pump and Stokes emission is in resonance with the 1-3 and 2-3 transitions, respectively.

3.2 Waveguide design

The laser waveguide must provide low-loss confinement of the THz mode and support propagation of the mid-IR pump. Devices were modeled as a ridge waveguide, as depicted in Fig. 3-3(a). The mid-IR pump couples into a ridge waveguide laterally along the length of the cavity. This configuration has several advantages compared to pumping through the laser facet. Lateral pumping does not require thick cladding layers for mid-IR modal confinement since the propagation distance is only a few hundred microns i.e. the device width. The absence of these cladding layers significantly reduces the epitaxial thickness (hence cost of structures) and increases the THz mode overlap with the active core. Additionally, the intra-cavity mid-IR field intensity is uniform for lateral pumping due to smaller propagation loss compared to facet pumping in which the mid-IR field intensity varies by at least 20% end-to-end for a 2-mm long device. As a result, a constant Raman gain coefficient is possible with a lateral pump scheme.

In this work, a semi-insulating surface plasmon waveguide and a double metal waveguide commonly implemented for high-power and high-performance THz QCLs, respectively, was investigated. The mode profile for a semi-insulating surface plasmon waveguide was simulated using COMSOL MultiPhysics and is shown in Fig. 3-3(b). Modal confinement is achieved with surface plasmon modes propagating along the metal

contact deposited on top of the ridge and a highly-doped semi-metallic GaAs layer positioned on top of a semi-insulating GaAs substrate. The semi-metal GaAs guiding layer is 200 nm-thick and doped at $n = 5x10^{18}$ cm^{-3} such that $\varepsilon < 0$. It should be noted that a significant portion of the THz mode leaks into the substrate and a greater amount of THz power out couples to free-space via substrate facet emission. For a 4-mm long device with a back facet HR coating, the computed waveguide loss, mirror loss, and modal overlap at 4 THz are 4.5 cm^{-1}, 1.4 cm^{-1}, and 22%, respectively. THz Raman gain of at least 27 cm^{-1} is required in the active region to start lasing for this waveguide.

The mode profile for a double-metal waveguide is given in Fig. 3-3(c). The THz active medium is sandwiched between two gold surfaces and the configuration is similar to a microwave microstrip antenna resonator. The impedance mismatch between the laser cavity and free-space is near unity due to outcoupling the mode through a sub-wavelength aperture (10 μm thick active region). As a result, excellent modal confinement is achieved albeit very small THz output power is outcoupled to free-space. The calculated waveguide loss, mirror loss, and modal overlap at 4 THz is 14 cm^{-1}, 0.8 cm^{-1}, and 0.97, respectively. THz Raman gain of at least 16 cm^{-1} is required in the active region to start lasing for this waveguide.

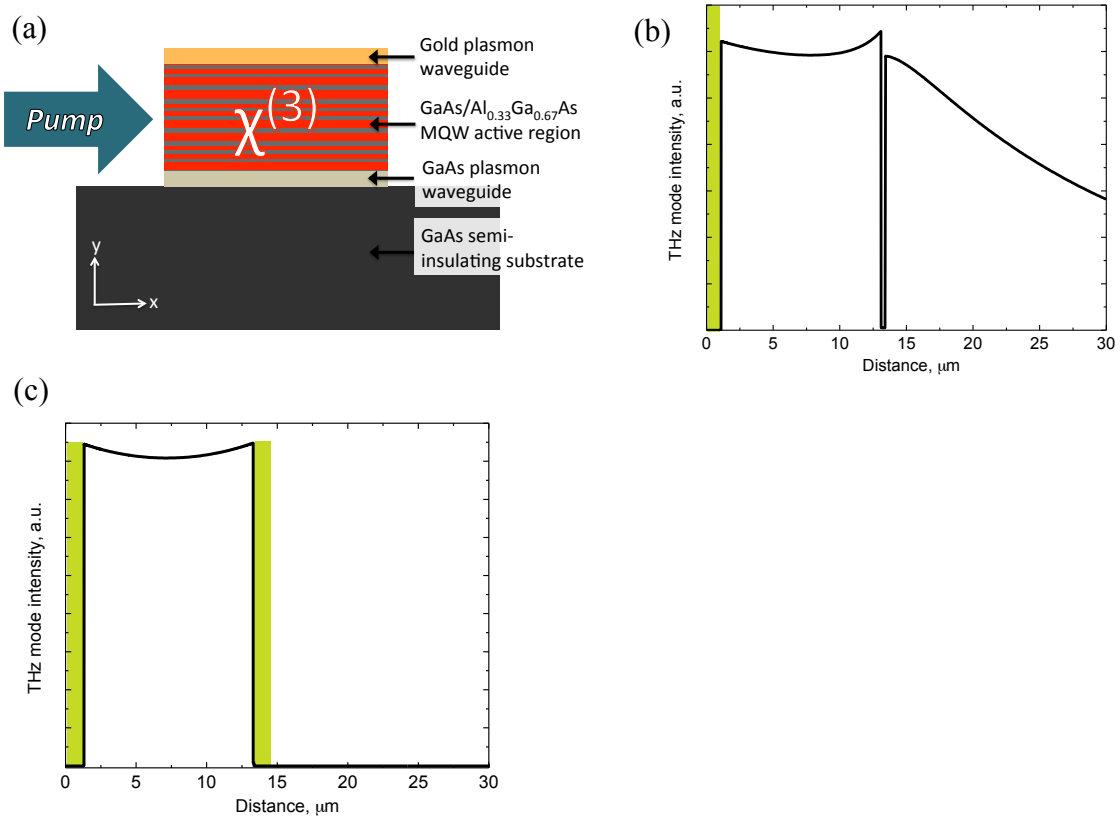

Figure 3-3, Waveguide profile: (a) cross section of the waveguide. The laser is pumped uniformly along its length (z-axis out of the page) and the THz emission is in to the x-y plane. (b) THz modal profile with a semi-insulating plasmon waveguide. (c) THz mode profile with a metal-metal waveguide.

3.3 GaAs-$Al_{0.33}Ga_{0.67}As$ multiple quantum well active region design

Our THz Raman gain medium is composed of multi-quantum wells made with the GaAs-$Al_{0.33}Ga_{0.67}As$ heterostructure system. A 1D self-consistent Schrodinger-Poisson solver was used to simulate the band structure. We first designed a simple two quantum well active medium – similar to successful intersubband mid-IR Raman designs – and Fig. 3-4(a) shows a single period of the conduction band diagram comprising of 2 well-barrier

pairs. The essential quantum well/barrier material parameters used in the simulation is listed in Table 3-2. The layer sequence and key parameters of this structure is listed in the Fig. 3-4 caption. The barriers are modulation doped n = 5 x 10^{16} cm^{-3} and spatially separated from the active quantum wells to reduce inhomogenous linewidth broadening due to impurity scattering. The average doping was n = 5x10^{15} cm^{-3}, similar to THz QCLs. The Stokes Raman emission is resonant with states 2-3 and is maximized at 4 THz when the external pump is tuned in resonance with 1-3 transition at λ = 10.60 μm. Using Eq. 3.1 and Eq. 3.2, the room-temperature Raman gain is computed and plotted as a function of pump intensity as shown in Fig 3-4(b). Mid-IR and THz transition linewidths of Γ_{MIR} = 7.5 meV and Γ_{THz} = 5 meV, respectively, were used for simulations and are based on values reported in literature for similar quantum well systems [65, 66]. The Raman gain increases monotonically with pump intensity and easily surpasses the gain threshold. However, Eq. 3-2 neglects to take into account power broadening of the upper Raman state due to Rabi coupling of the quantum well ground state and upper state 3, and does not consider carrier saturation at high pump intensities. If we account for these two effects, the quantum mechanical expression for the third-order susceptibility for this structure is given as [57, 67, 68],

$$\chi^{(3)} \approx -\frac{q^4}{\hbar^3 \varepsilon_0} \frac{(z_{13})^2 (z_{23})^2}{(\omega_{13} - \omega_P + i\Gamma_{13}) \times i\Gamma_{14} \times \left(\omega_{23} - \omega_S + i\left(\Gamma_{23} + \Omega^2 / \Gamma_{12}\right)\right)} \frac{(N_1 - N_3)}{1 + \Omega^2 \tau_3 / \Gamma_{13}} \qquad (3.3)$$

where q is the electron charge, N_i is the unsaturated population at level i, z_{ij} is the dipole moment between states i and j, Γ_{ij} corresponds to the energy linewidth at level j, and Ω corresponds to the Rabi frequency of the pump. The power (Rabi) broadening of states at

large pump intensities is accounted for by replacing THz transition linewidth Γ_{23} with $\Gamma_{23} + \Omega^2/\Gamma_{13}$. The expression for the Rabi broadening is given as [67],

$$\Omega = \frac{q \cdot z_{13}}{\hbar} \sqrt{\frac{2 \cdot I_{pump}}{\varepsilon_0 c n_{\omega 13}}} \tag{3.4}$$

where I_{pump} and $n_{\omega 15}$ is the pump intensity and modal refractive index, respectively. Additionally, optical pump saturation at high intensity is modeled by replacing $(N_i - N_j)$ in Eq. 3-2 with $(N_1 - N_3) / (1+\Omega^2\tau_3/\Gamma_{13})$. Finally, the expression includes the case in which the pump and Stokes emission is detuned from the resonant transitions. Accounting for power broadening and saturation, the Raman gain plotted in Fig. 3-4(b) and is significantly smaller than the required threshold gain for either THz waveguide configuration.

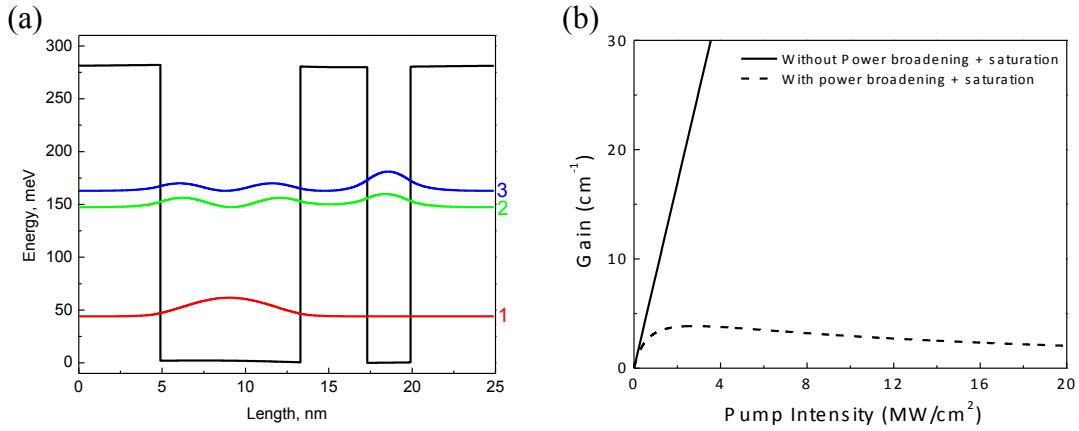

Figure 3-4, two quantum well Raman active medium (continued on next page): (a) Conduction band energy diagram of the proposed Raman gain section. The layer sequence from left to right is **25**/**25**/84/**40**/26/**25**/**25**, with barriers in bold and doped layers underlines. Energy level separations are E_{13} = 121 meV, E_{12} = 105 meV, and E_{23} = 16 meV. Levels 2-3 is resonant with the THz Raman Stokes emission, 1-3 resonant with the external pump, and 1-2 corresponding to the Stokes shift. The transition dipole

moments are z_{13} = 0.98 nm , z_{12} = 0.71 nm and z_{14} = 4.50 nm. The lifetime of state 2 and 3 is τ_2 = 1.66 ps and τ_5 = 1.15 ps. (b) The simulated Raman gain versus pump intensity with (black dashed line) and without (solid line) bradening and saturation effects.

Material	**ΔE_C w/ respect to GaAs (meV)**	**m_{eff} (m_0)**	**Υ m^{-1}**
GaAs	0	0.067	4.9×10^{-19}
$Al_{0.33}Ga_{0.67}As$	294	0.085	2.97×10^{-19}

Table 3-2, GaAs IRL material properies: GaAs- $Al_{0.33}Ga_{0.67}As$ Material parameters used in simulations.

A three quantum well active medium was designed to increase the Raman gain and a single period of the band structure is shown in Fig. 3-5(a). The layer sequence and other design parameters are given in the figure caption. The Stokes Raman emission is resonant with states 3-4 and is maximized at 4 THz when the external pump is tuned in resonance with 1-3 transition at λ = 10.60 μm. The extra quantum well serves to increase the spatial overlap of states 3-4 and thereby enlarging the transition dipole moment z_{34}. Additionally, energy state 2 is engineered to be separated from state 3 by a LO-phonon, thereby reducing the upper Raman state lifetime. However, the lifetime of state 2 is long - 1.5 ps – due to a large energy separation from state 1 and is a bottleneck for efficient scattering of carries back into the ground state. The average doping in this structure was 5 x 10^{15} cm^{-3} and the room-temperature Raman gain is plotted in Fig. 3-5(b). While the Raman gain is significantly larger compared to the two quantum well system, it still is less than the threshold gain required for either waveguide schemes.

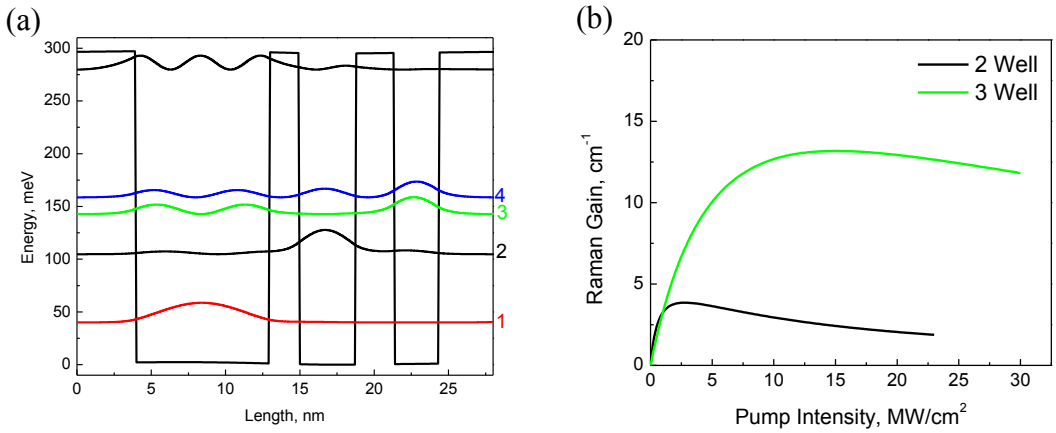

Figure 3-5, Three quantum well Rama active medium: (a) Conduction band energy diagram of the proposed Raman gain section. The layer sequence from left to right is **20**/**20**/90/**20**/38/**26**/30/**20**/**20,** with barriers in bold and doped layers underlines. Energy level separations are E_{14} = 122 meV, E_{13} = 105 meV, E_{34} = 17 meV, E_{23} = 40 meV, and E_{12} = 65 meV. Levels 1, 3, and 4 are used to produce giant Raman nonlinearity. The transition dipole moments are z_{14} = 1.0 nm , z_{34} = 6.3 nm and z_{13} = 0.40 nm. The lifetime of state 3 and 4is τ_3 = 0.32 ps and τ_4 = 0.4 ps. (b) The simulated room-temperature Raman gain versus pump intensity for 3 QW system (green). For comparison, the 2 QW Raman gain (black) is shown.

To further increase the Raman gain, a four quantum well-barrier system was designed and a single period of the band structure is shown in Fig. 3-6(a). Specific design principles were followed to optimize $\chi^{(3)}$. The structure was designed to maximize the product $z_{45}\times z_{15}$. This was best achieved by increasing the number of quantum well and barrier pairs to maximize the spatial overlap between wave functions. To increase optical saturation intensity, the electron lifetimes in the states 4 and 5 are designed to be minimized through resonant longitudinal optical (LO) phonon scattering of electrons from states 4 and 5 to states 2 and 3. The energy separation between states 1 and 2, 2 and 3, and 3 and 4 is approximately 36 meV which corresponds to the LO phonon energy in

GaAs. The Raman gain versus pump intensity at 78K and room-temperature is plotted in Fig 3-6(b). For simulations, the mid-IR transition linewidth at 78 K and 300 K were chosen as Γ_{MIR} = 5 meV and Γ_{MIR} = 7.5 meV, respectively, and the THz transition linewidth at 78 K and 300K were chosen as Γ_{THz} = 2.5 meV and Γ_{THz} = 5 meV, respectively. The low-temperature gain peaks at 60 cm^{-1} at 6 MW/cm^2 before pump saturation sets in. The room-temperature gain plateaus to 30 cm^{-1} at 15 MW/cm^2. The large discrepancy between the Raman gain at low- and room-temperature is attributed to the broadening of state linewidths at elevated temperatures due to increased LO phonon scattering. In both cases there is sufficient Raman gain to overcome the cavity losses in both waveguide configurations. Also plotted in Fig 3-3 (c,d) are the values for $\chi^{(3)}$ and Raman gain versus pump detuning. At perfect resonance, the low-temperature $\chi^{(3)}$ peaks at 3.5 x 10^{-10} cm^2/V^2 at the Stokes wavelength – more than 4 orders of magnitude larger than any bulk crystal or semiconductor medium.

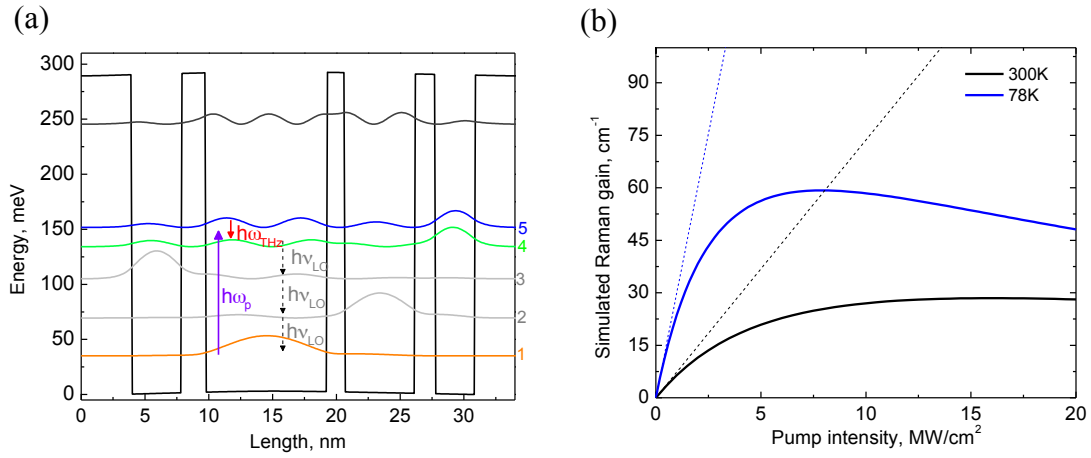

(Figure 3-6 continues on next page)

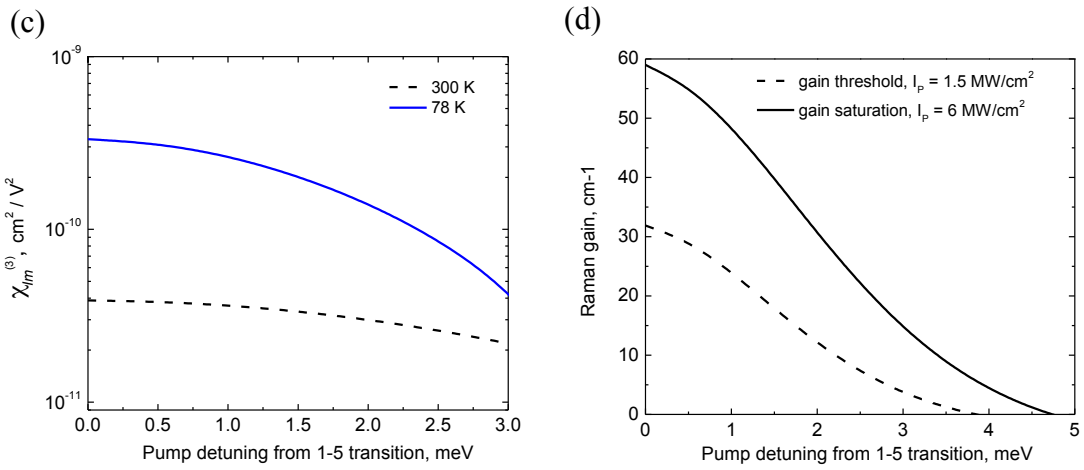

Figure 3-6, Raman Laser design (started on previous page): (a) Conduction band energy diagram of the proposed Raman gain section. The layer sequence from left to right is **20**/**20**/39/**19**/95/**14**/55/**16**/31/**20**/**20,** with barriers in bold and doped layers underlines. Energy level separations are E_{15} = 119 meV, E_{14} = 102 meV, E_{14} = 17 meV, E_{34} = 30 meV, E_{23} = 36 meV and E_{12} = 36 meV. Levels 1, 4, and 5 are used to produce giant Raman nonlinearity. The transition dipole moments are z_{15} = 0.63 nm , z_{45} = 7.7 nm and z_{14} = 0.79 nm. The lifetime of state 4 and 5 is τ_4 = 0.4 ps and τ_4 = 0.35 ps. (b) The simulated Raman gain versus pump intensity at 78 K (blue solid) and 300 K (black solid). Also shown is the gain without taking into account power broadening and saturation effects (dashed lines).

The four quantum well structure with a semi-insulating surface plasmon waveguide design was grown by Leeds University using molecular beam epitaxy. A semi-insulating GaAs substrate was used and growth started with 250-nm thick undoped GaAs buffer layer, followed by a 300 nm-thick GaAs plasmon waveguide layer doped n=2x10^{18} cm^{-3}, followed by 363 repetition of the $Al_{0.33}Ga_{0.67}As$-GaAs MQW active region, and ended with a 50-nm thick GaAs cap layer doped n = 5x10^{18} cm^{-3}. Samples were processed into 80 – 300 μm-wide deep-etched ridge waveguides and the processing steps are shown in Fig 3-7. The top metal waveguide was first defined using an image-

reversal lift off process and consisted of a 5 nm-thick Ti adhesion layer followed by a 500 nm-thick Au waveguide layer deposited by electron beam evaporation. The Au strips also served as a self-aligned etch mask for the deep ridge etch. Etching was carried out with an Oxford 100 ICP RIE using a BCl_3 and Ar gas combination. The depth of the ridge etch was approximately 12μm and equal to the active region thickness. Samples were then cleaved into 1mm – 4mm long bars just along the edge of the ridge. A back facet HR coating consisting of Al_2O_3(120 nm)/ Au (60nm) was applied to select devices.

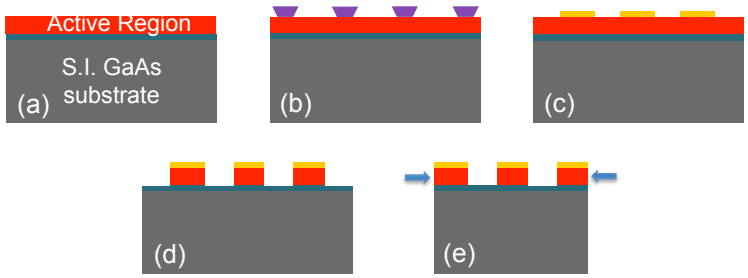

Figure 3-7, Processing steps: (a) A bare wafer showing the active region (red), GaAs plasmon waveguide layer (blue) and substrate (grey) (b) Ridge waveguide patterning is first carried out using an image reversal photolithography (c) Electron-beam deposition and liftoff leaves gold stripes on the sample (d) The waveguide is etched in the ICP RIE using the gold stripes as an etch mask (e) Samples are then cleaved along the waveguide length.

A schematic of the THz measurement setup is shown in Fig. 3-8. Testing was done at room-temperature and 78 K. Devices were optically pumped laterally along the waveguide and carefully cleaved such that the substrate and pumped facet were planarized. Laser bars were indium bonded to copper heatsinks, mounted in a vacuum cryostat, and pumped with a MTL-3 Mini TEA CO2 laser manufactured by Edinburgh Instruments. The pump laser operated with 50 ns wide pulses at a 5 x 10^{-4} % duty cycle. The emission was polarized in the vertical direction (growth direction) and grating tuned

to emit at specific wavelengths between λ = 9.2 μm – 10.8 μm. Typical pulse energies were between 20mJ/pulse - 70mJ/pulse, depending on the emission line. Two gold-coated mirrors were used to steer the pump beam and a ZnSe cylindrical lens focused the beam to a 5.5 x 0.3 mm^2 spot size. For a 2 mm-long and 12 μm-thick device, and accounting for 28% semiconductor-air facet reflectivity, less than 5% of the pump light was coupled into the waveguide.

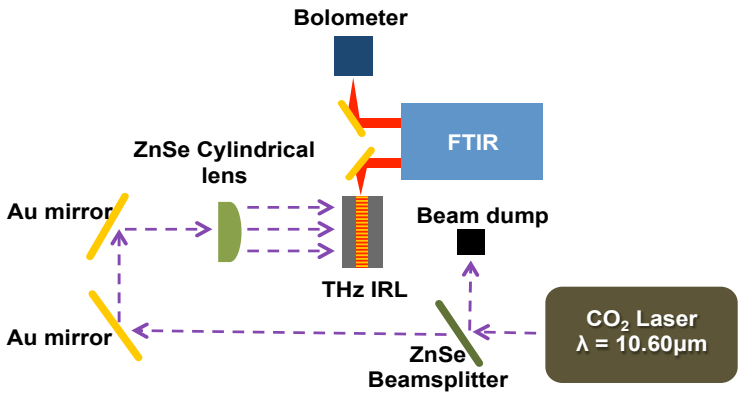

Figure 3-8, THz Raman measurement setup: Schematic of the measurement setup for testing Raman lasers. The pump laser was polarized in the vertical direction (in the plane of the phase) The ZnSe beam splitter has 95% transmission and the reflected laser power was directed to a beam dump or energy meter to monitor the pulse energy.

Various HR coated devices ranging from 80 – 300 μm in width and 1 – 4 mm in length were tested but THz emission was not observed. Intersubband absorption measurements were taken to verify that the quantum well resonances matched the designed parameters. Samples were cleaved into 6 x 2 mm^2 bars, gold coated on the front and back surfaces, and employed a multipass geometry to increase the absorption path length through the active core. The input and exit facets were polished at a 45° angle normal to the sample surface to achieve this. Broadband mid-IR light from a Fourier

transform IR spectrometer was modulated at 1 kHz by a mechanical chopper and coupled in normal to the polished facet. A LN_2 MCT detector collected the signal. Spectral measurements were taken using a time-resolved step scan with a 10 cm^{-1} resolution. A polarizer placed in front of the sample discriminated between the TM-polarized signal and TE-polarized background. However, clear absorption features were not discernable. The lack of any absorption features is indicative that the carrier concentration was smaller than expected. This could be due to the incomplete ionization of dopants in the barriers. For this particular structure, the $Al_{0.33}Ga_{0.67}As$ barriers are doped to minimize the linewidth broadening in the active quantum wells and there is evidence [69] that suggests incomplete ionization dopants for this barrier composition is the cause for small free carrier concentration. According to Ref. [69], deep-level donor states dominate for the $Al_{0.33}Ga_{0.67}As$ composition and the activation energy is E_D = 0.13 eV. In a bulk material, the ionized donor concentration can be roughly estimated using,

$$N = \frac{N_D}{1+g_D \cdot e^{(E_F - E_D)/kT}} \tag{3.5}$$

where N_D is the donor concentration, E_F is the Fermi level, E_D is the dopant activation energy, and g_D is the ground state degeneracy of the dopant (~2 for AlGaAs). A doping density of $N_D = 5x10^{16}$ cm^{-3} results in an active carrier concentration $N = 10^{15}$ cm^{-3}. As a result the Raman gain is 5 times smaller than expected and insufficient to overcome the THz losses.

3.4 Design and experimentation of GaAs-$Al_{0.33}Ga_{0.67}As$ Raman laser with modulation doped quantum wells and metal-metal waveguide

An optimized 4 quantum well active region with larger Raman gain compared to the initial structure was designed. One period of the conduction band diagram is shown in Fig. 3-9(a). The layer sequence and relevant parameters are given in the figure caption. The ground state wavefunction was designed to be localized in the widest well. Levels 4 and 5 (Raman transition) were designed to anti-cross in wells 1 and 4, thereby extending their wave functions over all four wells, resulting in a large z_{45}. The GaAs quantum wells were modulation doped to avoid incomplete ionization of carriers. While doping of the well increases the linewidth broadening of states due to ion scattering, the broadening is not expected to be significant given the low doping density. As a precaution the 35 Å well was doped given the reduced overlap of wave functions in it. Compared to the previously designed structure, the average doping was increased to $n = 9.4 \times 10^{15}$ cm^{-3} and leads to a factor of two enhancement of $X^{(3)}$. Transition dipole moment z_{45} was slightly larger, while z_{15} was reduced to increase the saturation intensity. Finally, the carrier lifetime of the upper Raman state was reduced by nearly a factor of two to mitigate the effects of pump saturation. The Raman gain profile versus pump current for this structure is shown in Fig. 3-9(b).

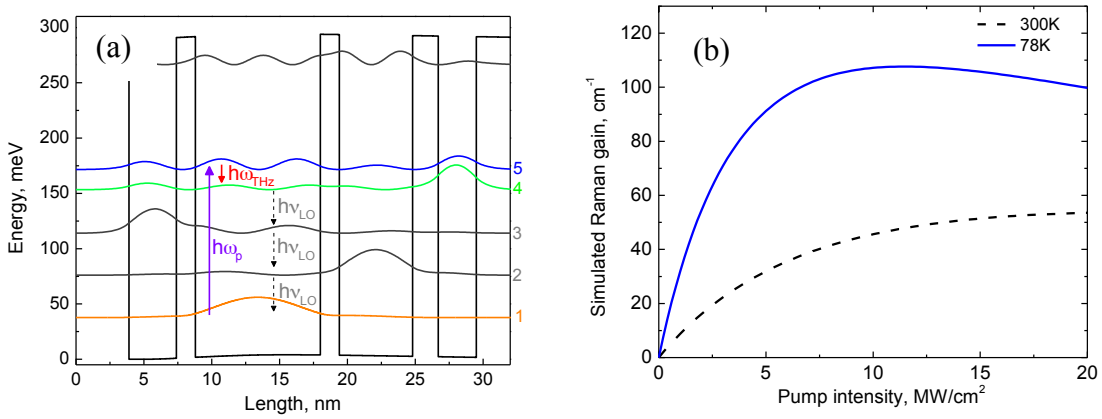

Figure 3-9, L793 Raman Laser design: (a) Conduction band energy diagram of the proposed Raman gain section. The layer sequence from left to right is **40**/35/**14**/92/**14**/54/**19**/28/**40,** with barriers in bold and doped layers underlines. Levels 1, 4, and 5 are used to produce giant Raman nonlinearity. The energy state separation are E_{15} = 133 meV, E_{14} = 117 meV, E_{45} = 16 meV, E_{34} = E_{23} = E_{12} = 39 meV. The transition dipole moments are z_{15} = 0.63 nm , z_{45} = 7.9 nm and z_{14} = 0.39 nm. The lifetime of state 4 and 5 is τ_4 = 0.4 ps and τ_4 = 0.35 ps. (b) The simulated Raman gain versus pump intensity at 78 K (blue solid) and 300 K (black solid).

The structure was designed with a double-metal waveguide for THz mode confinement given the significantly reduced threshold gain. similar to the THz QCLs described in the previous chapter. Following the laser "gain = loss" requirement, the pump threshold is expected to be only 400 kW/cm^2 at low-temperature and 2 MW/cm^2 at room-temperature.

Samples were fabricated into ridge waveguides and the same processing steps to fabricate THz QCLs in the previous chapter were carried out. Devices ranging from 1mm - 4 mm in length and 80 μm - 300 μm in width were tested. Despite the improvements in the design and waveguide, lasing was not observed.

Intersubband measurements were taken to verify the quantum well energy level positioning and the results are plotted along with a simulated absorption spectrum in Fig. 3-10. The theoretical absorption spectrum was calculated with an expression given as

$$\alpha = \frac{\omega_p}{c}\,\mathrm{Im}\left(\sum_{k=2}\frac{\left(q\cdot z_{1k}\right)^2\left(N_1 - N_k\right)}{3\cdot\varepsilon_0\left(\hbar\omega_{1k} - \hbar_p - i\Gamma_{1k}\right)\left(\hbar\omega_{1k} + \hbar_p + i\Gamma_{1k}\right)}\right) \tag{3.6}$$

where the term in the bracket is the quantum mechanical expression for first-order susceptibility $\chi^{(1)}$ summed over all transitions from the ground state to higher lying states *k*. Mid-IR linewidths were the same as previously stated and an average carrier population of N = 9 x 10^{15} cm^{-3} was assumed. The measured spectrum has two small absorption peaks that are slightly shifted from the expected 1-4 and 1-5 transition resonance. However, the absorption strength was considerably smaller than expected and could only provide a qualitative understanding of the design. Despite doping of the quantum wells, the carrier concentration once again is smaller than expected. Doping calibration and hall measurements would need to be carried out in conjunction with the structure growth to accurately determine the carrier concentration.

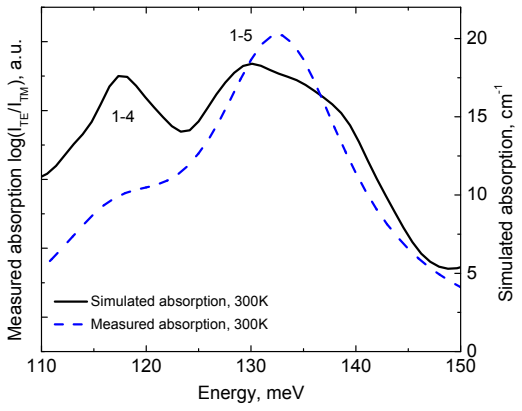

(Figure 3-10 continues on next page)

Figure 3-10, L793 mid-IR absorption profile (started on previous page): The measured spectrum (black solid line) is considerably weaker in absorption strength compared to the simulated spectrum (blue dashed line).

3.3 Outlook and future directions

Low-temperature and room-temperature THz Raman lasing was not observed for the aforementioned designs. There are a few factors that make this experiment highly challenging. The external CO_2 laser pump operates with an extremely low duty cycle of $5x10^{-4}$%. Despite using high-sensitivity bolometer detection and lock-in collection methodology, the average power is probably prohibitively small. To test this idea, a THz QCL with a peak power around 1 mW was operated with 50ns pulse width and 100 Hz repetition rate. The bolometer could not detect a signal. A pump source with a significantly larger duty cycle is required. Over the course of the experiment, laser induced damage on the GaAs ridge and gold metal contact was observed at pump intensities slightly above threshold. Upon further study, it was discovered that GaAs has a surface damage threshold of 100 kW [66] and restricts the maximum focused intensity to 15 MW/cm^2. This limits the dynamic range of the device and is particularly problematic if the threshold intensity is larger than simulations indicate. In addition to underestimating the carrier concentration in structures, the linewidth for both mid-IR and THz transitions may have been underestimated, particularly at room-temperature [70]. More recent experiments done in our lab for similar quantum well structures have room-temperature transition linewidths in the 10 meV – 20 meV range. The THz Raman gain is not sufficient to overcome cavity losses if the mid-IR transition linewidths are in this range.

While we have thoroughly optimized the quantum well structure to achieve the maximum Raman gain at THz frequencies, slight improvements can be made by designing and fabricating structures with different materials systems. In particular the $In_xGa_{1-x}As$-$In_yAl_{1-y}As$/InP heterostructure system is appealing given its physical properties and technological maturity. Larger oscillator strengths at THz frequencies can be designed with this materials system because it has a considerably smaller effective mass and requires wider quantum wells to maintain the same energy level separations compared to the GaAs-AlGaAs system. One period of a 4 quantum well $In_{0.53}Ga_{0.47}As$-$In_{0.52}Al_{0.48}As$ structure is shown in Fig. 3-11 and the material parameters used in simulation is given in Table 3-3. More realistic room-temperature mid-IR and THz transitions linewidth of Γ_{MIR} = 12 meV and Γ_{THz} = 5 meV were used in modeling and a pump threshold of 6 MW/cm^2 is required to match the loss with a double-metal waveguide design. If this project continues, it would be worthwhile to have this structure grown and tested.

The overall commercial prospect for a THz Raman laser is dimmed by the need for external optical pumping with high-powered lasers. The system size may be reduced by replacing the CO_2 laser pump scheme with a high-power mid-IR QCL butt-joined to the facet of the Raman laser, but this adds manufacturing complexity.

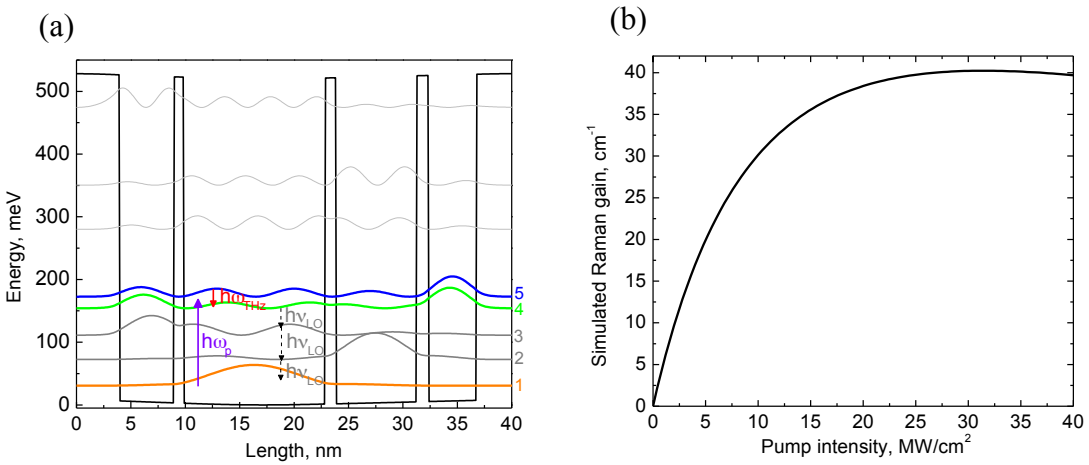

Figure 3-11, InP-based Raman Laser design: (a) Conduction band energy diagram of the proposed Raman gain section. The layer sequence from left to right is **30**/**10**/50/**9**/130/**10**/74/**11**/44/**10**/**30**, with barriers in bold and doped layers underlines. Levels 1, 4, and 5 are used to produce giant Raman nonlinearity. The energy state separation are E_{15} = 121 meV, E_{14} = 106 meV, E_{45} = 15 meV, $E_{34} = E_{23} = E_{12}$ = 35 meV. The transition dipole moments are z_{15} = 0.67 nm , z_{45} = 9.9 nm and z_{14} = 0.35 nm. The lifetime of state 4 and 5 is τ_4 = 0.2 ps and τ_4 = 0.4 ps. (b) The simulated Raman gain versus pump intensity at 300 K.

Material	**ΔE_C w/ respect to InAlAs (meV)**	**m_{eff} (m_0)**	**Υ m^{-1}**
$In_{0.53}Ga_{0.47}As$	0	0.042	11.3×10^{-19}
$In_{0.52}Al_{0.48}As$	520	0.067	3.5×10^{-19}

Table 3-3, InP IRL material parameters: $In_{0.53}Ga_{0.47}As$-$In_{0.52}Al_{0.48}As$ material parameters used in simulations.

Chapter 4: Cherenkov terahertz difference-frequency generation in quantum cascade lasers

Terahertz quantum cascade still require cryogenic cooling and the progress of improving the temperature performance has slowed considerably in the last few years. An alternative method of room-temperature terahertz generation is using difference-frequency generation in dual-wavelength quantum cascade lasers. This chapter describes previous implementations of THz difference-frequency generation (DFG) sources based on intersubband transitions in quantum well structures and explains the approach we've taken to improve the performance of sources. Specifically discussed is the modeling and implementation of a Cherenkov emission scheme for THz DFG-QCLs.

4.1 Nonlinear optics of difference-frequency generation

The optical response of a material to high-intensity electromagnetic radiation is the basis for nonlinear optics. It wasn't until the advent of lasers that nonlinear effects could be readily observed in systems. The polarization response of a material to an electromagnetic field is given by [57],

$$\vec{P}(t) = \varepsilon_0 \chi^{(1)} \vec{E}(t) + \varepsilon_0 \chi^{(2)} \vec{E}(t)^2 + \varepsilon_0 \chi^{(3)} \vec{E}(t)^3 + \ldots \quad (4.1)$$

where ε_0 is the permittivity of free-space, $\chi^{(n)}$ is the optical susceptibility and *E(t)* is the time varying electric field. The first term in Eq. 4.1 is the linear polarization response and it describes optical phenomena such as absorption in materials. In the case when a high-intensity field interacts with the material, the higher order terms in Eq. 4.1 become significant. The second-order polarization is given as

$$\vec{P}^2(t) = \varepsilon_0 \chi^{(2)} \vec{E}(t)^2 \quad (4.2)$$

A portion of this work has been published in K. Vijayraghavan, R.W. Adams, A. Vizbaras, M. Jang, C. Grasse, G. Boehm, M. C. Amann, and M.A. Belkin "Terahertz Sources Based on Čerenkov Difference-Frequency Generation in Quantum Cascade Lasers", *Appl. Phys. Lett.* 100, 251104 (2012). All authors contributed to this work.

where $\chi^{(2)}$ is referred to as the second-order susceptibility. Consider an electric field with two time-varying frequency components ω_1 and ω_2, we can write an plane-wave expression for the field as

$$E(t) = E_1 e^{-i\omega_1 t} + E_2 e^{-i\omega_2 t} + c.c. \tag{4.3}$$

where E_i is the field amplitude and c.c. is complex conjugate. Plugging Eq. 4.3 into 4.2 the polarization is given as,

$$\begin{aligned} P(t) = \; & \varepsilon_0 \chi^{(2)} \left(E_1^2 e^{-2\omega_1 t} + E_2^2 e^{-2\omega_2 t} + 2E_1 E_2 e^{-i(\omega_1 + \omega_2)t} + 2E_1^* E_2 e^{-i(\omega_2 - \omega_1)t} + c.c. \right) + \\ & 2\varepsilon_0 \chi^{(2)} \left(E_1^* E_2 + E_1 E_2^* \right) \end{aligned} \tag{4.4}$$

On the right hand side of Eq. 4.4 and in the first bracket, the first two terms represent second-harmonic generation (SHG), the third term sum-frequency-generation (SFG), and the fourth term is difference-frequency generation (DFG). The terms of Eq. 4.4 represents optical rectification (OR). The mixing of the field with the nonlinear medium produces polarization sources driven at these harmonic frequencies.

For a second-order process, we are particularly interested in using difference-frequency generation of two mid-infrared pumps to produce THz radiation at $\omega_{THz} = \omega_1 - \omega_2$. This concept has been demonstrated in nonlinear bulk optical crystals and an expression for $\chi^{(2)}$ derived using classical mechanics is given as [57]

$$\chi^{(2)}(\omega_3 = \omega_1 - \omega_2) = \frac{Ne^3}{m^2 \varepsilon_o} \frac{a}{\omega_0^6} \tag{4.5}$$

where N is the density of atoms interacting with the field, m is the mass of the atom, a is a factor relating to the nonlinear strength and ω_0 is the resonance frequency of the bulk medium. $\chi^{(2)}$ in bulk crystals is small - typically on the order of $\chi^{(2)} \sim 1$ - 40 pm/V - and

large, powerful sources are required for the pumps. Eq. 4.5 applies to the case in which the external pumps are far-off in energy compared to the natural resonance of the system. This is known as non-resonant excitation and is typically the case for THz generation in bulk materials.

In the case in which the pumps approach the resonant frequency of a system, a dramatic enhancement in nonlinearity can be achieved. Intersubband transitions in quantum wells can be exploited to engineer structures with giant nonlinearity in this manner. Resonant enhancement of susceptibility occurs when the electronic oscillations between subband states is equal or close to in energy of the pump sources. For a three level system, the resonant nonlinearity is given as

$$\chi^{(2)}(\omega_3 = \omega_1 - \omega_2) = \frac{e^3}{\mathrm{h}^2 \varepsilon_o} \frac{z_{12} z_{23} z_{31}}{(\omega_3 - \omega_{32} + i\Gamma_{32})} \times \left[\frac{N_1 - N_3}{(\omega_1 - \omega_{13} + i\Gamma_{31})} + \frac{N_1 - N_2}{(-\omega_2 + \omega_{12} + i\Gamma_{21})} \right] \tag{4.6}$$

where N_i is the electron population density in state i, and ez_{ij}, ω_{ij}, and Γ_{ij} are the dipole matrix element, frequency, and transition linewidth broadening between states i and j. Typical values for $\chi^{(2)}$ in a quantum well system ranges from 10^4 pm/V to 10^6 pm/V - more than three to four orders of magnitude larger than bulk crystals. As a result, significant nonlinear polarization can be realized for even modest pump power in the 1 – 10 MW/cm^2 range.

4.2 Previous demonstrations THz DFG sources using quantum wells and QCLs

The proof-of-principle concept of terahertz DFG using intersubband transitions in quantum wells was demonstrated by Bell labs in 1994 [71]. Devices from that work were

based on a GaAs-AlGaAs two quantum well, three energy level system and produced THz emission up to 160 K. One period of the conduction band structure along with the electron wavefunctions and the relevant energy levels is shown in Fig. 4-1. The wavefunctions were designed to have a large spatial overlap resulting in giant dipole matrix elements in the nanometer range. The energy separation between states 1-3 and 2-3 were designed to be in resonance with mid-infrared pumps provided by two external CO_2 lasers. One pump operated at $\lambda = 9.14$ μm while the other was tuned to provide tunable THz emission and the maximum THz power at the proper resonant condition. THz DFG occurs resonantly between states 1-2. The resonant nature of the DFG interaction and spatial overlap of the electron wavefunctions resulted in giant nonlinearity on the order of 10^6 pm/V – more than 5 orders of magnitude larger than bulk optical crystals and semiconductors. Subsequent improvement to quantum well design and material growth led to THz emission at room-temperature [72].

The progression towards a monolithic source involved integrating quantum cascade lasers with the nonlinear medium [29, 30, 73]. In this scheme, high-power InP-based QCLs replace the external pumps and the active region is designed for dual-wavelength mid-IR lasing at frequencies ω_1 and ω_2. The optical nonlinearity is either integrated actively [29, 30] in the band structure or passively [73] into the device structure by growing a separate active medium possessing the nonlinearity. A schematic for the passive nonlinear devices is shown in Fig. 4-1(b). The nonlinear medium is a simple two-quantum well system similar in the design concept as Refs. [71, 72] and grown on top of the QCL active region providing the mid-IR pump lasing. Given that the

nonlinear medium is designed to be in resonance with the mid-IR pumps, large absorption loss of the pumps prevents the distribution of the nonlinear layer along the entire waveguide length. Therefore, the nonlinearity is concentrated near the output facet of the laser as shown in Fig.4-1(b). This type of device produced only 100 nW of power at ω = 4.1 THz and operated at maximum temperature of 210 K [73].

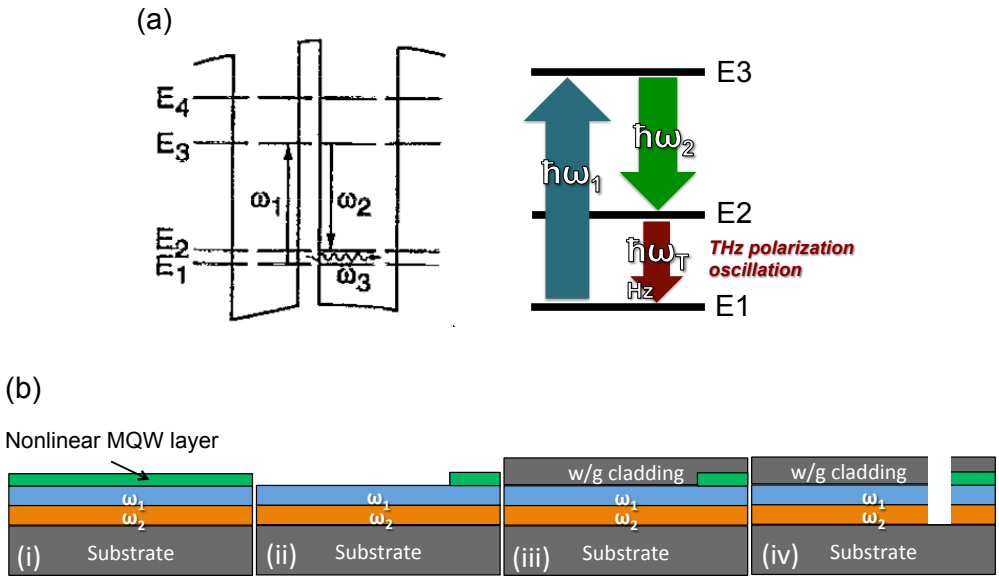

Fig 4-1, THz DFG sources with passive nonlinearity: (a) The quantum well design for the first report on THz DFG using intersubband transitions. CO_2 lasers externally pump the structure at ω_1 and ω_2. THz DFG is generated between states 1-2 and provides emission at $\omega_3 = \omega_1 - \omega_2$. (b) Monolithic configuration that replaces the external CO_2 pumps with a dual-wavelength mid-IR QCL. The nonlinear quantum well medium is grown on top the QCL active region. (i) The nonlinear medium (green) is grown on top of the active region (blue and orange) and then is (ii) selectively etched to concentrate it near the device output facet. (iii) The upper cladding (grey) is regrown to provide adequate confinement for the mid-IR pumps and (iv) the nonlinear section is then electrically isolated by etching a trench.

Active devices have optical nonlinearity integrated in the mid-infrared gain medium [29, 30, 74-81]. In this scheme, the mid-infrared pump absorption loss is

negligible because the laser gain regenerates the mid-IR pumps as THz DFG is produced along the length of the waveguide. The first devices demonstrating this concept was reported by Belkin et al. in 2007 and operated at low-temperatures [29]. The same author reported room-temperature devices in 2008 and Fig. 4-2 shows the device schematic from that work [30]. Similar to the monolithic passive devices, dual active region cores were designed to provide mid-IR emission at λ_1 and λ_2. Optical nonlinearity is incorporated in the active region stack and the energy levels that partake in the DFG process are colored. The upper laser state is denoted by state 1 and the lower states by 2 and 3, respectively. Lasing at frequency ω_1 takes place between energy states 1-3, states 1-2 is in resonance with ω_2 (provided by the two-phonon resonance active region not shown), and THz DFG takes place resonantly between lower laser states 2-3 and produces emission at THz frequency $\omega_{THz} = \omega_1 - \omega_2$. Experimentally, these sources provided a peak power of 300nW at 4THz.

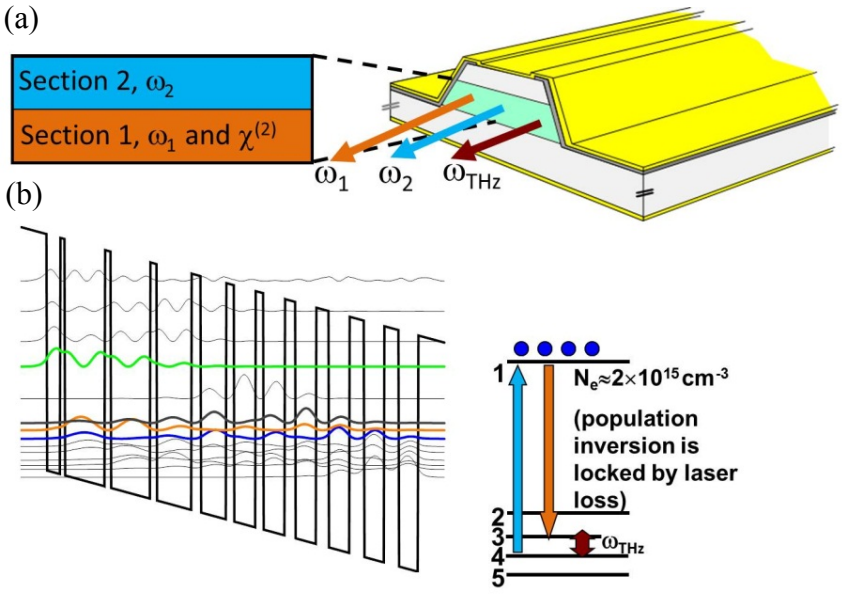

(Figure 4-2 continues on next page)

Fig 4-2, THz DFG sources with active nonlinearity: (a) Device geometry and waveguide design with dual color active region (b) Active region with integrated nonlinearity.

The unique aspect of this design is that the nonlinearity is incorporated in the active gain medium of the laser. Pump absorption no longer is an issue. However the density of carriers that partake in the nonlinear process is clamped by the laser "gain = loss" condition. As a result, the strength of $\chi^{(2)}$ is smaller by two orders of magnitude. An important figure-of-merit for THz DFG QCLs is the mid-infrared-to-THz *conversion efficiency*, which is defined as the ratio of the generated THz power to the product of the mid-infrared pump powers [29]. In addition to the bandstructure design, the conversion efficiency is heavily influenced by the waveguide design. The waveguide for the active device discussed above is based on a collinear modal phase matching scheme that provides confinement for both mid-IR and THz modes within the laser active region and operates close to the ideal phase-matching condition. A side-view of this waveguide configuration is shown in Fig. 4-3(a). The THz mode propagates along the nonlinear core until it reaches the mid-IR laser facet and outcouples to free-space. An expression for the conversion efficiency in active devices is given as [29]

$$\eta = \frac{W(\omega_3 = \omega_1 - \omega_2)}{W(\omega_1)W(\omega_2)} = \frac{\omega_3^2}{8\varepsilon_0 c^3 n_{\omega_1} n_{\omega_2} n_{\omega_3}} \left|\chi^{(2)}\right|^2 \frac{l_{eff}^2}{S_{eff}} \tag{4.1}$$

where $W(\omega_i)$ and $n(\omega_i)$ are the power and refractive index of the beam at frequency ω_i. The S_{eff} term is the effective area of interaction of the mid-IR and THz beams within the nonlinear layer, and is given by [29]

$$S_{eff} = \left|\chi^{(2)}\right|^2 \frac{\int[H_{\omega 3}(x,z)]^2 dxdz \int[H_{\omega 1}(x,z)]^2 dxdz \int[H_{\omega 2}(x,z)]^2 dxdz}{\left|\int H_{\omega 3}(x,z) H_{\omega 1}(x,z) H_{\omega 2}(x,z) \chi^{(2)}(x,z) dxdz\right|^2} \quad (4.2)$$

where $H_{\omega i}(x,z)$ is the magnetic field amplitude for the beam at frequency ω_i, propagating along the waveguide. Given that the mid-IR and THz mode propagate in the same waveguide, the overlap between these modes and the optical nonlinearity is excellent. The term l_{eff} is the effective length of the nonlinear interaction and is dependent upon THz optical loss and phase matching considerations in the nonlinear medium, and is given as

$$l_{coh}^{\ 2} = \frac{1}{\left(k_1 - k_2 - k_{THz}\right)^2 + \left(\alpha_{THz}/2\right)^2} \quad (4.3)$$

where $\Delta k = k_1 - k_2 - k_{THz}$ is the wavevector mismatch between the mid-IR and THz modes and α_{THz} is the THz waveguide loss. The waveguide can be designed with $\Delta k \approx 0$ by varying the thicknesses and doping of the cladding and active region. However, the THz loss in this configuration is significantly large and limits the coherence length to ~100μm. This is because the mid-IR cladding layers and active regions need to have a sufficiently high doping density ($n \approx 5 \times 10^{16}$ cm^{-3} is used in Ref. [29, 30, 74]) to provide high-power mid-IR output, high optical nonlinearity and sufficient conductivity to facilitate current transport through the device. A Drude-Lorentz model was used to compute the THz optical loss (α) in the InP cladding layers moderately doped to $n = 1 \times 10^{16}$ cm^{-3} and 5×10^{16} cm^{-3} and the results are plotted in Fig. 4-3(b) as a function of THz frequency. The implication of high loss is the following; THz DFG occurs along the

whole waveguide length in these devices. However, high THz losses implies that only the THz radiation generated within ~1/α from the waveguide exit facet can be out-coupled in these devices. Detailed waveguide calculations for 4-5 THz sources give a value for 1/α of ~40 μm [30] and ~67 μm [74]. As follows from the trend in Fig. 4-3(b), 1/α is expected to decrease to below 15 μm at 1 THz. These numbers imply that, for a 3-mm-long THz DFG QCL, over 97% of THz light generated at 4-5 THz and over 99.5% of THz light generated around 1 THz is absorbed in the QCL waveguide.

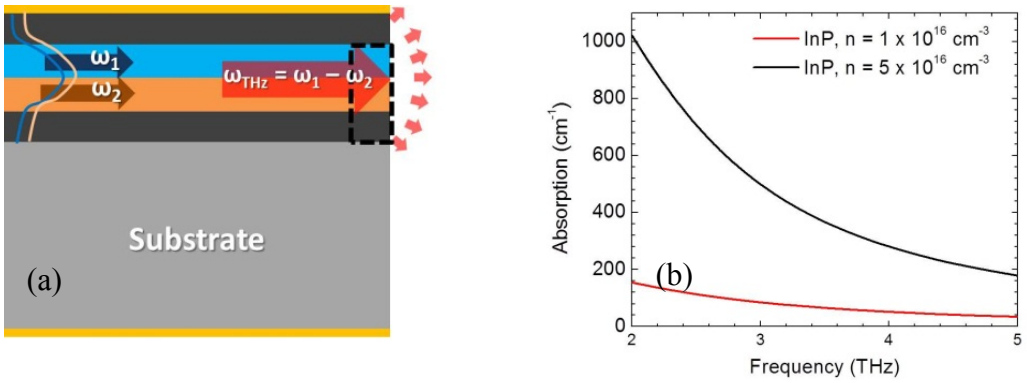

Fig 4-3, Collinear waveguide and THz absorption loss in cladding: (a) Side-view profile of the waveguide showing the active region (blue and orange) surrounded by the cladding layers (dark grey). THz DFG is produced along the entire length of the nonlinear core and exits out of the mid-IR laser facet. Due to large waveguide absorption, only the DFG generated close to the output facet (black box, dashed line) will outcouple. (b) Simulated absorption coefficient for typical doping levels in the cladding.

The THz mode experiences large free-carrier absorption in a modal-phase matching scheme and devices have low conversion efficiencies in the 3.5 μW/W^2 - 10μW/W^2 range at 4 THz [30, 74] . To improve THz power, devices with larger conversion efficiencies

are required. The very first report on THz DFG-QCLs recognized this issue and recommended a vertical-emitting scheme that extracts the THz mode along the length of the waveguide. In addition to improved THz outcoupling, the broad area of surface emission would improve the THz far-field profile. Soon after, a surface-emission scheme using a second-order diffraction grating for THz outcoupling was implemented for DFG-QCLs [82]. However the performance of these devices was poor and they produced 1μW THz power with a conversion efficiency of 0.4 μW/W^2 at 80K, and less than 70 nW THz power at room-temperature. The reason for the poor-performance is that surface-gratings also suffer from short coherence lengths. For THz wavelengths, the grating period is approximately 20 μm. With an effective coherence length of 40μm - 60 μm, nearly all of the THz emission would need to outcouple within the span of 3 periods.

4.3 Intracavity Cherenkov difference-frequency generation

In this work, we propose a new waveguide configuration such that the THz radiation is emitted through the substrate of the device (see Fig. 4-4a). This occurs through Cherenkov phase matching [83-85]. In such a configuration, THz radiation can be extracted from the entire length of the thin nonlinear core, which then propagates through the substrate at an angle. Proof-of-principle devices demonstrate broadband, directional output over the 1.2 – 4.5 THz range with a maximum 70 μW/W^2 conversion efficiency.

Cherenkov emission in nonlinear optics occurs when the phase-velocity of the nonlinear polarization wave in a thin slab of nonlinear optical material is faster than the phase-velocity of the generated radiation in the medium that surrounds the slab [13]. In

this case, the generated radiation is emitted at the Cherenkov angle θ_C from the slab as shown in Fig. 4-4(a). In the case of DFG-QCLs we can write an expression for the nonlinear polarization wave at $\omega_{THz}=\omega_1-\omega_2$ in the slab waveguide approximation as [14]:

$$P_z^{(2)}(x,z) = \varepsilon_0 \chi_{zzz}^{(2)}(z) E_z^{\omega_1}(z) E_z^{\omega_2}(z) e^{i(\omega_{THz}t-(\beta_1-\beta_2)x)}, \tag{4.4}$$

where the z-direction is normal to the QCL layers and the x-direction is along the waveguide, see Fig. 4-4a, β_1 and β_2 are the propagation constants for mid-IR pump modes, $E_z^{\omega_1}(z)$and $E_z^{\omega_2}(z)$ are z-components of E-field of the mid-IR pump modes, and $\chi_{zzz}^{(2)}(z)$ is the giant intersubband optical nonlinearity for DFG in the QCL active region. In terms of propagation constants, this means that the propagation constant of the nonlinear polarization wave (k_{nl}) is smaller compared to that of the THz radiation (k_{THz}) in the substrate. In this case, generated radiation is emitted at the Cherenkov angle

$$\theta_C = \cos^{-1}\left(k_{nl}/k_{THz}\right) \tag{4.5}$$

relative to the direction of k_{nl}, as shown schematically in Fig. 4-4(a). Experimentally, Cherenkov nonlinear emission was first observed for second harmonic generation (SHG) [84] and later for DFG [85]. Since then, it has been observed in a wide range of devices and processes, including SHG in GaAs/AlGaAs mid-IR QCLs [86].

In the case of DFG in QCLs, the propagation constant of the nonlinear polarization wave in the active region is given as $|\beta_{\omega 1}-\beta_{\omega 2}|$ [14], where $\beta_{\omega i}=n_{eff}(\omega_i)\omega_i/c$ with $n_{eff}(\omega_i)$ being the effective refractive index of the mid-IR pump mode at frequency ω_i (i=1,2). Since the two mid-IR pump frequencies are close, $\omega_1 \approx \omega_2$, one can write [57]

$$\left|\beta_1 - \beta_2\right| \approx \frac{n_g \omega_{THz}}{c} \tag{4.6}$$

where $n_g = n_{eff}(\omega_1) + \omega_1 \left.\frac{\partial n_{eff}}{\partial \omega}\right|_{\omega=\omega_1}$ is the group effective refractive index at ω_1 and $\omega_{THz}=\omega_1-\omega_2$ is the THz difference-frequency. In order to produce Cherenkov DFG emission into the substrate, the substrate refractive index at ω_{THz} must be larger than n_g. We have realized that this condition is satisfied throughout the 1-5 THz spectral range for InP/GaInAs/AlInAs QCLs grown on semi-insulating InP. As a result, efficient broadband THz QCL sources based on Cherenkov DFG can easily be implemented.

The schematic of proof-of-principle devices is shown in Fig. 4-4(b). The laser structure is virtually identical to that of the first room-temperature THz DFG-QCL sources reported in Ref [30], except that here we used a semi-insulating InP substrate and a lateral current injection scheme [40, 87]. The refractive index profile for mid-IR and THz frequencies in our laser is shown in Fig. 4-4(c). In mid-IR, the refractive index of the substrate is low and allows for good mode confinement. In the 1-5 THz range, due to the *Reststrahlenband* at 8-10 THz, the refractive index of semi-insulating InP is large and the Cherenkov condition is fulfilled. The waveguide calculations for our devices gives $n_g \approx 3.37$ in mid-IR. Given the refractive index of undoped InP of 3.6 (virtually independent of frequency in 1-5 THz range) [88], we obtain a Cherenkov angle $\theta_C \approx 21^o$ for DFG in the whole 1-5 THz range. Once in the substrate, THz radiation propagates towards the facet. Since undoped InP is virtually lossless over 1-5 THz, the Cherenkov emission scheme allows for efficient extraction of THz radiation along the whole length of the QCL

waveguide. To avoid total internal reflection of the THz Cherenkov wave at the front facet, the substrate has to be polished at a 20°- 30° angle as shown in Fig. 4-4(a).

Devices were grown by molecular beam epitaxy (MBE) on 350-µm-thick semi-insulating InP substrates. $In_{0.53}Ga_{0.47}As$-$In_{0.52}Al_{0.48}As$ heterostructures lattice-matched to InP was used. The growth started with a 3-µm-thick current extraction layer made of InP doped to n = 1 x 10^{17} cm^{-3}, followed by 33 repetitions of the 'bound-to-continuum' active region with integrated optical nonlinearity and 27 repetitions of the 'double-phonon resonance' active region, separated by a 100-nm-thick InGaAs spacer region doped to n = 5 x 10^{16} cm^{-3}. To be able to see the advantage of the Cherenkov DFG scheme over a modal phase matching scheme [6, 7], the bandstructure design of the two active region sections in our devices was chosen to be identical to that used in Refs. [6, 7]. The top cladding layer consists of 3.5-µm-thick InP n-doped to 5×10^{16} cm^{-3} followed by a 200-nm-thick InP n-doped to 2×10^{18} cm^{-3}.

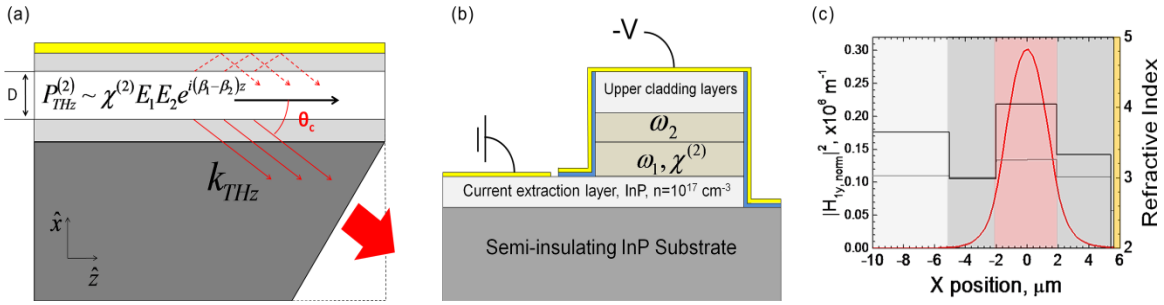

(Figure 4-4 continues on next page)

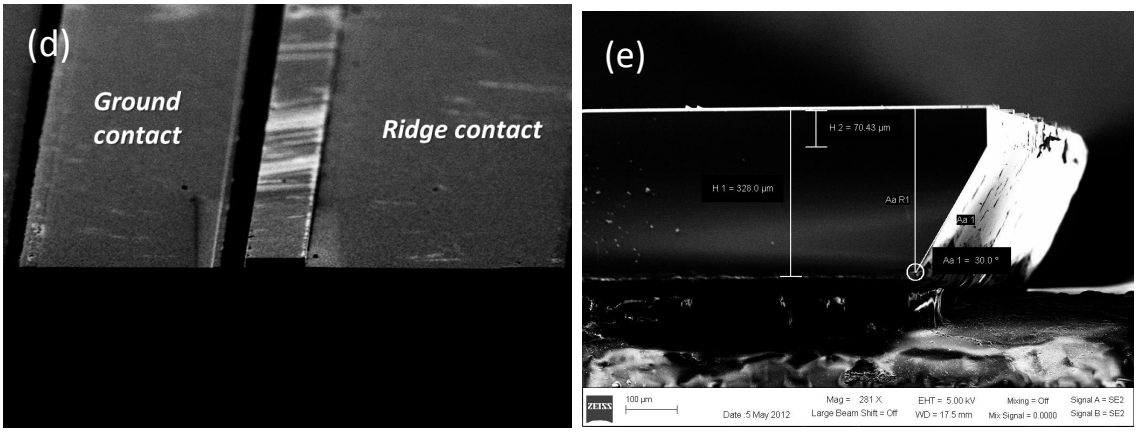

Figure 4-4, Cherenkov waveguide, device configuration and mode profile (started on previous page). (a) Schematic of Cherenkov THz DFG emission in a QCL. Waveguide cladding layers are shown in light gray, top gold contact layer is shown in yellow. Cherenkov THz radiation emitted into the substrate is shown with arrows. It may also be emitted towards the top contact layer (show with dashed arrows) and reflected to the substrate. (b) Facet-view schematic. Gold contact layers are shown as yellow, insulating SiN layers are shown as blue, InP layers are shown as grey and labeled, active region with two sections designed to emit mid-IR pumps at ω_1 and ω_2 is shown in brown. (c) Vertical refractive index profile in our devices for mid-IR (λ=9µm, grey line, right axis) and 4.5 THz (black line, right axis) light. Position x=0 corresponds to the middle of the active region, see (b). Also shown is the computed mid-IR waveguide mode. Colored regions indicate waveguide cladding layers (dark grey), active region (red), and substrate (light grey). (d) SEM cross-section of processed device. (e) SEM image of the polished substrate.

The material was processed into 35-µm-wide ridge waveguides via dry etching. The sidewalls of the ridges were insulated with a 600-nm-thick layer of SiN, followed by a Ti/Pt/Au (30nm/60nm/1000nm) contact layer deposition. Figure 4-4(b) shows the cross-section schematic of the processed ridge laser. The wafer was then cleaved into laser bars with 1-mm-long devices. A high reflectivity coating of Al_2O_3/Ti/Au (100 nm/5 nm/50 nm) was then evaporated onto the back facets of devices. The 350-µm-thick InP

substrate associated with the exit facet of the device was then mechanically polished to the desired angle with a combination of SiC lapping compound and Al_2O_3 lapping film. Special care was taken to ensure that the laser waveguide facets are unaffected by polishing. Devices were then indium soldered onto copper holders and wire bonded. A high resistivity silicon microlens was attached to the THz exit facet with Epoxy *adhesive* in order to improve outcoupling and collection efficiency of the THz beam.

Spectral emission of both the mid-infrared and terahertz beams was measured using a Fourier-transform infrared spectrometer. A helium-cooled silicon bolometer and deuterated L-alanine doped triglycine sulfate (DLaTGS) detector were used for the THz and mid-infrared spectral measurements, respectively. The power output of these devices was measured using a calibrated thermopile detector for the mid-infrared beams and a calibrated helium-cooled silicon bolometer for the THz beams. We corrected the measured power for loss associated with parabolic mirror system collection. The power collection efficiency for the output beams in our optical setup is approximately 70% for the mid-infrared emission, and approximately 50% for the THz emission. Appropriate optical filters were used to differentiate between the mid-infrared pump beams, and to separate mid-infrared and THz emission.

The results are shown in Fig. 4-5 for a 1-mm-long laser with the substrate polished at 20^o. The mid-IR emission was observed at two groups of frequencies centered around 1020 cm^{-1} (λ_1=9.8 μm) and 900 cm^{-1} (λ_2=11.1 μm) as shown in the inset of Fig. 4-5. Experimentally, the mid-IR pump wavelengths are slightly longer compared to design wavelengths of 8.9 μm and 10.5 μm. Since QCLs with an identical active region design

operated as designed earlier [30, 74], the difference in the current devices is attributed to growth calibration. Power measurements were performed using bandpass filters to separate two groups of frequencies. The results are shown in Fig. 4-5 along with the current-voltage characteristic of the laser. We emphasize that the mid-IR pumps are unaffected by substrate polishing since the ridge facet and mid-IR waveguide structure remains intact during polishing. The improvement in the THz power output is thus entirely due to improved outcoupling of THz radiation.

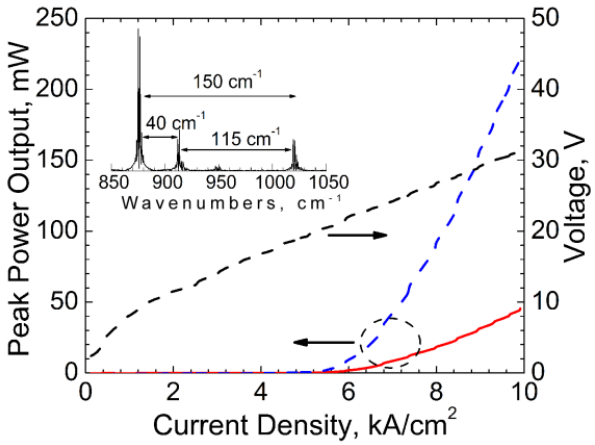

Figure 4-5, Mid-IR Performance: Light output-current density (bottom and left axes) and current density-voltage (bottom and right axes) characteristics of a of a 1-mm-long laser with high-reflection back facet coating. Dashed blue line is the emission centered around 900cm^{-1} and solid red line is emission at 1020 cm^{-1}. Voltage shown as dotted black line. The laser was operated at room temperature with 100 ns pulses at 100 kHz repetition frequency. (inset) Emission spectrum.

The room-temperature THz emission spectrum of the same device is displayed in Fig. 4-6(a). To maximize THz collection efficiency, a high-resistivity silicon hyperhemisphere lens was affixed to the polished substrate facet for spectral measurements. Optical filters were used to block mid-IR output. The spectrum shows

three THz peaks in perfect agreement with the mid-IR pump frequency spacing shown in Fig. 2. Because of the large emitter area (whole laser waveguide), the Cherenkov THz wave is expected to be well-collimated in the direction normal to the waveguide layers. Figure 4-6(b) shows far-field THz emission profiles of three devices: 1-mm-long lasers with the substrate output facet as cleaved (vertical), polished at 20^o, and polished at 30^o. The far field pattern of the unpolished sample is very broad and weak. In these lasers the Cherenkov wave experiences total internal reflection and only optical nonlinearity near the exit facet contributes to THz output, similar to devices reported in Refs. [30, 74]. Contrastingly, the samples polished to 20° and 30° had highly directional emission and strong output. For the case of 20° polishing, we see a sharp emission peak approximately 22.5° below normal incidence. In the case of 30° polishing, the beam emits almost normal to the exit facet of the ridge, with a peak 7° above normal incidence. In both cases, taking into account the refraction that occurs at the air-semiconductor interface, this corresponds to an internal emission angle at approximately 20.5° which is in good agreement with the theoretical value of $\theta_C \approx 21^o$. Difference in the widths of the emission profiles in the case of 20^o and 30^o polishing in Fig. 4-6(b) is most likely due to curvature or other artifacts of the polished facet introduced during manual polishing.

Figure 4-6(a) displays the THz power output for two samples: one with an unpolished exit facet and the other one with exit facet polished to 20°. High resistivity silicon hyperhemisphere lenses were affixed to the THz exit facet for both devices. The unpolished sample produced peak THz power output of only 0.07 μW at 300 K, which corresponds to a mid-IR to terahertz conversion efficiency of ≈7 $\mu W/W^2$. The 20°

polished sample produced 0.5 μW of THz output power at 300 K, which corresponds to a conversion efficiency of ≈ 45 μW/W^2, which is approximately a factor of 10 above the conversion efficiencies in multi-mode THz DFG QCLs reported earlier [30, 74]. More detailed analysis of power distribution in mid-IR pumps and THz output may be performed by integrating areas below peaks in mid-IR (Fig. 4-5(a)) and THz (Fig. 4-6(a)) spectra. This analysis yields conversion efficiencies of 70 μW/W^2, 40 μW/W^2, and 8.4 μW/W^2 for THz emission lines at 3.3 THz, 4.5 THz and 1.2 THz, respectively.

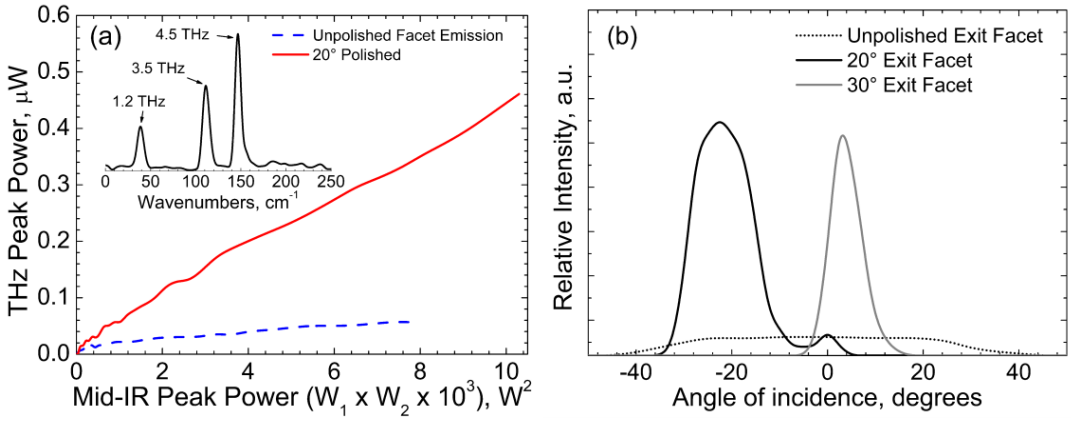

Figure 4-6, Terahertz performance of Cherenkov devices: (a) Room-temperature terahertz peak power output vs the product of mid-IR pump powers for a device with the substrate polished at 20^o (solid red line) and a device with unpolished substrate (dashed blue line). (inset) Room-temperature terahertz emission spectrum of the device analyzed in Fig. 2. Terahertz emission peak positions correspond to differences between mid-IR pump frequencies. Data was taken in step scan mode; the laser was operated at room temperature with peak current density of 9.6 kA/cm^2. (b) Far-field emission profiles of devices with substrate polished at 20^o (solid black line), substrate polished at 30^o (dashed grey line), and with unpolished substrate (dotted black line). Lasers were operated at 80K with current density of 9.6 kA/cm^2.

To evaluate the mid-IR-to-THz conversion efficiency in our devices theoretically, we treat Cherenkov emission as a leaky THz waveguide mode with the propagation

constant along the waveguide direction fixed at $\beta_{\omega 1}$-$\beta_{\omega 2}$. Similarly to Ref. [89], we find an *analytical* solution of the Cherenkov wave in a slab waveguide. A plane wave transfer matrix method programmed in Mathematica was used to simulate the intensity of the Cherenkov wave in the device substrate. The waveguide structure of our lasers and the coordinate system used in this analysis is presented in Fig. 4-7(a). Mid-IR pumps are assumed to be propagating along z-axis in positive direction. For calculations presented below, we obtain the values of the refractive indices in our QCL by combining the table values of the refractive indices of undoped semiconductor compounds with the Drude model with the relaxation time constant $\tau=10^{-13}$ sec to account for the free-carrier contribution. The refractive indices of undoped $Al_{0.48}In_{0.52}As$ and $In_{0.53}Ga_{0.47}As$ compounds in the waveguide core are calculated using the linear interpolation between the data for the binary compounds. We note that this approach is known to work well in the mid-IR; however, that it may not be very accurate for the wavelength of 60-100μm, because of the proximity of the *Reststrahlenband* and the strong dependence of the optical phonon energies on the material composition. Experimentally, we measured mid-IR and THz power emitted from a QCL. These powers are related to the powers inside of a QCL through facet power transmission coefficients *T*. Assuming $T_1 = T_2 = T_{THz} = 0.7$ for both mid-IR pumps and THz Cherenkov wave, respectively, we obtain for the theoretical values of 'experimental' conversion efficiency:

$$\eta_{ext} \approx \eta \frac{T_1 T_2}{T_{THz}} = \begin{cases} 1.2\,mW/W^2 @ 4.5THz \\ 0.13\,mW/W^2 @ 3.5THz \\ 0.02\,mW/W^2 @ 1.2THz \end{cases} \tag{4.7}$$

Experimentally-measured efficiencies are similar in magnitude for DFG at 3.5 and 1.2 THz but over 2 orders of magnitude smaller for DFG at 4.5 THz.

The discrepancy with experimental results may be due to a number of factors. Firstly, we note that theoretical results are very sensitive to the values of refractive indices of different waveguide layers in THz, and these are not known precisely. In particular, the refractive index of the $Al_{0.48}In_{0.52}As/In_{0.53}Ga_{0.47}As$ active region is calculated using the linear interpolation between the data for the binary compounds. This approach is known to work well in mid-IR, but it is likely to produce significant errors in THz, especially for 4.5 THz DFG because of the proximity of the *Reststrahlenband* and the strong dependence of the optical phonon energies on the material composition. The value of optical nonlinearity in the actual devices may be different, compared to a theoretical estimate of $1.5x10^4$ pm/V[7] used for our calculations. It is also likely to be different for THz DFG at different frequencies. Additionally, mid-IR pumps are known to be partly operating in higher-order waveguide modes, which dramatically reduces their interaction in the nonlinear section as described in Ref. [90]. Finally, THz modes are not plane waves as assumed in this slab-waveguide analysis.

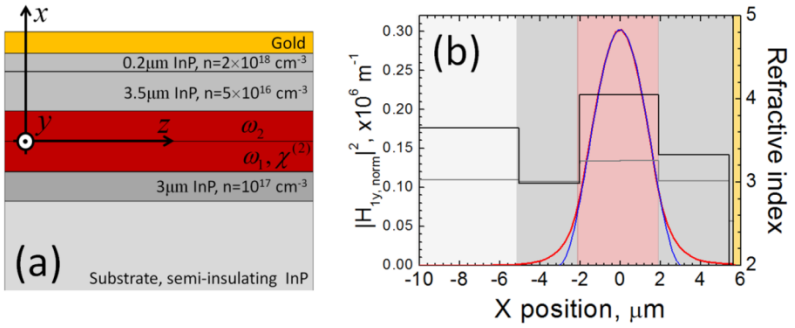

(Figure 4-7 continues on next page)

Figure 4-7, Device layers and mid-IR mode profile (started on previous page): Assumed coordinate system and details of the waveguide structure in our devices. (a) Device layers and coordinate system assumed in calculations. (b) Refractive index profile (bottom and right axes) in our devices for 4.5 THz (black line) and λ_1=9μm pump (grey line). Also shown are calculated TM_0 mode at λ_1=9μm, normalized so that $\int_{-\infty}^{+\infty}\left|H_{1y,norm}(x)\right|^2 dx[m]=1$ (red line, bottom and left axes) and the analytical solution in Eq. S2 for comparison. Colored regions indicate waveguide cladding layers (dark grey), active region (red), and substrate (light grey).

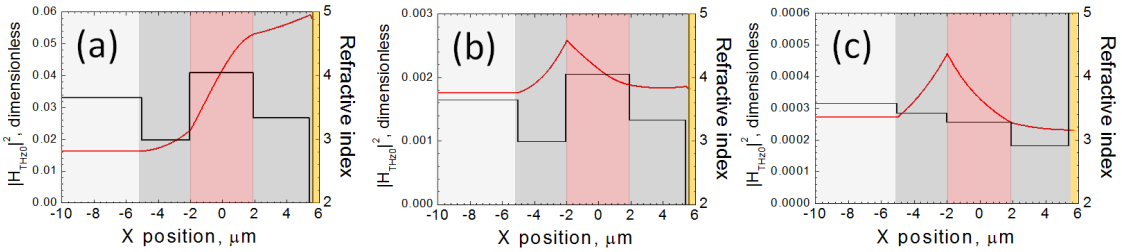

Figure 4-8, Cherenkov mode profiles: Calculated THz Cherenkov mode $|H_{THz0}|^2$ for THz DFG (red line, bottom and left axes) and waveguide refractive index profiles (black line, bottom and right axes) at (a) 4.5 THz, (b) 3.5 THz, and (c) 1.2 THz. Colored regions indicate waveguide cladding layers (dark grey), active region (red), and substrate (light grey).

Chapter 5: Cherenkov THz DFG-QCL sources for broadband tuning

In the previous chapter, it was shown that proof-of-principle Cherenkov DFG-QCL sources produce well collimated, directional broadband emission and have a larger conversion-efficiency with respect to modal-phase matched sources. But to evaluate the performance of Cherenkov devices, we had to implement the same active region and cladding structure used for modal-phase matched designs.

In this chapter, we present sources that have been comprehensively optimized for improved THz generation and Cherenkov outcoupling. We discuss a band structure in which optical nonlinearity is specifically integrated in *both* active regions sub-stacks, thereby effectively doubling the thickness of the nonlinear core. We present a more rigorous calculation for $\chi^{(2)}$ that is more accurate compared to previous reports on THz DFG-QCLs. We also use the mathematical model derived for the Cherenkov wave in the previous section and comprehensively optimize the layer thicknesses and doping to maximize THz transmission into the substrate and operate closer to the optimal phase matching condition. Finally, we use a first-order dual period DFB grating to demonstrate narrow-linewidth THz sources and demonstrate broadly tunable sources.

5.1 Dual bound-to-continuum active region with $\chi^{(2)}$

An active region with a broadband mid-infrared gain spectrum was designed to achieve large THz tuning. The waveguide core was made up of two stacks of QCL stages designed for emission at $\lambda_1 = 8.2$ μm and $\lambda_2 = 9.2$ μm. Giant optical nonlinearity for the DFG process is integrated in the QCL bandstructure by reducing the thickness of the extraction barrier and producing significant anti-crossing between the lower laser level

A portion of this work has been published in K. Vijayraghavan, Y. Jiang, M. Jang, A. Jiang, K. Choutagunta, A. Vizbaras, F. Demmerle, G. Boehm, M. C. Amann, and M. A. Belkin, "Broadly tunable terahertz generation in mid-infrared quantum cascade lasers", *Nature Comm.* 4, 2021 (2013). All authors contributed to this work.

state and the injection states. As a result, the laser design effectively becomes a bound-to-continuum QCL design [35]. The calculated bandstructure and squared-moduli of the electron wave functions for one period of these structures are depicted in Fig. 5-1. The design of both sections is chosen to have large optical nonlinearity $\chi^{(2)}$ for DFG between the mid-IR pumps.

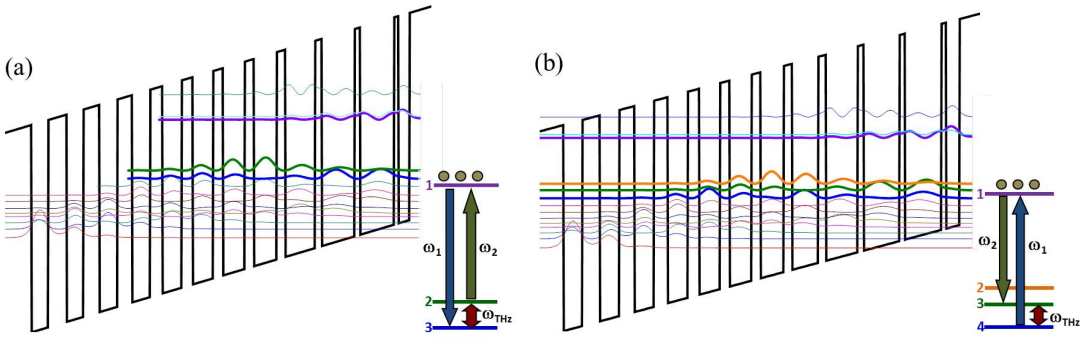

Figure 5-1, Active region bandstructure for QC111: (a) Conduction band diagram for one period of active region Stack A biased at 48kV/cm and producing radiation around 8.20µm. Schematic description of resonant DFG process in Stack A is shown in the bottom left. Transition dipole moments z_{12} = 2.20 nm, z_{13} = 2.20 nm, z_{23} = 8.00 nm, E_{12}= 134.8 meV, and E_{13}= 154.1 meV are calculated for this structure. Lasing at λ_1 occurs in near-resonance to a transition between states 1 and 3. Transition between states 1 and 2 is in near-resonance with the pump at λ_2. (b) Conduction band diagram for one period of active region Stack B biased at 40 kV/cm and producing radiation around 9.20µm. Schematic description of resonant DFG process in Stack A is shown in the bottom left Transition dipole moments z_{12} = 2.00 nm, z_{13} = 2.37 nm, z_{14} = 0.60 nm, z_{34} = 9.80 nm, E_{12}= 117.0 meV, E_{13}= 134.4 meV and E_{14}= 153.6 meV are calculated for this structure.

Our method for calculating $\chi^{(2)}$ for the active regions presented in Fig. 5-1 follows a similar approach described in Ref. [29]. We use the fully-resonant quantum-mechanical expression for $\chi^{(2)}$ given as [57]:

$$\chi^{(2)}(\omega_{DFG}=\omega_p-\omega_q,\omega_p,-\omega_q)=\Delta N\frac{e^3}{\varepsilon_o\hbar^2}\sum_{lmn}\rho_{ll}^{(0)}\left\{\begin{array}{l}\dfrac{z_{ln}z_{nm}z_{ml}}{\left[\left(\omega_{nl}-\omega_{DFG}\right)-i\Gamma_{nl}\right]\left[\left(\omega_{ml}-\omega_p\right)-i\Gamma_{ml}\right]}\\+\dfrac{z_{ln}z_{nm}z_{ml}}{\left[\left(\omega_{nl}-\omega_{DFG}\right)-i\Gamma_{nl}\right]\left[\left(\omega_{ml}+\omega_q\right)-i\Gamma_{ml}\right]}\\+\dfrac{z_{ln}z_{nm}z_{ml}}{\left[\left(\omega_{mn}-\omega_{DFG}\right)-i\Gamma_{nl}\right]\left[\left(\omega_{nl}+\omega_p\right)+i\Gamma_{nl}\right]}\\+\dfrac{z_{ln}z_{nm}z_{ml}}{\left[\left(\omega_{mn}-\omega_{DFG}\right)-i\Gamma_{nl}\right]\left[\left(\omega_{nl}-\omega_q\right)+i\Gamma_{nl}\right]}\\+\dfrac{z_{ln}z_{nm}z_{ml}}{\left[\left(\omega_{nm}+\omega_{DFG}\right)+i\Gamma_{nl}\right]\left[\left(\omega_{ml}-\omega_p\right)-i\Gamma_{ml}\right]}\\+\dfrac{z_{ln}z_{nm}z_{ml}}{\left[\left(\omega_{nm}+\omega_{DFG}\right)+i\Gamma_{nl}\right]\left[\left(\omega_{ml}+\omega_q\right)-i\Gamma_{ml}\right]}\\+\dfrac{z_{ln}z_{nm}z_{ml}}{\left[\left(\omega_{ml}+\omega_{DFG}\right)+i\Gamma_{nl}\right]\left[\left(\omega_{nl}+\omega_p\right)+i\Gamma_{nl}\right]}\\+\dfrac{z_{ln}z_{nm}z_{ml}}{\left[\left(\omega_{ml}+\omega_{DFG}\right)+i\Gamma_{nl}\right]\left[\left(\omega_{nl}-\omega_q\right)+i\Gamma_{nl}\right]}\end{array}\right\} \quad (5.1)$$

where the indices l,m,n correspond to the energy levels that take part in DFG, ΔN is the population inversion density and ez_{ij}, ω_{ij} and Γ_{ij} are the dipole matrix element, frequency, and broadening of the transition between states i and j. Applying this equation to our structures (see Fig. 5-1), we set l=1, and permute m and n over all combinations of the lower state energy levels. This results in 16 terms and 32 terms for the active regions presented in Fig. 5-1(a,b), respectively, and is too long to write here. Values for energy levels and dipole matrix elements were found using a self-consistent Schrödinger-Poisson solver and given in the Fig. 5-1 caption. Values for the transition linewidth between states were chosen by comparing data from different literature sources [65, 66]; here we used a

full-width of half-max of $\Gamma = 12.5$ meV and $\Gamma = 4$ meV for the mid-infrared and THz transitions, respectively.

To evaluate $\chi^{(2)}$, we need to calculate the population difference ΔN between DFG states. In our structures, state 1 coincides with the upper laser level and all other DFG states coincide with the lower laser levels (see Fig. 5-1(a,b)). We can therefore approximate ΔN as being equal to the upper state population and assume the same population density in each active region. This can be found by applying the "gain = loss" condition for a laser given as:

$$\frac{g_{1,\omega}+g_{2,\omega}}{2} = \frac{\alpha_m+\alpha_w}{\Gamma} \tag{5.2}$$

where Γ, $g_{i\omega}$, α_w, α_m, and g_{max} is the mid-infrared modal overlap with the active region core (with includes both active region stacks) at frequency ω, the gain in active region i at frequency ω, waveguide loss, mirror loss, and maximum gain at which clamping occurs, respectively. We simulate our structure using COMSOL and find that $\Gamma = 0.84$, $\alpha_w \approx 7$ cm^{-1} and $\alpha_m \approx 6$ cm^{-1} for a 2mm-long device with uncoated facets. This results in $g_{max} \approx 30$ cm^{-1}.

Next, we calculate the gain spectrum for each active region stack using the QCL gain expression given as:

$$g\left(\omega_i\right) = \frac{\omega_i}{cn_{eff}\left(\omega_i\right)}\frac{\Delta N}{\varepsilon_0 \hbar}\mathrm{Im}\left(\sum_n \frac{\left|e\cdot z_{1n}\right|^2}{\left(\omega_i-\omega_{1n}\right)-i\cdot\Gamma_{1n}}\right) \tag{5.3}$$

where n_{eff} is the effective modal index at frequency ω_i. The simulated gain spectrum for both active regions combined and the measured electroluminescence (EL) is presented in Supplementary Fig. 5-2(a). The EL spectrum is red-shifted by 50 cm^{-1} compared to the simulation. We attribute this shift to uncertainty in the growth parameters (i.e. layer thicknesses, doping, etc.). We can reconcile the differences in the measured/simulated spectrum by shifting the simulated gain spectrum to overlay with the EL spectrum as shown in Supplementary Fig. 5-2(b). We note that we still assume the same values for the transition dipole moments simulated in the 'pre-shifted' structure.

For a 4 THz source, DFBs can be used to select the mid-IR pumps at λ_1 = 1120cm^{-1} and λ_2 = 986cm^{-1}, see Fig. 5-5(a). The mid-IR loss in DFB devices remains virtually unchanged, compared to Fabry-Perot lasers, at these two wavelengths. We can verify this fact by noting that the threshold current density remains around the same for Fabry-Perot and grating-based devices. As a result, the population will clamp when the gain at either lasing wavelengths reaches the loss.

Given that the gain cross-section at both lasing wavelengths is nearly the same, we calculate $\Delta N \approx 8.5 \times 10^{14}$ cm^{-3}. Using this value we calculate $\chi^{(2)}$ = 21,000 – *i*7,500 pm/V and $\chi^{(2)}$ = 9,000 - *i*4,000 pm/V for the active regions presented in Fig. 5-1(a) and Fig. 5-1(b), respectively. We note that we used slightly larger linewidths for the mid-IR transitions, compared to that used in Refs. [30, 74, 75], and fixed computing errors made in these references, which resulted in reduction of theoretical values of $\chi^{(2)}$ in all structures. The new linewidth values are more consistent with experimental measurements.

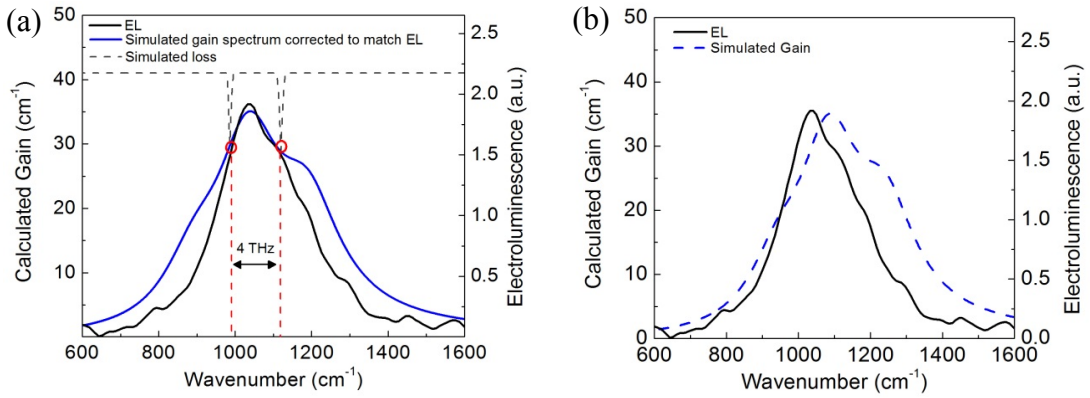

Figure 5-2, Simulated and measured mid-IR gain spectrum of the active regions: (a) Simulated gain spectrum (blue line, bottom and right axis) and electroluminescence (black line, bottom and left axis). Electroluminescence (EL) measurements were done at 298K with a 200μm-diameter mesa cleaved in half and operated at a current density of 7kA/cm^2. (b) Simulated gain red-shifted 50cm^{-1} to match EL spectrum. DFBs were used to select mid-IR lasing at 1120 cm^{-1} and 986 cm^{-1} (shown in red), corresponding to 4THz. The population density in the upper laser state clamps when the gain at these two lasing frequencies equals the loss (shown in grey).

5.2 Optimized Cherenkov waveguide design

Three major modifications were made in the structure of the current devices compared to the proof-of-principle devices. Firstly, the new devices use a 200-nm-thick InGaAs current extraction layer n-doped to 7×10^{17} cm^{-3} and separated from the active region by a 3-μm-thick layer of InP n-doped to 1.5×10^{16} cm^{-3}, as opposed to 3-μm-thick InP lower cladding and current injection layer n-doped to 10^{17} cm^{-1} used for devices in Chapter 4. The sheet resistance of the current injection layer is calculated using

$$R_s = \frac{\rho}{t} = \frac{1}{q \cdot \mu \cdot n \cdot t} \tag{5.4}$$

where q is the electron charge, μ is the electron mobility in InGaAs, n is the carrier concentration and t is the layer thickness. Higher electron mobility in InGaAs compared

to InP allowed us to maintain the same low sheet resistance (~100 Ω/sq) while using smaller sheet doping density for the current extraction layer. Plane wave transfer matrices calculations shows that the new current extraction layer has 80-90% transmission for the exiting THz Cherenkov wave at 3-4 THz as opposed to only 20-40% transmission for the current extraction layer in Ref. [75]. Secondly, optical nonlinearity was integrated in both mid-IR active region stacks. This effectively doubles the interaction length of the Cherenkov wave with the nonlinear material. Lastly, waveguide cladding layers thickness and doping were adjusted to provide for low THz loss and constructive interference between reflected upward and downward propagating Cherenkov waves.

To observe the effect of these modifications, we modeled the Cherenkov emission as a leaky slab-waveguide mode with the propagation constant fixed at β_1-β_2. The calculated squared magnitude of the H-field for the TM-polarized Cherenkov wave ($|H_y|^2$) for our devices are shown in Fig. 5-3(b) along with the refractive index profile for the case of 4 THz emission. For comparison, Fig. 5-3(c) plots the same data for the non-optimized proof-of-concept devices. The simulations assumed 25-μm-wide ridge devices with mid-IR pumps operating in TM_{00} mode, each with 1.4 W of optical power propagating inside of the waveguide. Simulation results predict about ten times improvement in Cherenkov wave intensity in the substrate compared to our proof-of-principle devices assuming the same ridge width and pump power.

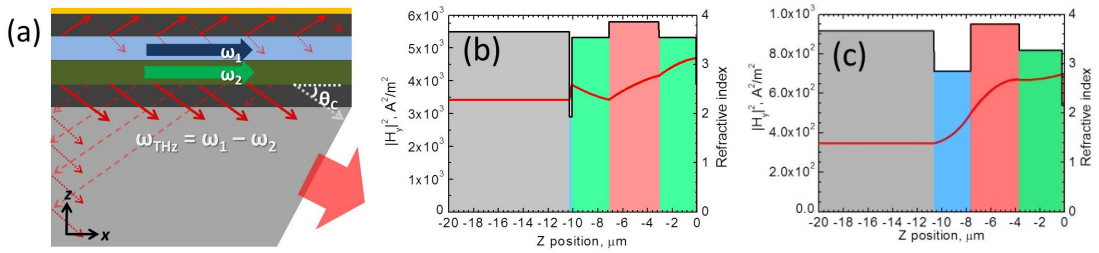

Figure 5-3, Cherenkov waveguide geometry and mode profile: (a) Schematic of Cherenkov THz DFG in our devices. (b,c) Calculated square of H-field in the TM-polarized THz Cherenkov waves (red lines, left axes) and waveguide refractive index profiles (black lines, right axes) at 4 THz for (b) optimized devices reported here and (c) proof-of-principle devices in Ref. 1. The gold contact layer is positioned at z=0, cladding layers are shown in green, current injection layers in blue, active regions in red, and substrate in grey.

5.3 Device performance

Structures were grown on semi-insulting InP substrates. The laser structure was grown by molecular beam epitaxy (MBE) on a 350-μm-thick semi-insulating InP substrate. The growth commenced with a 200-nm-thick InGaAs current injection layer (Si,7x10^{17} cm^{-3}), followed by a 3-μm-thick InP lower cladding doped (Si,1.5x10^{16} cm^{-3}). The active region was grown next and made with an $In_{0.53}Ga_{0.47}As/In_{0.52}Al_{0.48}As$ heterostructure lattice-matched to InP. It comprised of 33 repetitions of the $\lambda_1 = 9.20$ μm design followed by 33 repetitions of the $\lambda_2 = 8.20$ μm design. The top cladding layer consisted of 3-μm-thick InP (Si,1.5×10^{16} cm^{-3}), followed by a 100-nm-thick InP layer (Si, 3×10^{18} cm^{-3}) and terminated with a 10-nm-thick InGaAs contact layer (Si, 2x10^{19} cm^{-3}). Samples were processed into dry-etched ridge waveguides via inductive plasma etching. Ridge widths varied between 18 μm to 40μm. The sidewalls of the ridges were insulated with a 400-nm-thick layer of silicon nitride, followed by Ti/Au (15nm/800nm) contact

metallization. The wafer was cleaved into laser bars approximately 1mm - 2mm long. The 350-μm-thick InP substrate associated with the THz exit facet of the device was mechanically polished at a 30 degree angle for the THz Cherenkov wave outcoupling with Al_2O_3 lapping film.

Fabry-Perot devices produced broadband mid-IR emission with a typical spectrum displayed in Fig. 5-4(a). The corresponding THz spectrum, shown in Fig. 5-4(b), is centered around 3 THz and has equally spaced modes that span over 2.5 THz. This is the broadest room-temperature THz emission from a single device to our knowledge. The mid-IR and THz L-I and I-V is given in Fig. 5-4(c) and a maximum THz power of 3 μW.

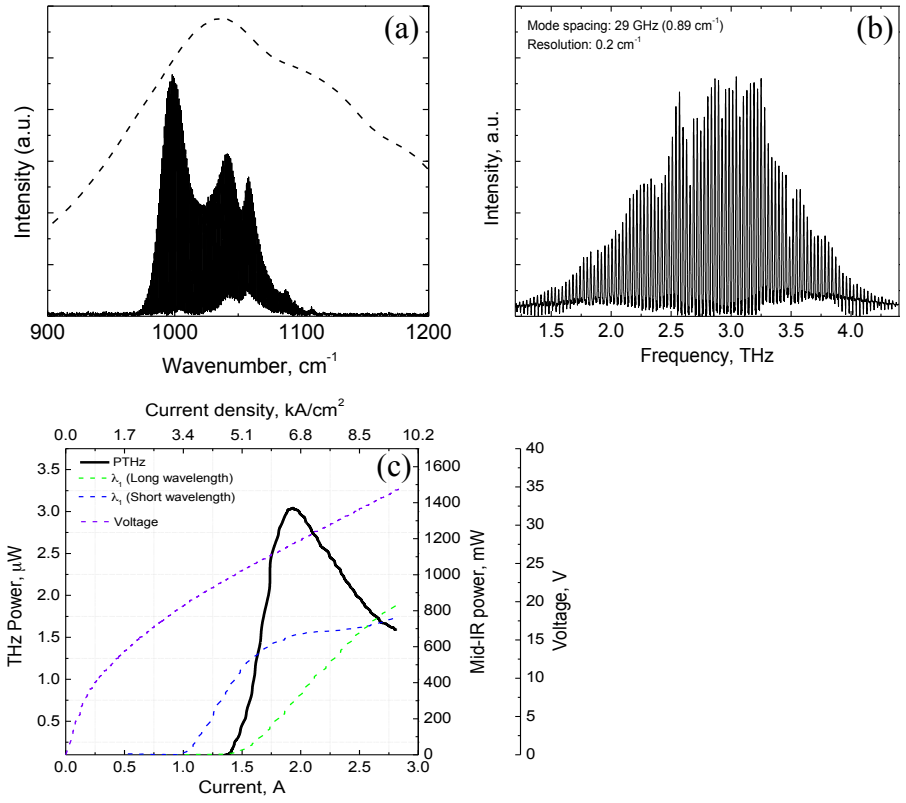

(Figure 5-4 continues on next page)

Figure 5-4, Fabry-Perot laser performance (stated on previous page): (a) Mid-infrared spectrum of a typical Fabry-Perot cavity device operated in pulsed mode at room temperature. Also shown is the electroluminescence (dashed line) from a 200μm-diameter mesa at a current density of 7kA/cm^2 that is indicative of the gain spectrum of our lasers. (b) Corresponding THz spectrum measured with a time resolved step-scan with a 0.2 cm^{-1} resolution in a N_2 purged atmosphere. (c) Mid-IR and THz current-voltage and power-current curves.

To produce narrowband THz sources, devices were processed as dual-color surface distributed feedback (DFB) gratings for the mid-IR lasers as shown in Fig. 5-4(a). Gratings with periods Λ_1 and Λ_2 alternating every 1 mm were written using electron beam lithography and were etched 130-nm-deep into the upper waveguide cladding. COMSOL Multiphysics simulated the coupling coefficient κ as a function of etch depth for each wavelength and followed the same procedure outlined in Ref. [91]. A model of the waveguide structure with a two periods of the grating was constructed. Periodic boundary conditions were applied. Gold covers the top surface of thee grating and a drude model was used to compute the refractive index parameters at mid-IR frequencies. For a given etch depth, waveguide eigenfrequency simulations were carried out and resulted in three different modes close to the expected mode frequency of the grating. The results are plotted in Fig. 5-5(a) and the three solutions correspond to a mid-IR modes confined in the active region and localized under the grating trough (mode 1), confined in the active region and localized under the grating peak (mode 2), and attached to the top metal as a surface plasmon (mode 3). The grating coupling coefficient, κ, relates to the difference in eignenfrequency between mode 2 and modes 1 or 3, and is computed following a procedure given in [91]. The coupling coefficient vs. etch depth for

three different mid-IR wavelengths is shown in Fig. 5-5(b). For an etch depth of 130 nm, κ is approximately 20 cm^{-1} for both λ_1 and λ_2 pumps.

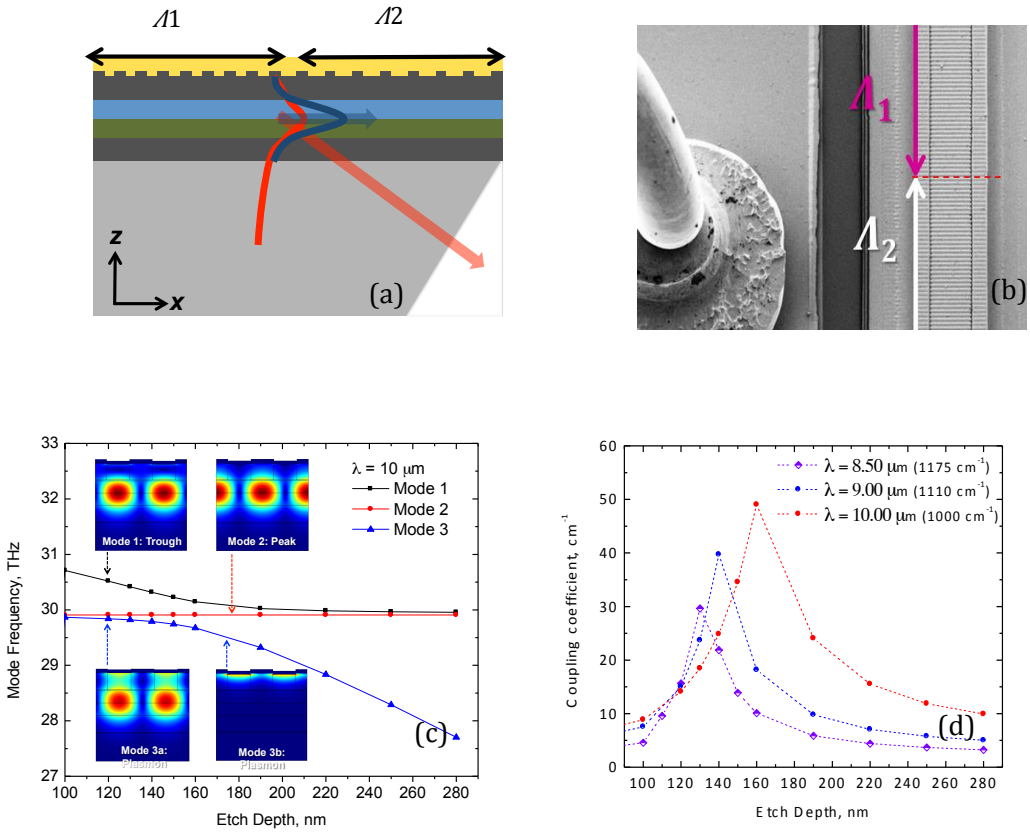

Figure 5-5, Dual period distributed feedback gratings for narrow linewidth THz emission: (a) Schematic of a dual-period surface DFB grating cavity with a Cherenkov waveguide. Colored regions indicate top gold contact (yellow), active regions with nonlinearity (blue and green), cladding layers (dark grey) and substrate (light-grey). Cherenkov THz radiation (red) is emitted into the substrate. Dual-color lasers presented in this paper had an approximately equal length of gratings sections Λ_1 and Λ_2. (b) SEM of dual period surface gratings. (c) Mid-infrared eigenfrequency vs etch depth for distributed feedback grating simulations (d) grating coupling coefficient vs. etch depth.

Room-temperature performance results are presented in Fig. 5-6 for a 1.7-mm-long x 25-μm-wide ridge laser with uncoated facets. The mid-IR emission spectrum,

collected at the laser pump current providing the maximum mid-IR power output, is shown in Fig. 5-5a inset. The laser operated dual-wavelength emission at λ_1 = 8.93 μm and λ_2 = 10.14 μm over the entire dynamic range with a better than 20 dB side-mode suppression ratio. Some additional peaks are located in the mid-IR spectra at around 9.5 μm for this particular device and are 10 dB lower in power compared to the pumps. We note that these peaks may likely be eliminated if anti-reflective coatings are applied to the laser facets, which was not done to our devices. Other devices have no such 'parasitic' peaks (see, e.g., Fig. 5-7). The L-I and V-I characteristics for the mid-IR power output is displayed in Fig. 5-6(a). The threshold current density was approximately the same as Fabry-Perot devices fabricated with the same wafer, indicating that the grating introduced negligible waveguide loss for the pumps. The corresponding THz spectrum is shown in Fig. 5-6(b). The inset shows a side mode suppression ratio better than 25 dB. Fig. 5-6(c) plots THz power output versus the product of the two mid-infrared pump powers. Nearly 120 μW of THz power output was recorded in a simple two-parabolic-mirror setup without any correction for collection efficiency. A linear increase of THz power is observed with a 0.6 mW/W^2 conversion efficiency, more than an order of improvement over Cherenkov DFG-QCLs with non-optimized waveguide structures [75, 76]. The inset in Fig. 5-6(c) plots the THz output wall-plug efficiency as a function of current over the dynamic range of the device. A maximum efficiency of 0.9×10^{-6} is observed at the device rollover point.

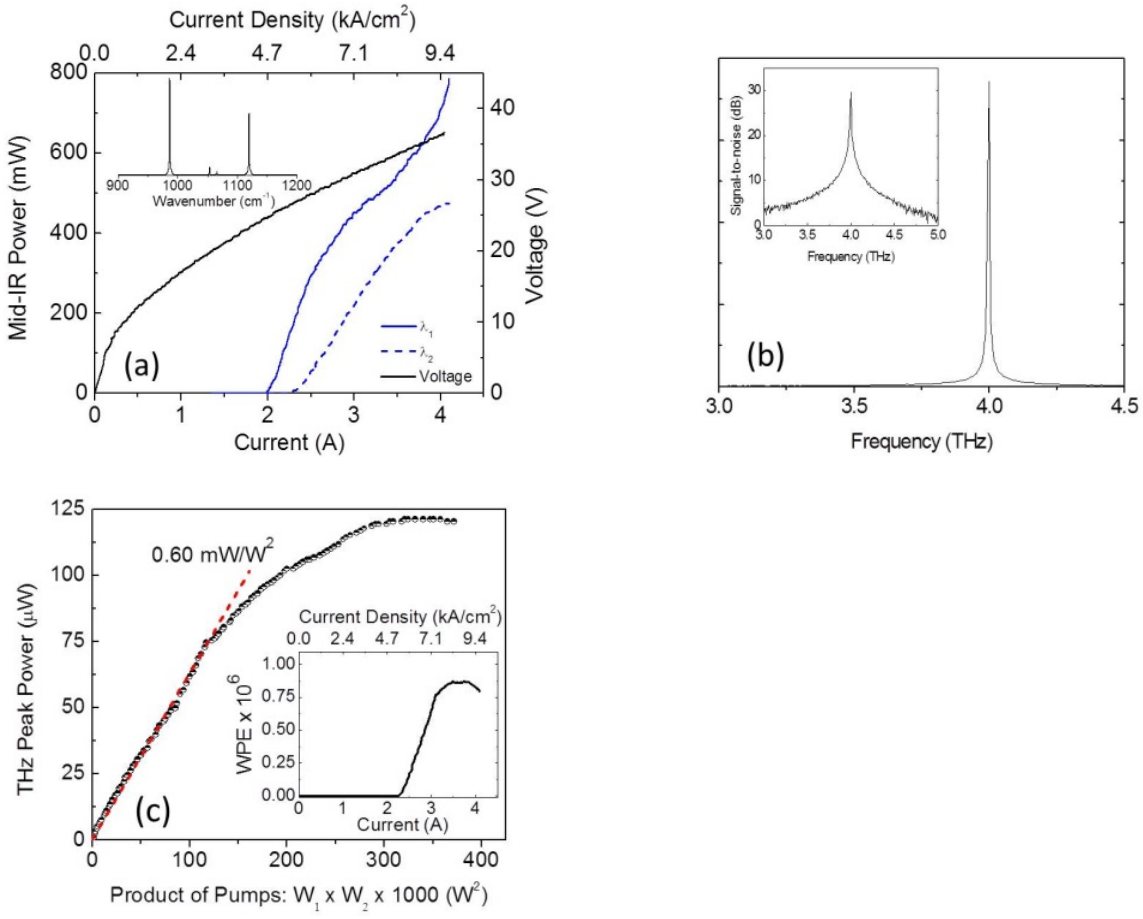

Figure 5-6, Performance of a 4 THz source: Spectral performance of a 1.70mm-long x 25μm-wide dual-period DFB grating device at room temperature. (a) Mid-infrared pump performance. Peak power (blue lines, bottom and left axis) and voltage (black line, bottom and right axis) vs. current density. Mid-IR power data is corrected for measured 70% mid-IR collection efficiency of our setup. (inset) Mid-IR emission spectrum of the device at current density of 9 kA/cm^2. (b) Corresponding THz emission spectrum taken at 9 kA/cm^2. (inset) The same spectrum in logarithmic scale. (c) Terahertz peak power output versus the product of peak mid-infrared pump powers. (inset) Terahertz output wall-plug efficiency versus current.

We also fabricated devices with mid-IR DFB gratings designed for a pump frequency separation at 2 and 3 THz. The room-temperature mid-IR and THz emission

spectra of these devices is shown in Fig 5-7(a) and the THz power as a function of the product of the mid-IR pump powers is shown in Fig. 5-7(b). The 2 THz source produced nearly 12 μW of power with a constant 0.09 mW/W^2 conversion efficiency and the 3 THz source generated 36 μW of power with a conversion efficiency of 0.4 mW/W^2 at low bias.

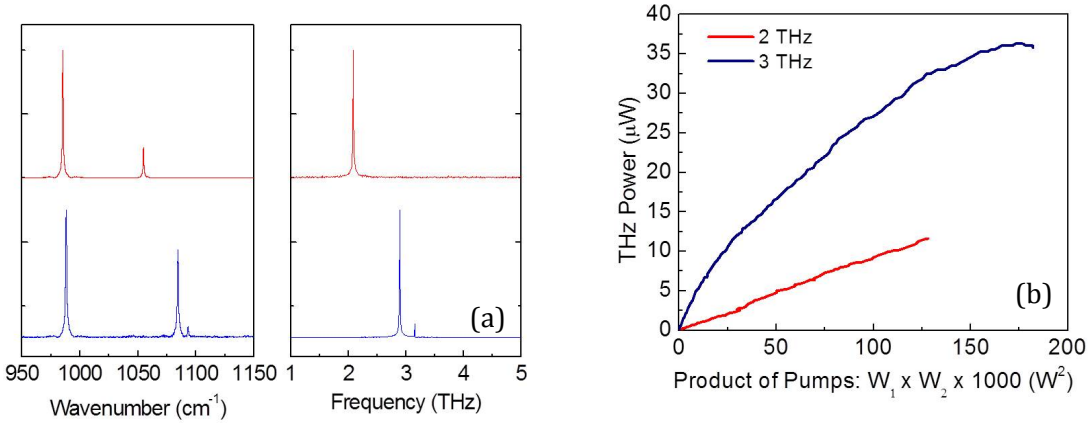

Figure 5-7, Performance of 2 THz and 3 THz sources: Performance of 2 THz (pink line), 3 THz (blue line) sources. (a) Mid-infrared and THz spectral performance taken with a 0.2cm^{-1} resolution. (b) Terahertz peak power output versus the product of mid-infrared pump powers.

Figure 5-8 displays the far-field profile taken at the maximum THz power output for the 4 THz device discussed above. The bolometer was placed 15cm away from the sample and swept in the planes indicated in the figure inset. A narrow emitting field 4 degrees above normal incidence is obtained in the xz-plane. Directional THz output is a natural consequence of Cherenkov emission process, which results in the whole polished substrate facet acting as THz emitter. In that regard, our Cherenkov THz-DFG sources are conceptually similar to THz QCLs with plasmonic collimators that make the whole substrate facet to act as THz emitter [92]. The maximum intensity is measured at +4^o

which corresponds to an emission angle of approximately 21 degrees in the substrate, in agreement with theoretical expectations. We note that the THz radiation emission angle can be adjusted by an appropriate choice of the substrate polish angle. Higher THz beam divergence is observed in the xy-plane, which is expected since the ridge width in our devices is only 25μm.

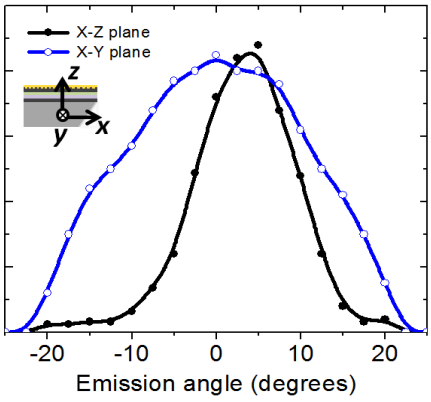

Figure 5-8, THz far-field emission profile of a 4 THz device: Far-field terahertz emission profile in horizontal and vertical plane for the device.

Cherenkov DFG scheme allows for efficient extraction of THz radiation along the whole length of the QCL waveguide at any THz frequency. Since mid-infrared frequencies in a QCL can be tuned well over 5 THz and optical nonlinearity for intracavity THz DFG is not expected to change significantly over several THz of tuning, Cherenkov DFG-QCLs are uniquely-suited to be operated as broadly-tunable THz sources for applications such as spectroscopy, microscopy, and drug or explosives detection. High-performance of the Cherenkov DFG-QCL chips reported here allowed us to demonstrate, for the first time, an external cavity (EC) DFG-QCL system which is

similar in mechanical design and operation to highly- successful widely-tunable mid-IR EC QCL systems [93]. A schematic of the setup is shown in Fig. 5-9(a). Primary system components include a 4-mm-diameter molded Chalcogenide glass plano-convex lens with a numerical aperture of 0.84 and a broadband anti-reflection coating in 8-12 μm and a gold-coated, 10.6-μm-wavelength-blazed grating with 150 groves per mm. We used a 1.7-mm-long 22-μm-wide ridge waveguide Cherenkov DFG-QCL device with contained a single period DFB grating over nearly the entire length of its waveguide. The grating parameters and processing was identical to that use for our single-mode THz DFG-QCL devices described earlier. This time, however, the grating period was kept constant to provide feedback at the mid-IR wavelength of λ_1 = 10.30 μm. The external cavity was then used to tune the lasing wavelength of the second mid-IR pump from λ_2 = 8.6μm to 9.8μm. The laser facets were left uncoated for this proof-of-concept demonstration. Mid-IR spectra and power of the mid-IR pumps at λ_1 and λ_2 are displayed in Fig. 5-9(b) for different grating angles. The spectra were taken at room temperature at a pump current density 8 kA/cm^2, close to the rollover point. The corresponding THz spectrum shown in Fig. 5-9(c) displays recorded emission spectra of the EC DFG-QCL system for operation between 1.70 to 5.25 THz. Single-frequency emission with a side-mode suppression ratio of better than 15dB is observed for nearly all THz signals with the exception for the THz emission at the periphery of the systems tuning range that have parasitic lasing peaks in the mid-IR spectrum corresponding to the active region gain peak. Anti-reflection coating for the mid-IR facets that are used for high-performance mid-IR EC QCLs is expected to suppress this parasitic lasing and improve the spectral purity. The power and conversion

efficiency at each THz wavelength is also plotted in Fig. 5-9(c). At 3.6 THz, a maximum power and conversion efficiency of 40 μW and 0.300 mW/W^2, respectively, is measured in general agreement with the conversion efficiency of DFB DFG-QCLs operating at 3 THz and 4 THz near the rollover point, cf. Fig. 5-6b and 6-6c, respectively.

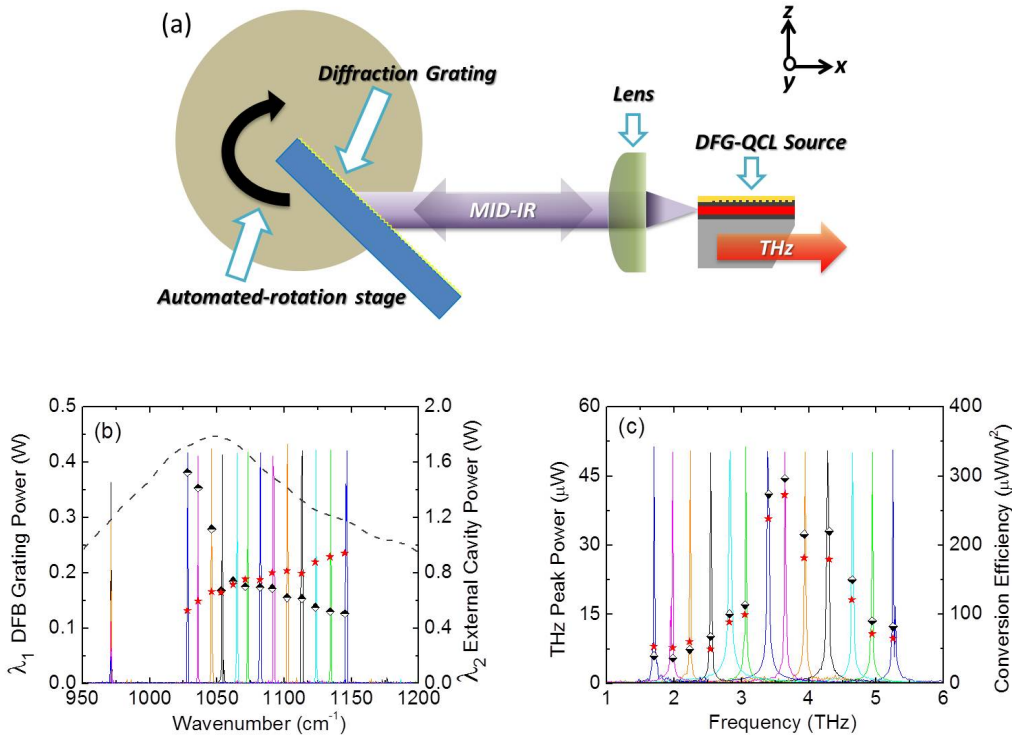

Figure 5-9, Broadband tuning with an external-cavity setup (continued on next page): (a) Schematic of the external-cavity system operated in the Littrow configuration. (b) Mid-IR spectra taken with a 0.2 cm^{-1} resolution. The electroluminescence spectrum (gray, dashed line) displaying the gain bandwidth of the active region. Also shown are the power of the tunable-wavelength λ_2 pump (red star, bottom and right axes) and that of the fixed-wavelength λ_1 pump (black-white diamond, bottom and left axes) as a function of λ_2 pump frequency. (c) Corresponding THz spectrum displaying a tuning bandwidth of 3.55 THz for our proof-of-concept external cavity

system. The THz power (red star, bottom and left axes) and conversion efficiency (black-white diamond, bottom and right axes) is shown for each wavelength.

The lasers were grown on a 350-μm-thick semi-insulating InP substrates with the output facet polished at 30 degrees for devices reported above. From simple geometrical considerations, assuming $\theta_C=20^o$ and a substrate polish angle of 30^o, only Cherenkov radiation generated within 1.15 mm from the exit facet can be outcoupled and radiation generated further away undergoes multiple reflections and is eventually absorbed in the substrate, see Fig. 5-3(a). We have measured an absorption coefficient of $\alpha = 15$ cm^{-1} at 4 THz for the substrates used in our devices (see Fig. 5-10). For our particular case, 50% of power in the Cherenkov wave generated from the 1.15mm-long section and propagating towards the output facet is lost to absorption. Furthermore, the output facet in our devices does not have any anti-reflection coatings and transmits only an estimated 72% of incident THz power. Finally, we note that Cherenkov waves are generated towards both front and back facet of the laser and we only collect the wave that propagates towards the front facet. Thus, for a 1.7 mm-long DFB device described in the text, only 12% of total generated THz power in Cherenkov waves is being outcoupled. The theoretical estimate for the conversion efficiency in our devices may be obtained from Fig. 5-3(b), using a 1.15-mm-long section of the laser waveguide that contribute to the outcoupled Cherenkov wave, and correcting the Cherenkov wave power for 50% absorption loss in the substrate, and 28% reflection loss at the facet. We obtain the value of 2.65mW/W^2, close to that measured experimentally.

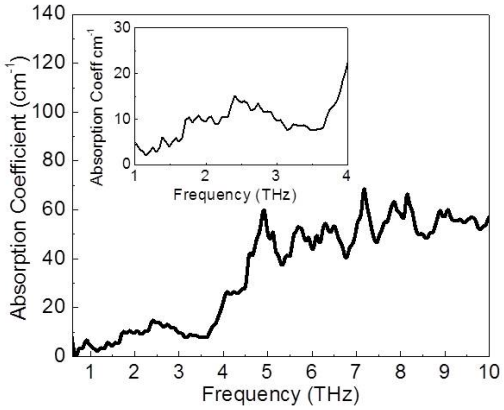

Figure 5-10, InP absorption: The absorption spectrum taken for a semi-insulating InP wafer 1050 μm-thick.

The wall-plug efficiency of the 4 THz DFG-QCL source peaks at approximately 0.9×10^{-6} near rollover point, see Fig. 5-6(c) inset. In comparison, THz QCLs systems integrated with pulsed-tube cryorefrigerators or Stirling cryocoolers [94] have a wall-plug efficiency of about 10^{-5}, once taking into account the power consumption of the cooling system. Clearly, a cryocooler also adds to the system size and complexity. Given the rapid progress of THz DFG-QCL technology one may expect significant improvement wall-plug efficiency in future generation of sources. Manley-Rowe relations may be viewed as the fundamental limit on wall-plug efficiency for THz DFG systems. From this perspective, given the current record values for room-temperature pulsed-operation wall-plug efficiency of mid-IR QCLs of 27% at $\lambda \approx 5\mu m$ [95] and 6% at $\lambda\approx10\mu m$ [96], we obtain the Manley-Rowe-limited wall-plug efficiency value of approximately 10^{-2} for 4 THz generation in DFG-QCLs at room temperature.

Chapter 6: MOVPE foundry grown THz DFG-QCL sources

An important milestone for THz DFG-QCL technology is the demonstration of high-performance sources grown by a foundry service. Successful chip performance will verify the commercial feasability of THz DFG-QCL sources and systems. In this chapter, we present the first demonstration of room-temperature THz-DFG QCL sources grown by metal organic vapor phase epitaxy (MOVPE) at a commercial foundry and discuss optimized structures with integrated nonlinearity for 3.5 THz generation. The latter part of this chapter describes modeling and testing different active region designs for high performance THz DFG-QCLs.

6.1 Bound-to-continuum and two-phonon resonance active region with $\chi^{(2)}$

THz-DFG QCLs are made with the InP heterostructure system and can be grown and processed in standard telecommunication laser diode foundries which significantly enhances their commercial appeal. The preferred growth method in industry is metal organic vapor phase epitaxy (MOVPE) due to the possibility of high-volume production of devices. High-performance InP-based QCLs have been demonstrated [8-10] with this growth technique.

We designed an active region made up of two stacks of QCL stages designed for emission at λ_1 = 9.2 μm and λ_2 = 10.2 μm. The calculated bandstructure and squared-moduli of the electron wave functions for one period of these structures are depicted in Fig. 6-1. Compared to Ref. [75], the doping in the active region stacks was lowered by 20% to reduce the free carrier THz absorption loss. Optical nonlinearity was engineered by adjusting the injection barriers' thickness such that the injector wavefunctions anti-

A portion of this work has been published in K. Vijayraghavan, M. Jang, A. Jiang, X. Wang, M. Troccoli, and M. A. Belkin, M, "THz Difference-Frequency Generation in MOVPE-Grown Quantum Cascade Lasers", *IEEE Photonics Technology Letters*, 26 (4), 391-394 (2014). All authors contributed to this work.

cross with the lower laser level. This results in the splitting of the lower laser level into two well-coupled states designed with an energy separation of 3.5 THz. As a result of the modifications, both active region stacks now possess optical nonlinearity. The mid-IR emission was designed for dual wavelength lasing around $\lambda_1 = 9$ µm and $\lambda_2 = 10$ µm and the combined nonlinearity for the structure, calculated in a formalism described in the previous chapter, is $|\chi^{(2)}| \sim 10$ nm/V at a clamping population of $n = 8.2 \times 10^{14}$ cm^{-3}. We note that the bandstructure of the redesigned 'two-phonon resonance' section, shown in Fig. 6-1(b), has been optimized to achieve maximum optical nonlinearity close to the rollover point.

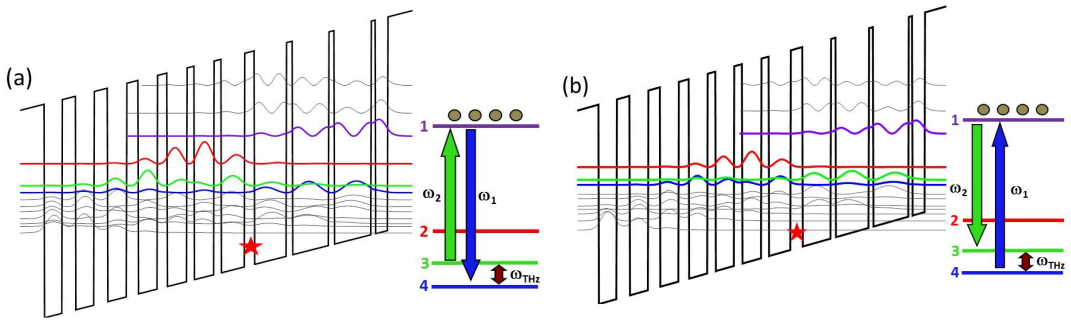

Figure 6-1, Bandstructure Diagram of AT002 (continued on next page): Conduction band diagram and bias for one period of active region (a) bound-to-continuum (BTC) stack producing radiation around 9.20 µm and (b) two-phonon resonance stack producing radiation around 10.20µm. Starting with the injection barrier, the layer sequence of the BTC stack is **40.0**/29.0/**22.0**/30.0/**22.0**/31.0/**19.0**/31.0/**16.0**/32.0/**12.0**/32.0/**12.0**/38.0/**16.0**/52.0/**10.0**/59.0/**9.0**/60.0/**7.0**/20.0/**40.0,** and for two-phonon resonance stack **39.0**/33.0/**24.0**/34.0/**22.0**/34.0/**19.0**/34.0/**15.0**/34.0/**15.0**/35.0/**14.0**/40.0/**22.0**/52.0/**9.0**/61.0/**8.0**/65.0/**7.0**/23.0/**39.0,** where the units are in angstroms, bold numbers indicate barriers, and underlined numbers indicate Si:doping of $n = 2.4 \times 10^{17}$cm^{-3} . Next to each bandstructure is a Schematic description of resonant DFG process. For the BTC active region, lasing at $\lambda = 9.20$ µm occurs between states 1-3. States

1-2 is in resonance around at λ = 10.20 μm and DFG interaction occurs between states 2-3. For the design in part(b), lasing at λ = 10.20 μm takes places between states 1-2, states 1-3 is resonant around λ = 9.20 μm. DFG interaction occurs resonantly between states 2-3.

6.2 Waveguide design

Three major modifications were made in the structure of the current devices compared to the proof-of-principle devices in Ref. [75]. Firstly, the new devices use a 200-nm-thick InGaAs current extraction layer n-doped to 1×10^{18} cm^{-3} and separated from the active region by a 3-μm-thick layer of InP n-doped to 1.5×10^{16} cm^{-3}, as opposed to 3-μm-thick InP lower cladding and current injection layer n-doped to 10^{17} cm^{-1} used for devices in Ref. [75]. Higher electron mobility in InGaAs compared to InP allowed us to maintain the same low sheet resistance (~70 Ω/sq) while using smaller sheet doping density for the current extraction layer. Plane wave transfer matrices calculations show that the new current extraction layer have 70-80% transmission for the exiting THz Cherenkov wave at 3-4 THz as opposed to only 20-40% transmission for the current extraction layer in Ref. [75]. Secondly, optical nonlinearity was integrated in both mid-IR active region stacks as described in the previous section. This effectively doubles the interaction length of the Cherenkov wave with the nonlinear material. Lastly, the waveguide cladding layers thickness and doping were adjusted to provide for low THz loss and constructive interference between reflected upward and downward propagating Cherenkov waves. The combination of changes for this structure is expected to boost the output power by a factor 2 – 4 with respect to the proof-of-principle design.

6.3 Device performance

The laser structure was grown by MOVPE on a 350-µm-thick semi-insulating InP substrate. The growth commenced with a 200-nm-thick InGaAs current extraction layer (Si, 10^{18} cm^{-3}), followed by a 3.5-µm-thick InP lower cladding (Si, $1.5x10^{16}$ cm^{-3}), and a 150-nm-thick InGaAs layer (Si, $1.5x10^{16}$ cm^{-3}). The active region was grown next and made with an InGaAs/InAlAs heterostructure lattice-matched to InP. It comprised of 33 repetitions of the two-phonon resonance design followed by 35 repetitions of the bound-to-continuum design. The average doping in each active region is around $4x10^{16}$ cm^{-3}. The top cladding layer consisted of a 300-nm-thick InGaAs layer (Si, $1.5x10^{16}$ cm^{-3}), 3-µm-thick InP (Si, $1.5x10^{16}$ cm^{-3}), followed by 500-nm-thick InP (Si, 3×10^{18} cm^{-3}) and terminated with a 20-nm-thick InGaAs current spreading layer (Si, 10^{19} cm^{-3}).

Samples were initially processed into Fabry-Perot ridge waveguides. All testing was done at room-temperature in pulsed mode at a duty cycle that did not exceed 1%. Emission spectra was measured with a Fourier Transform Infrared (FTIR) spectrometer and recorded with a helium-cooled bolometer and doped triglycine sulfate detector for the THz and mid-IR signals, respectively. The output power of devices was measured using an off-axis parabolic mirror setup and recorded with a calibrated thermopile and Golay cell manufactured by Tydex Instruments for the mid-IR and THz signals, respectively. The mid-IR measurements were corrected for a 70% collection efficiency. However, THz measurements were not corrected for any collection efficiency because of difficulty in accurately distinguishing between the THz signal and thermal background produced by the source in close proximity to the detector's entrance aperture.

Room temperature performance for a 1.20mm-long by 25μm-wide Fabry-Perot source is presented in Fig. 6-2. The substrate was polished at 30º angle to outcouple the Cherenkov wave. The combined power of the mid-IR pumps was 1.4W and a maximum THz peak power of 5μW was measured. The Fig. 6-2 inset displays the THz spectrum taken near the rollover point and broadband emission is centered at 3.5 THz and spans over a 1.2 THz bandwidth. This is a consequence of broad mid-IR lasing due to the wide spectral gain distribution of the active regions. Despite the lower sheet resistance of the current extraction layer, the device operating voltage is similar to our previously reports structures.

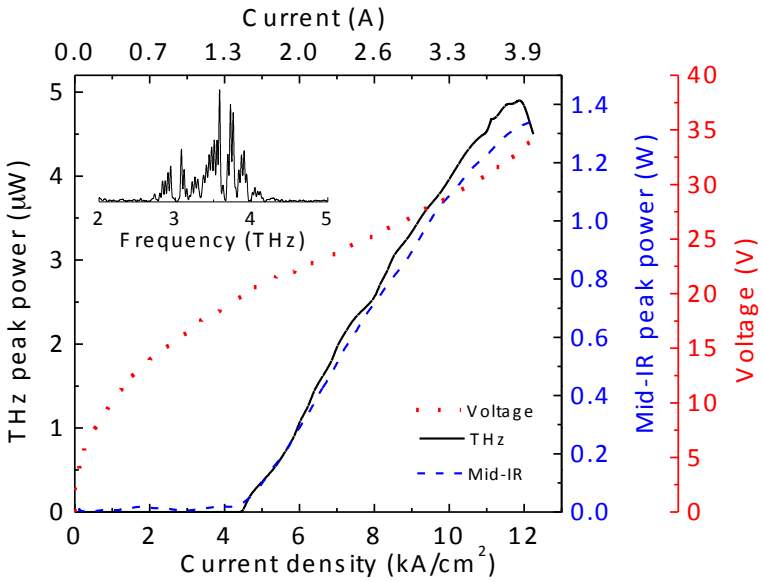

Figure 6-2 Fabry-Perot laser performance: Fabry-Perot cavity performance for 1.25mm-long x 25μm-wide device operated at room temperature with 100ns pulses and a 5kHz repetition frequency.(inset) THz spectra taken at 10 kA/cm^2.

Narrow-linewidth THz sources were processed using distributed-feedback (DFB) gratings for the mid-IR pumps. Surface DFB gratings were etched into the upper

waveguide to produce dual-wavelength single-mode mid-infrared emission. In order to achieve the appropriate coupling strength, the top cladding was etched 420 nm. We note that this increases the Schottky voltage of our devices. Two separate gratings with periods Λ_1 = 1.50 μm and Λ_2 = 1.65 μm alternating every 1 mm to select λ_1 and λ_2, respectively, were then defined by electron beam lithography and etched 140 nm by reactive ion etching. The grating coupling coefficient was simulated with Comsol and is approximately κ = 15 cm-1 for both pumps, as seen in Fig. 6-3. The wafers were then processed into standard ridge-waveguide devices.

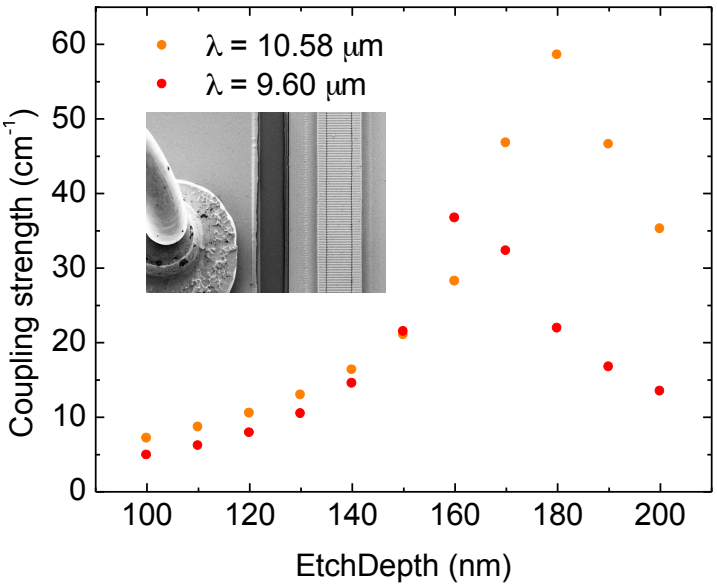

Figure 6-3, DFB coupling coefficient: The coupling strength is plotted as a function of grating etch depth. The inset shows a picture of the processed device.

Room-temperature performance results are presented for a 2-mm-long-by-18-μm-wide source with uncoated facets. The device substrate was polished at a 30º angle for Cherenkov wave outcoupling. All testing was done in a N_2 purged environment to eliminate absorption of the THz signal from water vapor. Fig. 6-4(a) shows narrow

linewidth emission at 3.5 THz. The mid-IR emission spectrum, collected at a 9 kA/cm^2 current density, is shown in the bottom inset of Fig. 6-4(a). The laser operated with dual-wavelength emission at λ_1 = 9.40 μm and λ_2 = 10.58 μm over the entire dynamic range. The long-wavelength mid-IR pump is single-mode with a 20 dB mode discrimination ratio and the short-wavelength pump had secondary lasing peak separated by 50 GHz and 7dB lower in magnitude. This manifests into a THz emission spectrum containing two peaks, with a maximum signal-to-noise ratio (SNR) of 25 dB as shown in the Fig. 6-4(a) top inset.

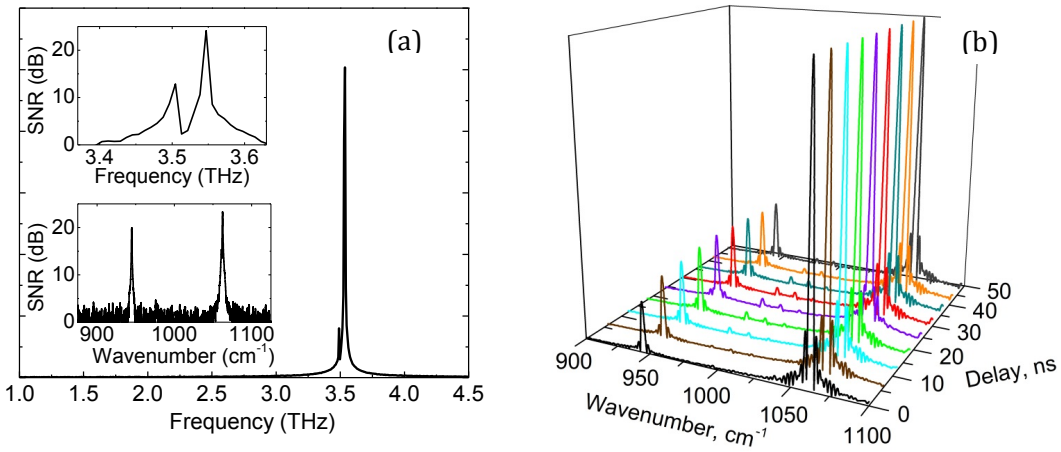

Figure 6-4, Emission spectra recorded with a 0.2 cm^{-1} resolution: (a) THz emission frequency recorded with a time-resolved step scan. (inset, top) Signal-to-noise ratio of the THz mode. A 25dB SNR is observed at 3.55 THz. (inset, bottom) Mid-IR spectra displaying dual-wave lasing at 9.40μm and 10.58μm. Signal-to-noise ratio (SNR) plotted as decibels vs. wavenumber. (b) Time dependent lasing characteristics of the mid-IR pump over a 50ns applied pulse.

Multiwavelength QCLs operated in pulse mode have been shown to commence lasing at different wavelengths over the duration of the bias pulse [97]. Efficient THz DFG requires the mid-IR pumps λ_1 and λ_2 to synchronously lase at the beginning and end

of the applied pulse. The time-dependent lasing in our single color THz source was measured using a gated integrator and a fast MCT detector with a 3ns rise time to measure the signal. The device operated with a 50 ns pulse width and a 3 ns gate width. Spectra was taken with 3 ns time slices and the results are shown in Fig. 6-4(b). Both pumps operated simultaneously over the pulse duration and this is consistent from 5 kA/cm^2 to 9 kA/cm^2 at which point λ_2 begins to roll over (see Fig. 6-5).

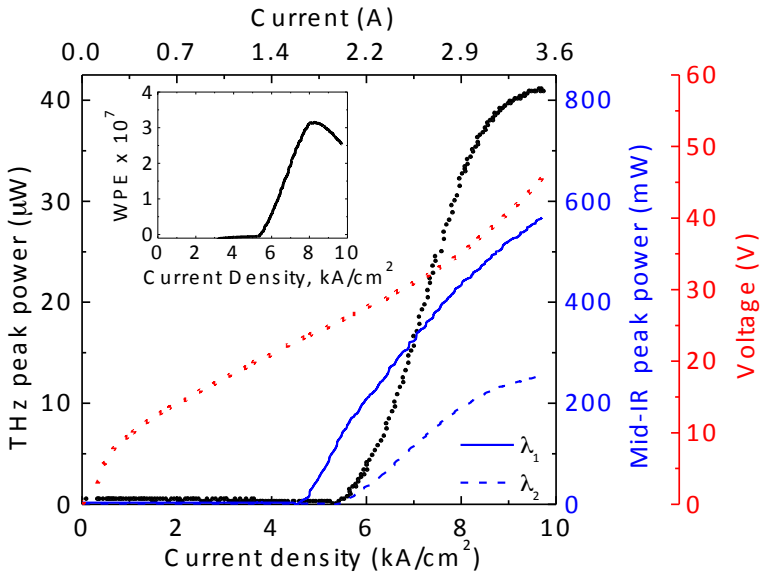

Figure 6-5, Performance of a 2.00mm-long x 18μm-wide dual-period DFB grating device operated at room temperature: Terahertz peak power (black line, bottom and left axis), the mid-IR pump power (blue lines, bottom and inner right axes), and voltage (red line, bottom and outer right axis) vs. current density. (inset) Terahertz wall plug efficiency versus current density.

The L-I-V characteristics for the mid-IR and THz signals are shown Fig. 6-5 and nearly 40 μW of THz peak power output was observed. It should be noted that the mid-infrared pump power is a factor of two smaller and the threshold current density is larger compared to the Fabry-Perot devices. This is in contrast to previously reported devices

where both parameters were roughly equivalent for broadband and narrowband sources[78]. In this particular case, we may be experiencing overcoupled feedback which could be alleviated by reducing the grating etch depth. Improved THz performance may also be achieved by optimizing the relative performance of each mid-IR pump. The THz dynamic range and maximum power can be increased if both pumps turn on at the same bias and have equal power. However, realizing this is challenging due to a combination of gain competition in dual wavelength QCLs [90], differences in the waveguide loss for each pump, and additional nonlinear effects such as optical parametric amplification.

The Fig. 6-5 inset plots the device wall plug efficiency (WPE) and it peaks at $3x10^{-7}$, a factor of two smaller compared to state-of-the-art sources [78, 98]. Compared to the Fabry-Perot device described in Fig. 6-2, the operating voltage for this source is large due to etching of the top contact layer during grating fabrication. A redesigned top cladding structure providing sufficient coupling for surface DFB gratings while maintaining a low Schottky voltage is expected to produce a WPE comparable to or better than currently reported THz-DFG QCLs [78, 98]. Fig. 6-6 plots the THz power output versus a product of the two mid-infrared pump powers. A linear increase of THz power is observed with a 0.36 mW/W^2 conversion efficiency prior to rollover. The conversion efficiency experiences a rollover at high mid-IR pump powers likely due to a change in the QCL bandstructure alignment at high current/high bias voltages which reduces the value of optical nonlinearity in the active region. The rollover is not as pronounced as that of devices in Ref. [78] due to an optimized bandstructure design for the section shown in Fig. 6-1.

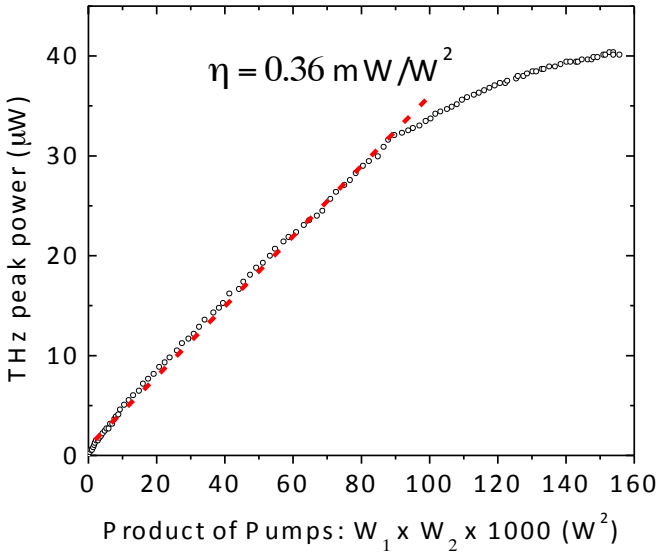

Figure 6-6, THz conversion efficiency: THz Peak power output versus the product of mid-infrared pump powers.

Chapter 7: Conclusion and outlook

Compared to well-established microwave, infrared, and visible optics markets, the THz industry is in its infancy and primed for significant growth, particularly if inexpensive mass-producible electrically-pumped semiconductor source technology is developed. A THz market analysis report projects $600 million total revenue by 2021 [15]. A revenue breakdown by industry and application is given in Fig. 1. THz spectroscopy and sensing is projected to be a $250 million industry by 2021. These numbers are conservative estimates based on current sales of THz spectroscopy systems and the increase in demand for sensor technology. The healthcare, manufacturing, and defense industries are expected to be the largest end-users (see Chapter 1).

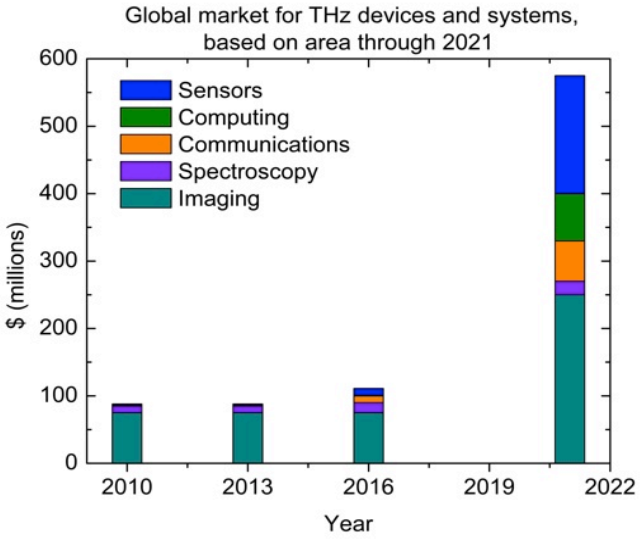

Figure 7-1, THz market breakdown: Projected THz market for various applications taken from Ref. [].

Table 1-1 highlights commercially available THz technology and there is a glaring absence of sources operating in the 3 - 6 THz spectral range at room-temperature. THz QCLs and THz-DFG QCL sources are best suited to operate in the aforementioned

spectral range. THz QCLs can operate continuous-wave, single mode with mW average power. They are best suited for applications where large system footprint, cryogenic cooling, and periodic maintenance are secondary concerns. Through my interaction with industry, room-temperature and easy-to-maintain systems are highly preferable. Unfortunately, the improvements in the temperature performance of THz QCLs has slowed significantly in recent years, as seen in Fig. 7-2. Unless new materials, new systems, or better growth techniques are developed, thermoelectrically-cooled and room-temperature operation is not likely in the near future. Additionally, tunable THz QCLs inherently have a small tuning bandwidth and complicated design that requires MEMs-integrated technology [26].

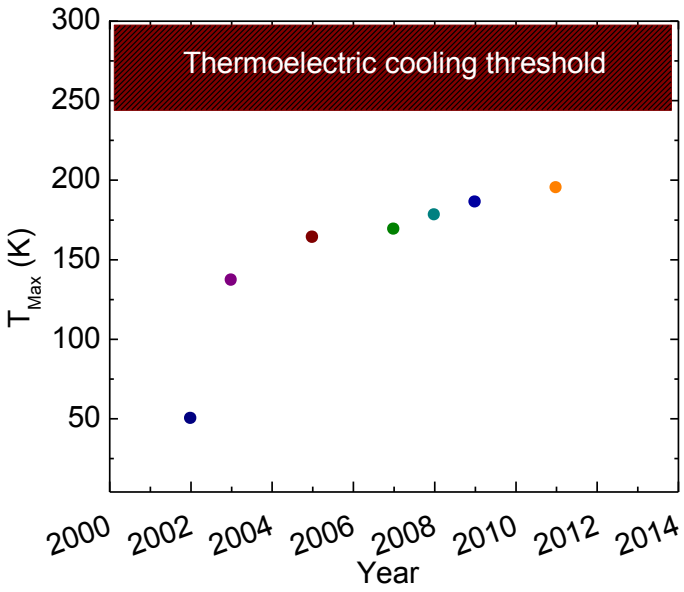

Figure 7-2, Maximum operating of THz QCLs: There was rapid progress improving the temperature performance of THz QCLs soon after the first demonstration in 2002. Over the past 5 years the progress has slowed considerably.

Contrastingly, THz-DFG QCL source are primed to emerge as a feasible technology and Fig. 7-3 highlights the progress made in the past 7 years. These sources operate at room temperature with a record spectral coverage and tuning range compared to similar semiconductor technology. One of the drawback with this technology is the small output power. But recently devices with optimized thermal management and packaging has demonstrated continuous-wave operation with microwatt power and pulsed operation with mW peak power [99]. These power levels are approaching the threshold required for application development. Spectroscopy and raster scan imaging can be done with 10 μW - 100 μW average THz power using room-temperature Golay cells, pyroelectric detectors, or uncooled microbolometer elements. Real-time imaging is the preferred mode and a MIT group demonstrated QCL-based imaging at frame rates better than 20 Hz using uncooled microbolometer cameras with a noise-equivalent-power (NEP) of 320 $pW/Hz^{1/2}$ [100]. They showed that approximately 150 μW peak power (50 μW average power) at a sample position was sufficient to image a maple tree seed pod in transmission mode. It should be noted that the microbolometer detector used in their demonstration was optimized for mid-IR detection (λ = 7 – 15 am). Recently, Dr. Naoki Ode at SOLTEC corp. has demonstrated QCL-based imaging using a THz microbolometer camera with 30 – 100 $pW/Hz^{1/2}$ NEP and we may expect further improvements in THz detector technologies in the future.

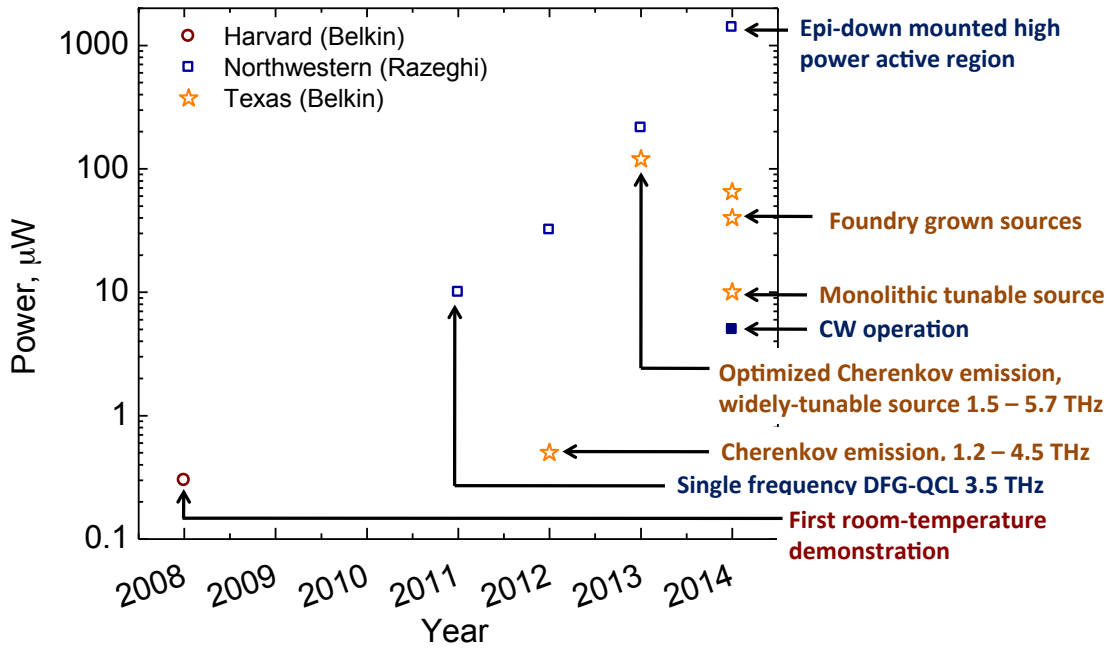

Figure 7-3, Progression of room-temperature THz DFG-QCL performance: After the first demonstration by Harvard (open circle, red), work on improving THz DFG-QCLs is primarily being done by The University of Texas (open star, orange) and Northwestern University (squares, blue).

There is still significant room to improve the THz power output of devices by implementing optimized bandsturctures and using higher effieciency THz outcoupling schemes. For devices reported in this dissertation, we estimate that only 24% of the forward going THz wave power and 12% of the total THz power, including backward going THz wave, generated in a 1.7-mm-long device outcouples to free space. This value is based on an estimated 30% reflection loss for THz radiation at the uncoated laser facet and 66% absorption loss for a forward-going THz wave based on measured absorption of semi-insulating InP substrates shown in Fig. 5-10. Thus significant improvements in power output of these devices are expected from simply developing efficient mechanisms for Cherenkov emission extraction from the active region. This may accomplished by

using prisms affixed to either the device substrate or upper cladding, implementing second or third order gratings that extract the THz radiation along the entire device length, or by replacing the semi-insulating InP substrate with a high-resistivity float zone silicon substrate (HRFZ-Si). Compared to S.I. InP, high-resistivity silicon has an order of magnitude smaller THz absorption coefficient due to the absernce of a Restrahlenband. Plane wave transfer matrix calculations estimates the extraction of THz Cherenkov radiation through a 350-μm-thick semi-insulating InP substrate results in a 66% absorption loss in power generated from the 1.70 mm-long and 25 μm-wide device. For the same device dimensions, a 3 times improvement in power is expected by extracting THz radiation through a high-resistivity float zone silicon substrate. Additionally, HRFZ-Si has a near constant refractive index and was recently shown to supress the variation in the far-field angle for different THz emission frequencies in DFG-QCL devices [80] and is benefical for tuning systems.

References

[1] M. Tonouchi, "Cutting-edge terahertz technology," *Nature Photonics,* vol. 1, pp. 97-105, Feb 2007.

[2] C. Jördens and M. Koch, "Detection of foreign bodies in chocolate with pulsed terahertz spectroscopy," *Optical Engineering,* vol. 47, pp. 037003-037003-5, 2008.

[3] A. Gowen, C. O'Sullivan, and C. O'Donnell, "Terahertz time domain spectroscopy and imaging: emerging techniques for food process monitoring and quality control," *Trends in Food Science & Technology,* vol. 25, pp. 40-46, 2012.

[4] P. F. Taday, "Applications of terahertz spectroscopy to pharmaceutical sciences," *Philosophical Transactions of the Royal Society of London Series a-Mathematical Physical and Engineering Sciences,* vol. 362, pp. 351-363, Feb 15 2004.

[5] C. S. Joseph, A. N. Yaroslavsky, V. A. Neel, T. M. Goyette, and R. H. Giles, "Continuous wave terahertz transmission imaging of nonmelanoma skin cancers," *Lasers in Surgery and Medicine,* vol. 43, pp. 457-462, 2011.

[6] P. Lancaster, F. Carmichael, J. Britton, H. Craddock, D. Brettle, and V. Clerehugh, "Surfing the spectrum–what is on the horizon?," *British dental journal,* vol. 215, pp. 401-409, 2013.

[7] A. G. Davies, A. D. Burnett, W. Fan, E. H. Linfield, and J. E. Cunningham, "Terahertz spectroscopy of explosives and drugs," *Materials Today,* vol. 11, pp. 18-26, 2008.

[8] P. H. Siegel, "THz instruments for space," *Antennas and Propagation, IEEE Transactions on,* vol. 55, pp. 2957-2965, 2007.

[9] P. H. Siegel, "Terahertz technology," *IEEE Transactions on microwave theory and techniques,* vol. 50, pp. 910-928, 2002.

[10] J. F. Federici, B. Schulkin, F. Huang, D. Gary, R. Barat, F. Oliveira*, et al.*, "THz imaging and sensing for security applications—explosives, weapons and drugs," *Semiconductor Science and Technology,* vol. 20, p. S266, 2005.

[11] C. M. Armstrong, "THE TRUTH ABOUT TERAHERTZ-No other region of the electromagnetic spectrum has generated so much interest in recent years, but breathless hype still can't overcome the fundamental limits of physics," *IEEE Spectrum,* vol. 49, p. 28, 2012.

[12] H. Eisele, "State of the art and future of electronic sources at terahertz frequencies," *Electronics Letters,* vol. 46, pp. S8-S11, Dec 23 2010.

[13] T. W. Crowe, W. L. Bishop, D. W. Porterfield, J. L. Hesler, and R. M. Weikle, "Opening the Terahertz window with integrated diode circuits," *Ieee Journal of Solid-State Circuits,* vol. 40, pp. 2104-2110, Oct 2005.

[14] E. R. Brown, "Advancements in Photomixing and Photoconductive Switching for THz Spectroscopy and Imaging," *Terahertz Technology and Applications Iv,* vol. 7938, 2011.

[15] J. Faist, F. Capasso, D. L. Sivco, C. Sirtori, A. L. Hutchinson, and A. Y. Cho, "Quantum cascade laser," *Science,* vol. 264, pp. 553-556, 1994.

[16] M. Beck, D. Hofstetter, T. Aellen, J. Faist, U. Oesterle, M. Ilegems*, et al.*, "Continuous wave operation of a mid-infrared semiconductor laser at room temperature," *Science,* vol. 295, pp. 301-305, Jan 11 2002.

[17] A. Wittmann, Y. Bonetti, M. Fischer, J. Faist, S. Blaser, and E. Gini, "Distributed-Feedback Quantum-Cascade Lasers at 9 m Operating in Continuous Wave Up to 423 K," *Photonics Technology Letters, IEEE,* vol. 21, pp. 814-816, 2009.

[18] B. Gokden, Y. Bai, N. Bandyopadhyay, S. Slivken, and M. Razeghi, "High peak power (34 W) photonic crystal distributed feedback quantum cascade lasers," *Photonic and Phononic Properties of Engineered Nanostructures,* vol. 7946, 2011.

[19] J. Faist, C. Gmachl, F. Capasso, C. Sirtori, D. L. Sivco, J. N. Baillargeon*, et al.*, "Distributed feedback quantum cascade lasers," *Applied Physics Letters,* vol. 70, pp. 2670-2672, 1997.

[20] A. A. Kosterev, "Chemical sensors based on quantum cascade lasers," *Quantum Electronics, IEEE Journal of,* vol. 38, pp. 582-591, 2002.

[21] C. Gmachl, D. L. Sivco, R. Colombelli, F. Capasso, and A. Y. Cho, "Ultra-broadband semiconductor laser," *Nature,* vol. 415, pp. 883-887, 2002.

[22] G. Scalari, C. Walther, M. Fischer, R. Terazzi, H. Beere, D. Ritchie*, et al.*, "THz and sub-THz quantum cascade lasers," *Laser & Photonics Reviews,* vol. 3, pp. 45-66, 2009.

[23] B. S. Williams, "Terahertz quantum-cascade lasers," *Nature photonics,* vol. 1, pp. 517-525, 2007.

[24] L. Li, L. Chen, J. Zhu, J. Freeman, P. Dean, A. Valavanis*, et al.*, "Terahertz quantum cascade lasers with> 1 W output powers," *Electronics Letters,* vol. 50, pp. 309-311, 2014.

[25] S. Fathololoumi, E. Dupont, C. Chan, Z. Wasilewski, S. Laframboise, D. Ban*, et al.*, "Terahertz quantum cascade lasers operating up to∼ 200 K with optimized oscillator strength and improved injection tunneling," *Optics express,* vol. 20, pp. 3866-3876, 2012.

[26] Q. Qin, B. S. Williams, S. Kumar, J. L. Reno, and Q. Hu, "Tuning a terahertz wire laser," *Nature photonics,* vol. 3, pp. 732-737, 2009.

[27] M. Gurnick and T. DeTemple, "Synthetic nonlinear semiconductors," *IEEE Journal of Quantum Electronics,* vol. 19, pp. 791-794, 1983.

[28] C. Gmachl, A. Belyanin, D. L. Sivco, M. L. Peabody, N. Owschimikow, A. M. Sergent*, et al.*, "Optimized second-harmonic generation in quantum cascade lasers," *Quantum Electronics, IEEE Journal of,* vol. 39, pp. 1345-1355, 2003.

[29] M. A. Belkin, F. Capasso, A. Belyanin, D. L. Sivco, A. Y. Cho, D. C. Oakley*, et al.*, "Terahertz quantum-cascade-laser source based on intracavity difference-frequency generation," *Nature Photonics,* vol. 1, pp. 288-292, 2007.

[30] M. A. Belkin, F. Capasso, F. Xie, A. Belyanin, M. Fischer, A. Wittmann*, et al.*, "Room temperature terahertz quantum cascade laser source based on intracavity difference-frequency generation," *Applied Physics Letters,* vol. 92, p. 201101, 2008.

[31] R. Kazarinov and R. Sui-is, "POSSIBILITY OF THE AMPLIFICATION OF ELECTROMAGNETIC WAVES IN A," *Soviet Physics-Semiconductors,* vol. 5, 1971.

[32] C. Sirtori, F. Capasso, J. Faist, A. L. Hutchinson, D. L. Sivco, and A. Y. Cho, "Resonant tunneling in quantum cascade lasers," *Quantum Electronics, IEEE Journal of,* vol. 34, pp. 1722-1729, 1998.

[33] J. Faist, F. Capasso, C. Sirtori, D. L. Sivco, A. L. Hutchinson, and A. Y. Cho, "Vertical transition quantum cascade laser with Bragg confined excited state," *Applied physics letters,* vol. 66, pp. 538-540, 1995.

[34] J. Faist, F. Capasso, C. Sirtori, D. L. Sivco, A. L. Hutchinson, and A. Y. Cho, "Laser action by tuning the oscillator strength," *Nature,* vol. 387, pp. 777-782, 1997.

[35] J. Faist, M. Beck, T. Aellen, and E. Gini, "Quantum-cascade lasers based on a bound-to-continuum transition," *Applied Physics Letters,* vol. 78, pp. 147-149, 2001.

[36] J. Faist, *Quantum cascade lasers*: Oxford University Press, 2013.

[37] H. E. Beere, J. C. Fowler, J. Alton, E. H. Linfield, D. A. Ritchie, R. Kohler*, et al.*, "MBE growth of terahertz quantum cascade lasers," *Journal of Crystal Growth,* vol. 278, pp. 756-764, May 1 2005.

[38] R. Green, J. Roberts, A. Krysa, L. Wilson, J. Cockburn, D. Revin*, et al.*, "MOVPE grown quantum cascade lasers," *Physica E-Low-Dimensional Systems & Nanostructures,* vol. 21, pp. 863-866, Mar 2004.

[39] O. Cathabard, R. Teissier, J. Devenson, J. Moreno, and A. Baranov, "Quantum cascade lasers emitting near 2.6 mum," *Applied Physics Letters,* vol. 96, p. 1110, 2010.

[40] R. Köhler, A. Tredicucci, F. Beltram, H. E. Beere, E. H. Linfield, A. G. Davies*, et al.*, "Terahertz semiconductor-heterostructure laser," *Nature,* vol. 417, pp. 156-159, 2002.

[41] B. S. Williams, S. Kumar, H. Callebaut, Q. Hu, and J. L. Reno, "Terahertz quantum-cascade laser operating up to 137 K," *Applied Physics Letters,* vol. 83, pp. 5142-5144, Dec 22 2003.

[42] B. Williams, S. Kumar, Q. Hu, and J. Reno, "Operation of terahertz quantum-cascade lasers at 164 K in pulsed mode and at 117 K in continuous-wave mode," *Optics Express,* vol. 13, pp. 3331-3339, 2005.

[43] M. A. Belkin, J. A. Fan, S. Hormoz, F. Capasso, S. P. Khanna, M. Lachab*, et al.*, "Terahertz quantum cascade lasers with copper metal-metal waveguides operating up to 178 K," *Optics Express,* vol. 16, pp. 3242-3248, Mar 3 2008.

[44] S. Kumar, Q. Hu, and J. L. Reno, "186 K operation of terahertz quantum-cascade lasers based on a diagonal design," *Applied Physics Letters,* vol. 94, Mar 30 2009.

[45] S. Kumar, "Recent progress in terahertz quantum cascade lasers," *Selected Topics in Quantum Electronics, IEEE Journal of,* vol. 17, pp. 38-47, 2011.

[46] M. S. Vitiello, G. Scamarcio, V. Spagnolo, B. S. Williams, S. Kumar, Q. Hu*, et al.*, "Measurement of subband electronic temperatures and population inversion in THz quantum-cascade lasers," *Applied Physics Letters,* vol. 86, Mar 14 2005.

[47] B. S. Williams, S. Kumar, Q. Qin, Q. Hu, and J. L. Reno, "Terahertz quantum cascade lasers with double-resonant-phonon depopulation," *Applied physics letters,* vol. 88, pp. 261101-261101-3, 2006.

[48] S. Tsujino, A. Borak, E. Müller, M. Scheinert, C. Falub, H. Sigg*, et al.*, "Interface-roughness-induced broadening of intersubband electroluminescence in p-SiGe and n-GaInAs/AlInAs quantum-cascade structures," *Applied Physics Letters,* vol. 86, p. 062113, 2005.

[49] C. Walther, G. Scalari, J. Faist, H. Beere, and D. Ritchie, "Low frequency terahertz quantum cascade laser operating from 1.6 to 1.8 THz," *Applied physics letters,* vol. 89, pp. 231121-231121-3, 2006.

[50] L. Lever, N. Hinchcliffe, S. Khanna, P. Dean, Z. Ikonic, C. Evans*, et al.*, "Terahertz ambipolar dual-wavelength quantum cascade laser," *Optics express,* vol. 17, pp. 19926-19932, 2009.

[51] S. Kumar, Q. Hu, and J. L. Reno, "186 K operation of terahertz quantum-cascade lasers based on a diagonal design," *Applied Physics Letters,* vol. 94, p. 131105, 2009.

[52] A. Matyas, R. Chashmahcharagh, I. Kovacs, P. Lugli, K. Vijayraghavan, M. A. Belkin*, et al.*, "Improved terahertz quantum cascade laser with variable height barriers," *Journal of Applied Physics,* vol. 111, p. 103106, 2012.

[53] A. Jiang, A. Matyas, K. Vijayraghavan, C. Jirauschek, Z. R. Wasilewski, and M. A. Belkin, "Experimental investigation of terahertz quantum cascade laser with variable barrier heights," *Journal of Applied Physics,* vol. 115, p. 163103, 2014.

[54] H. Machhadani, Y. Kotsar, S. Sakr, M. Tchernycheva, R. Colombelli, J. Mangeney*, et al.*, "Terahertz intersubband absorption in GaN/AlGaN step quantum wells," *Applied Physics Letters,* vol. 97, pp. 191101-191101-3, 2010.

[55] G. Sun, R. A. Soref, and J. B. Khurgin, "Active region design of a terahertz GaN/Al< sub> 0.15</sub> Ga< sub> 0.85</sub> N quantum cascade laser," *Superlattices and Microstructures,* vol. 37, pp. 107-113, 2005.

[56] D. Indjin, Z. Ikonić, V. Jovanović, N. Vukmirović, P. Harrison, and R. Kelsall, "Relationship between carrier dynamics and temperature in terahertz quantum cascade structures: simulation of GaAs/AlGaAs, SiGe/Si and GaN/AlGaN devices," *Semiconductor science and technology,* vol. 20, p. S237, 2005.

[57] R. W. Boyd, *Nonlinear optics*: Academic press, 2003.

[58] Y.-R. Shen, "The principles of nonlinear optics," *New York, Wiley-Interscience, 1984, 575 p.,* vol. 1, 1984.

[59] G. Eckhardt, R. Hellwarth, F. McClung, S. Schwarz, D. Weiner, and E. Woodbury, "Stimulated Raman scattering from organic liquids," *Physical Review Letters,* vol. 9, p. 455, 1962.

[60] H. M. Pask, "The design and operation of solid-state Raman lasers," *Progress in Quantum Electronics,* vol. 27, pp. 3-56, 2003.

[61] W. Hartig and W. Schmidt, "A broadly tunable IR waveguide Raman laser pumped by a dye laser," *Applied physics,* vol. 18, pp. 235-241, 1979.

[62] F. Galeener, J. Mikkelsen Jr, R. H. Geils, and W. Mosby, "The relative Raman cross sections of vitreous SiO2, GeO2, B2O3, and P2O5," *Applied Physics Letters,* vol. 32, pp. 34-36, 1978.

[63] J. Nishizawa and K. Suto, "Semiconductor raman laser," *Journal of Applied Physics,* vol. 51, pp. 2429-2431, 1980.

[64] H. Rong, A. Liu, R. Jones, O. Cohen, D. Hak, R. Nicolaescu*, et al.*, "An all-silicon Raman laser," *Nature,* vol. 433, pp. 292-294, 2005.

[65] M. Scheinert, H. Sigg, S. Tsujino, M. Giovannini, and J. Faist, "Intersubband Raman laser from GaInAs/AlInAs double quantum wells," *Applied Physics Letters,* vol. 91, pp. 131108-131108-3, 2007.

[66] H. Liu, I. W. Cheung, A. SpringThorpe, C. Dharma-Wardana, Z. Wasilewski, D. Lockwood*, et al.*, "Intersubband Raman laser," *Applied Physics Letters,* vol. 78, pp. 3580-3582, 2001.

[67] M. Troccoli, A. Belyanin, F. Capasso, E. Cubukcu, D. L. Sivco, and A. Y. Cho, "Raman injection laser," *Nature,* vol. 433, pp. 845-848, 2005.

[68] J. B. Khurgin, G. Sun, L. R. Friedman, and R. Soref, "Comparative analysis of optically pumped intersubband lasers and intersubband Raman oscillators," *Journal of applied physics,* vol. 78, pp. 7398-7400, 1995.

[69] T. Ishibashi, S. Tarucha, and H. Okamoto, "Si and Sn Doping in Alxga1-Xas Grown by Mbe," *Japanese Journal of Applied Physics Part 2-Letters,* vol. 21, pp. L476-L478, 1982.

[70] P. Von Allmen, M. Berz, G. Petrocelli, F.-K. Reinhart, and G. Harbeke, "Inter-sub-band absorption in GaAs/AlGaAs quantum wells between 4.2 K and room temperature," *Semiconductor science and technology,* vol. 3, p. 1211, 1988.

[71] C. Sirtori, F. Capasso, J. Faist, L. Pfeiffer, and K. West, "Far-infrared generation by doubly resonant difference frequency mixing in a coupled quantum well two-dimensional electron gas system," *Applied physics letters,* vol. 65, pp. 445-447, 1994.

[72] E. Dupont, Z. R. Wasilewski, and H. C. Liu, "Terahertz emission in asymmetric quantum wells by frequency mixing of midinfrared waves," *Ieee Journal of Quantum Electronics,* vol. 42, pp. 1157-1174, Nov-Dec 2006.

[73] R. W. Adams, A. Vizbaras, M. Jang, C. Grasse, S. Katz, G. Boehm*, et al.*, "Terahertz sources based on intracavity frequency mixing in mid-infrared quantum cascade lasers with passive nonlinear sections," *Applied Physics Letters,* vol. 98, p. 151114, 2011.

[74] Q. Lu, N. Bandyopadhyay, S. Slivken, Y. Bai, and M. Razeghi, "Room temperature single-mode terahertz sources based on intracavity difference-frequency generation in quantum cascade lasers," *Applied Physics Letters,* vol. 99, p. 131106, 2011.

[75] K. Vijayraghavan, R. W. Adams, A. Vizbaras, M. Jang, C. Grasse, G. Boehm*, et al.*, "Terahertz sources based on Čerenkov difference-frequency generation in quantum cascade lasers," *Applied Physics Letters,* vol. 100, p. 251104, 2012.

[76] Q. Lu, N. Bandyopadhyay, S. Slivken, Y. Bai, and M. Razeghi, "Widely tuned room temperature terahertz quantum cascade laser sources based on difference-frequency generation," *Applied Physics Letters,* vol. 101, p. 251121, 2012.

[77] Q. Lu, N. Bandyopadhyay, S. Slivken, Y. Bai, and M. Razeghi, "High performance terahertz quantum cascade laser sources based on intracavity difference frequency generation," *Optics express,* vol. 21, pp. 968-973, 2013.

[78] K. Vijayraghavan, Y. Jiang, M. Jang, A. Jiang, K. Choutagunta, A. Vizbaras*, et al.*, "Broadly tunable terahertz generation in mid-infrared quantum cascade lasers," *Nature communications,* vol. 4, 2013.

[79] K. Vijayraghavan, M. Jang, A. Jiang, X. Wang, M. Troccoli, and M. A. Belkin, "Room-temperature 3.5 THz sources based on nonlinear frequency mixing in quantum cascade lasers," 2014.

[80] Y. Jiang, K. Vijayraghavan, S. Jung, F. Demmerle, G. Boehm, M. C. Amann*, et al.*, "External cavity terahertz quantum cascade laser sources based on intra-cavity frequency mixing with 1.2–5.9 THz tuning range," *Journal of Optics,* vol. 16, p. 094002, 2014.

[81] S. Jung, A. Jiang, Y. Jiang, K. Vijayraghavan, X. Wang, M. Troccoli*, et al.*, "Broadly tunable monolithic room-temperature terahertz quantum cascade laser sources," *Nature communications,* vol. 5, 2014.

[82] C. Pflügl, M. A. Belkin, Q. J. Wang, M. Geiser, A. Belyanin, M. Fischer*, et al.*, "Surface-emitting terahertz quantum cascade laser source based on intracavity difference-frequency generation," *Applied Physics Letters,* vol. 93, p. 161110, 2008.

[83] G. Askaryan, "Cerenkov and transition radiation from electromagnetic waves," *Zhur. Eksptl'. i Teoret. Fiz.,* vol. 42, 1962.

[84] P. Tien, R. Ulrich, and R. Martin, "optical second harmonic generation in form of coherent cerenkov radiation from a thin-film waveguide," *Applied Physics Letters,* vol. 17, pp. 447-450, 1970.

[85] D. Bagdasaryan, A. Makaryan, and P. Pogosyan, "Cerenkov radiation from a propagating nonlinear polarization wave," *JETP Lett,* vol. 37, 1983.

[86] M. Austerer, H. Detz, S. Schartner, M. Nobile, W. Schrenk, A. Andrews*, et al.*, "Čerenkov-type phase-matched second-harmonic emission from GaAs⁄AlGaAs quantum-cascade lasers," *Applied Physics Letters,* vol. 92, p. 111114, 2008.

[87] S. Kohen, B. S. Williams, and Q. Hu, "Electromagnetic modeling of terahertz quantum cascade laser waveguides and resonators," *Journal of applied physics,* vol. 97, p. 053106, 2005.

[88] E. D. Palik, *Handbook of optical constants of solids* vol. 3: Academic press, 1998.

[89] N. Hashizume, M. Ohashi, T. Kondo, and R. Ito, "Optical harmonic generation in multilayered structures: a comprehensive analysis," *JOSA B,* vol. 12, pp. 1894-1904, 1995.

[90] M. Geiser, C. Pflügl, A. Belyanin, Q. J. Wang, N. Yu, T. Edamura*, et al.*, "Gain competition in dual wavelength quantum cascade lasers," *Optics express,* vol. 18, pp. 9900-9908, 2010.

[91] M. Carras, M. Garcia, X. Marcadet, O. Parillaud, A. De Rossi, and S. Bansropun, "Top grating index-coupled distributed feedback quantum cascade lasers," *Applied Physics Letters,* vol. 93, Jul 7 2008.

[92] N. F. Yu, Q. J. Wang, M. A. Kats, J. A. Fan, S. P. Khanna, L. H. Li*, et al.*, "Designer spoof surface plasmon structures collimate terahertz laser beams," *Nature Materials,* vol. 9, pp. 730-735, Sep 2010.

[93] A. Hugi, R. Terazzi, Y. Bonetti, A. Wittmann, M. Fischer, M. Beck*, et al.*, "External cavity quantum cascade laser tunable from 7.6 to 11.4 μm," *Applied Physics Letters,* vol. 95, p. 061103, 2009.

[94] H. Richter, M. Greiner-Bar, S. G. Pavlov, A. D. Semenov, M. Wienold, L. Schrottke*, et al.*, "A compact, continuous-wave terahertz source based on a quantum-cascade laser and a miniature cryocooler," *Optics Express,* vol. 18, pp. 10177-10187, May 10 2010.

[95] Y. Bai, N. Bandyopadhyay, S. Tsao, S. Slivken, and M. Razeghi, "Room temperature quantum cascade lasers with 27% wall plug efficiency," *Applied Physics Letters,* vol. 98, pp. 181102-181102-3, 2011.

[96] B. G. Lee, H. A. Zhang, C. Pflügl, L. Diehl, M. A. Belkin, M. Fischer*, et al.*, "Broadband distributed-feedback quantum cascade laser array operating from 8.0 to 9.8 m," *IEEE Photonics Technology Letters,* vol. 21, 2009.

[97] R. Maulini, M. Beck, J. Faist, and E. Gini, "Broadband tuning of external cavity bound-to-continuum quantum-cascade lasers," *Applied Physics Letters,* vol. 84, pp. 1659-1661, Mar 8 2004.

[98] Q. Y. Lu, N. Bandyopadhyay, S. Slivken, Y. Bai, and M. Razeghi, "Room temperature terahertz quantum cascade laser sources with 215 mu W output power through epilayer-down mounting," *Applied Physics Letters,* vol. 103, Jul 1 2013.

[99] Q. Lu, N. Bandyopadhyay, S. Slivken, Y. Bai, and M. Razeghi, "Continuous operation of a monolithic semiconductor terahertz source at room temperature," *Applied Physics Letters,* vol. 104, p. 221105, 2014.

[100] A. W. Lee, Q. Qin, S. Kumar, B. S. Williams, Q. Hu, and J. L. Reno, "Real-time terahertz imaging over a standoff distance (≫ 25 meters)," *Applied Physics Letters,* vol. 89, pp. 141125-141125-3, 2006.